

University of Windsor

Scholarship at UWindor

Electronic Theses and Dissertations

Theses, Dissertations, and Major Papers

1975

AN EPR INVESTIGATION OF CALCIUM-HYDROXIDE: COPPER(II) AND CALCIUM-DEUTEROXIDE: COPPER(II) SYSTEMS.

ROBERT G. WILSON
University of Windsor

Follow this and additional works at: <https://scholar.uwindsor.ca/etd>

Recommended Citation

WILSON, ROBERT G., "AN EPR INVESTIGATION OF CALCIUM-HYDROXIDE: COPPER(II) AND CALCIUM-DEUTEROXIDE: COPPER(II) SYSTEMS." (1975). *Electronic Theses and Dissertations*. 1002.
<https://scholar.uwindsor.ca/etd/1002>

This online database contains the full-text of PhD dissertations and Masters' theses of University of Windsor students from 1954 forward. These documents are made available for personal study and research purposes only, in accordance with the Canadian Copyright Act and the Creative Commons license—CC BY-NC-ND (Attribution, Non-Commercial, No Derivative Works). Under this license, works must always be attributed to the copyright holder (original author), cannot be used for any commercial purposes, and may not be altered. Any other use would require the permission of the copyright holder. Students may inquire about withdrawing their dissertation and/or thesis from this database. For additional inquiries, please contact the repository administrator via email (scholarship@uwindsor.ca) or by telephone at 519-253-3000ext. 3208.

AN E.P.R. INVESTIGATION OF $\text{Ca}(\text{OH})_2:\text{Cu}^{++}$ AND $\text{Ca}(\text{OD})_2:\text{Cu}^{++}$ SYSTEMS

by

Robert G. Wilson

A Dissertation

Submitted to the Faculty of Graduate Studies through the Department
of Physics in Partial Fulfillment of the Requirements for
the Degree of Doctor of Philosophy at the
University of Windsor

Windsor, Ontario

1975

© Robert G. Wilson 1975

557064

ABSTRACT

The electron paramagnetic resonance (E.P.R.) spectra of the Cu^{++} ion in hexagonal $\text{Ca}(\text{OH})_2$ and $\text{Ca}(\text{OD})_2$ crystals have been investigated in the temperature range 4.2 - 300°K. Below 140°K, there exists an E.P.R. spectrum, I, which is associated with a static Jahn-Teller effect. Spectrum I has three axial components referred to as a, b, and c. Each was analysed by assuming the static distortions appropriate for trigonal symmetry. The unusually sharp spectrum of $\text{Ca}(\text{OD})_2:\text{Cu}^{++}$ provided measurements of not only the usual g-factors and diagonal components of the hyperfine-structure tensor, but also its off-diagonal components and quadrupole terms. A detailed analysis of spectrum I indicated a Jahn-Teller effect stabilization energy of $1,180 \pm 400 \text{ cm}^{-1}$, and a ground level splitting of $4,700 \pm 1,500 \text{ cm}^{-1}$. Above 150°K, this spectrum vanishes and is replaced by an axial spectrum, III. Significantly enough, the parameters of spectrum III are almost exact averages of the three corresponding parameters of spectrum I. This is expected if the system associated the low temperature spectrum, I, executes a hindered rotation about the hexagonal axis. If temperature variations of the peak heights of spectra I and III are described by an Orbach relaxation process, then the transition between them is characterized by an activation energy of $1,300 \pm 400 \text{ cm}^{-1}$.

Additional Cu^{++} spectra, II and IV, associated with non-Jahn-Teller systems were also observed. Most of the qualitative and quantitative features of these spectra are similar to those of spectrum I. However, these spectra do not vanish at high temperatures.

ACKNOWLEDGEMENTS

The author wishes to thank Dr. F. Holuj for suggesting this problem, and for his guidance and encouragement during the course of this work. Thanks are also extended to Dr. N. Hedgecock for his supervision during Dr. Holuj's absence, to Dr. C. Kikuchi for neutron irradiation of samples, to Mr. W. Grewe and the machine shop staff for construction of apparatus, to Mr. A. Buzzeo for his assistance with diagrams, and to Miss M. Shedlowich and Mrs. B. Walker for the typing of this thesis.

Financial assistance in the form of a National Research Council Scholarship is also gratefully acknowledged.

TABLE OF CONTENTS

	Page
ABSTRACT	iii
ACKNOWLEDGEMENTS	iv
LIST OF TABLES	viii
LIST OF FIGURES	x
I. INTRODUCTION	1
II. CRYSTALLOGRAPHY	8
III. THEORY	10
A. THE FREE CUPRIC ION	10
B. SPLITTING OF $3d^9 2D$ ORBITALS BY CRYSTAL FIELDS OF VARIOUS SYMMETRIES	11
C. CRYSTAL FIELD INTERACTION OF Cu^{++} WITH THE $Ca(OH)_2$ LATTICE IN THE ABSENCE OF JAHN-TELLER COUPLING	13
D. THE EXPERIMENTAL SPIN-HAMILTONIAN	16
E. THE ELECTRONIC SPIN-HAMILTONIAN USING A PERTURBATION APPROACH	16
1. Introduction to a Perturbation Approach	16
2. g-Factor	18
3. Hyperfine Structure	19
4. Quadrupole Interaction	21
F. THE JAHN-TELLER COUPLING INTERACTION (STATIC DEFORMATION TERM)	21
G. THE COMPLETE ELECTRONIC HAMILTONIAN	25
H. DYNAMIC JAHN-TELLER EFFECT	26
IV. INSTRUMENTATION AND MEASUREMENT TECHNIQUES	29
A. K BAND SPECTROMETER	29
B. X BAND SPECTROMETER	32
C. E.P.R. MEASUREMENTS	32

	Page
V. EXPERIMENTAL OBSERVATIONS AND RESULTS	36
A. GENERAL REMARKS	36
B. THE JAHN-TELLER CUPRIC ION	38
1. Low Temperature Spectrum	38
i) Angular variation	38
ii) Quantitative results for spectrum I	39
iii) Superhyperfine structure	39
2. High Temperature Spectrum	47
3. The Transition Temperature	51
C. NON-JAHN-TELLER CUPRIC IONS	51
1. Qualitative Discussion of spectra II and IV	51
2. Quantitative Results for spectra II and IV	54
D. APPLIED STRESS	54
E. RADIATION DAMAGE	58
VI. DISCUSSION OF THE RESULTS	59
A. THE JAHN-TELLER CUPRIC ION	59
1. Low Temperature Spectrum	59
2. High Temperature Spectrum	62
B. NON-JAHN-TELLER CUPRIC ION	65
VII. SUMMARY AND CONCLUSIONS	66
APPENDIX A DEFINITION OF SYMBOLS USED IN MATHEMATICAL RELATIONSHIPS	68
APPENDIX B NORMALIZED SPHERICAL HARMONICS $Y_{lm}(\theta, \phi)$ TO ORDER $l = 4$	73
APPENDIX C REAL ANGULAR FUNCTIONS $Z_{lm}(\theta, \phi)$, $l=2$ and 4	75
APPENDIX D POINT CHARGE MODEL CRYSTAL FIELD EIGENVALUES AND EIGENVECTORS	77
APPENDIX E POINT CHARGE MODEL ESTIMATES OF $\text{Ca}(\text{OH})_2:\text{Cu}^{++}$ SYSTEM PARAMETERS	80
APPENDIX F TRANSFORMATIONS OF THE Z_{2i} BASIS FUNCTIONS FOR A COUNTER-CLOCKWISE ROTATION OF CO-ORDINATE AXES BY α ABOUT THE Y-AXIS IN FIG. 1	81

APPENDIX G	NON-ZERO MATRIX ELEMENTS OF THE SPIN-HAMILTONIAN OF EQ. (9) BETWEEN THE STATES $ 1/2, M_S, 3/2, M_I\rangle$	82
APPENDIX H	PROPERTIES OF ANGULAR MOMENTUM OPERATORS L_x, L_y, L_z, L_+ and L_- WITHIN MANIFOLDS SPANNED BY SECOND ORDER SPHERICAL HARMONICS, BY REAL LINEAR COMBINATIONS OF 3d ORBITALS DEFINED z_{2i} , AND BY CRYSTAL FIELD EIGENSTATES OF Cu^{++} TRANSFORMING AS REPRESENTATIONS $1E_g, A_{1g}$ AND $2E_g$ IN D_{3d} SYMMETRY	85
APPENDIX I	NON-ZERO ELEMENTS OF THE SECOND ORDER PERTURBATION TENSOR Λ_{pq}	91
APPENDIX J	ELEMENTS OF THE SECOND ORDER PERTURBATION TENSOR λ_{pq}	92
APPENDIX K	NON-ZERO ELEMENTS OF THE SECOND ORDER PERTURBATION TENSOR Λ'_{pq}	93
APPENDIX L	NORMAL CO-ORDINATES OF AN XY_6 COMPLEX OF D_{3d} SYMMETRY	95
APPENDIX M	NON-ZERO MATRIX ELEMENTS OF THE COMPLETE ELECTRONIC HAMILTONIAN, H_{ORB} , WITHIN THE MANIFOLD SPANNED BY THE STATES $ z_{2i}, \pm 1/2\rangle$	97
APPENDIX N	SPIN-HAMILTONIAN PARAMETERS OF AN AVERAGED SPECTRUM I	99
REFERENCES		102
BIBLIOGRAPHY		106

LIST OF TABLES

	Page
I. Spin-Hamiltonian Parameters of Jahn-Teller Coupled $\text{Ca}(\text{OH})_2:\text{Cu}^{++}$ and $\text{Ca}(\text{OD})_2:\text{Cu}^{++}$ Complexes	44
II. Parameters of Cu^{++} in $\text{Ca}(\text{OD})_2$	45
III. Spin-Hamiltonian Parameters of the Dynamic Jahn-Teller Effect Spectrum in $\text{Ca}(\text{OH})_2:\text{Cu}^{++}$ and $\text{Ca}(\text{OD})_2:\text{Cu}^{++}$ Systems	50
IV. Spin-Hamiltonian Parameters of non-Jahn-Teller Coupled $\text{Ca}(\text{OH})_2:\text{Cu}^{++}$ and $\text{Ca}(\text{OD})_2:\text{Cu}^{++}$ Complexes	57
B1. Spherical Harmonics in both Spherical and Rectangular Co-ordinate Representations for $\ell = 1$ to 4	74
C1. Real Angular Functions, $Z_{\ell m}(\theta, \phi)$, $\ell = 2$ and 4	76
E1. Point Charge Model Estimates of $\text{Ca}(\text{OH})_2:\text{Cu}^{++}$ System Parameters	80
H1. Functions Generated by the Angular Momentum Operators L_+ , L_- , and L_z Operating on the Spherical Harmonic Functions $ Y_{2-m}\rangle$ and $ Y_{2-m}^*\rangle$, $M = 0, 1, 2$	86
H2. Functions Generated by the Angular Momentum Operators L_x , L_y , and L_z Operating on the Real Linear Combinations of 3d Orbitals, Z_{2i}	87
H3. Matrix Elements of the Angular Momentum Operators L_x , L_y , and L_z Within the Manifold Spanned by the Real Cu^{++} Orbital Eigenfunctions $ \epsilon\rangle$, $ \theta\rangle$, $ \phi\rangle$, $ c\rangle$ and $ s\rangle$ Defined in the (x,y,z) Co-ordinate System of Fig.1 by Eq.(8)	88

H4. Matrix Elements of the Spin-Orbit Interaction,

$V_{LS} = \lambda \vec{L} \cdot \vec{S}$, Within the Manifold Spanned by

the Coupled Real Orbital-Spin Functions

$|z_{2i}, M_s\rangle, M_s = 1/2, -1/2$

90

L1. Normal Co-ordinates of an XY_6 Complex of D_{3d}

Symmetry

95

LIST OF FIGURES

	Page
1. Geometry of a Ca^{++} Site in $\text{Ca}(\text{OH})_2$	9
2. Crystal Field Splitting of the $3d^9 2D$ Term	12
3. Averaging of the Low Temperature Cu^{++} Spectrum by Thermal Reorientation of the Elongated Octahedral Complex	27
4. Block Diagram of the K Band E.P.R. Spectrometer	30
5. The K Band Cavity Assembly	31
6. Block Diagram of the X Band E.P.R. Spectrometer	33
7. The X Band Cavity Assembly used in Uniaxial Stress and Temperature Dependence Experiments	34
8. Typical Jahn-Teller Spectra of a $\text{Ca}(\text{OH})_2:\text{Cu}^{++}$ System for General Orientations of \vec{H}	37
9. Recordings of Spectrum I for $\text{Ca}(\text{OD})_2:\text{Cu}^{++}$ at significant Orientations of \vec{H} in the $(1\bar{2}10)$ plane at 80°K	40
10. Angular Variation of Spectrum Ia in the $(1\bar{2}10)$ plane for $\text{Ca}(\text{OD})_2:\text{Cu}^{++}$ at 80°K	41
11. Angular Variation of Spectrum Ia in the y-z plane	42
12. Forbidden Transitions of Spectrum Ia Observed for $\text{Ca}(\text{OD})_2:\text{Cu}^{++}$	43
13. Superhyperfine Structure Observed for $\text{Ca}(\text{OH})_2:\text{Cu}^{++}$ Systems at Various Temperatures	46
14. Temperature Dependence of $\text{Ca}(\text{OH})_2:\text{Cu}^{++}$ Spectra	48
15. Temperature Dependence of $\text{Ca}(\text{OD})_2:\text{Cu}^{++}$ Spectra	49
16. Plots of $\text{Log } I_p$ versus T^{-1} for Spectra I and III	52

	Page
17. Recording of the Non-Jahn-Teller Spectra II and IV for a General Orientation of \vec{H} in the $(1\bar{2}10)$ Plane	53
18. Recording of the $\text{Ca}(\text{OD})_2:\text{Cu}^{++}$ Spectrum for a General Orientation of \vec{H} in the $(10\bar{1}0)$ Plane at 80°K and at 4.2°K	53
19. Effect of Uniaxial Stress when Applied to $\text{Ca}(\text{OH})_2:\text{Cu}^{++}$ along the $[1\bar{2}10]$ Direction at 4.2°K	55
20. Effect of Uniaxial Stress when Applied to $\text{Ca}(\text{OH})_2:\text{Cu}^{++}$ along the $[0001]$ Direction at 80°K	56
21. Angular Variations of the Jahn-Teller Spectra of $\text{Ca}(\text{OH})_2:\text{Cu}^{++}$ in the $(1\bar{2}10)$ Plane	64
L1. Some of the Normal Modes of an XY_6 Complex with D_{3d} Symmetry	96

I. INTRODUCTION

The mineral group containing the isomorphous compounds, portlandite ($\text{Ca}(\text{OH})_2$) and brucite ($\text{Mg}(\text{OH})_2$), has long been the subject of extensive experimental investigation. Until recently, most interest in these compounds was the result of difficulties encountered in accurate location of their protons, the detection of anomalous sidebands associated with their infrared spectra, and most importantly, their occurrence as major structural modules in certain silicates, such as clays and micas.

As early as 1921, Aminoff¹ located the magnesium and oxygen sites in $\text{Mg}(\text{OH})_2$ by x-ray diffraction techniques. Additionally, he established that the brucite lattice is a CdI_2 -type structure, exhibiting hexagonal symmetry about an axis directed normal to the crystal cleavage plane. The magnesium and oxygen atoms were found to sit in layers parallel to the cleavage plane, with oxygen layers located on both sides of each Mg layer at separations of about 1.04 Å. The arrangement of atoms within these layers formed a central, hexagonal pattern with atomic separations of about 3.12 Å.

By 1933, Megaw² had obtained accurate values of the lattice constants of both brucite and portlandite, and had determined the oxygen positions in $\text{Ca}(\text{OH})_2$. Although location of hydrogen sites had been impossible, Bernal and Megaw³ postulated that each O-H bond is parallel to the hexagonal axis (c axis), and that no hydrogen bonding existed between adjacent layers of oxygen atoms. These conclusions were derived on the basis of symmetry and electrostatic

arguments, and were confirmed by the low frequency infrared investigations of Yeou Ta,⁴ and Duval and Lecompte^{5,6} in the early 1940's.

Mara and Sutherland⁷ investigated the infrared spectrum of brucite in 1953. They observed a band exhibiting fine structure with at least sixteen sub-bands, all associated with O-H stretching frequencies and exhibiting a variety of polarization properties. In interpreting these observations, Mara and Sutherland questioned the unit cell model originally proposed by Bernal and Megaw, and suggested that the unit cell must be larger than indicated by earlier x-ray analysis.

In response to the Mara and Sutherland conclusions, the crystal structures of brucite and portlandite were reinvestigated by Petch and Megaw⁸. The new x-ray data revealed nothing to support the Mara and Sutherland proposal of a larger unit cell. However, an additional study of the infrared absorption in portlandite did uncover an anomalous spectrum similar to that observed for brucite.

The proton positions in brucite were first determined by Elleman and Williams⁹. From the nuclear magnetic resonance (N.M.R.) spectrum, they determined the distance between nearest neighbour protons when located both in the same and in adjacent planes. From this information, the separation between hydrogen planes was calculated. By a comparison of this spacing with the separation between oxygen layers known from x-ray investigations, Elleman and Williams were able to provide the first estimate of the O-H bond length.

Soon after this, Mara and Sutherland¹⁰ observed that the anomalous sidebands on the infrared spectrum

disappeared when the sample temperature was lowered to 80°K . This demonstrated that these sidebands were associated with thermal motions of the protons, and two alternative explanations of these sidebands were proposed. The first, by Hexter and Dows,¹¹ suggested that the sidebands arise from librational or hindered rotational motions of the hydroxide ions which couple to the internal stretching motion of the O-H bond. The second, attributed to Wickersheim,¹² assumed that low frequency crystalline lattice modes couple to the internal stretching motion of the OH^- ion. The investigation of energy levels in brucite and portlandite by inelastic scattering of slow neutrons by Safford, Brajovic and Boutin¹³ supported the latter hypothesis over the rotational model proposed by Hexter and Dows.

A neutron diffraction study of single crystals of $\text{Ca}(\text{OH})_2$ by Busing and Levy¹⁴ confirmed the hydrogen atoms to be positioned as postulated by Bernal and Megaw. Particular attention was given to the thermal motions of various ions in the portlandite lattice. For hydrogen atoms, it was found that displacements parallel to the c axis are small while those in the hydrogen plane are much larger and temperature dependent, indicating that forces tending to align the OH^- ions are weak. The Ca^{++} ions, on the other hand, were found to move almost entirely parallel to the c axis. Small amplitude oxygen motions were also found to be confined to this direction. The observed lack of hydrogen bonding in $\text{Ca}(\text{OH})_2$ was attributed to a lack of sufficient polarity in the OH^- ions to form such bonds.

The electron distribution in a $\text{Ca}(\text{OH})_2$ crystal was determined by Petch¹⁵ using x-ray and Fourier synthesis techniques. His predictions of the hydrogen positions and O-H bond length differed from the values obtained from the

neutron diffraction studies of Busing and Levy. However, similar discrepancies had been noted in O-H bond length determinations for other substances, and were attributed to increased electronic density in the bond region between ions.

Considering its simple structure and interesting vibrational properties, it is amazing that the $\text{Ca}(\text{OH})_2$ lattice has been, until recently, completely overlooked as a host lattice for electron paramagnetic resonance (E.P.R.) investigations. Paramagnetic ions are often capable of strong coupling to lattice vibrational modes. In such cases, the changes in E.P.R. spectra not only indicate the effect of lattice vibrations on the paramagnetic ion, but also can provide extensive information regarding the physical properties of the lattice and the nature of its vibrational modes in the vicinity of the paramagnetic ion. In the first E.P.R. investigation¹⁶ involving a $\text{Ca}(\text{OH})_2$ -type host lattice, an interesting temperature dependence was observed for the crystal field and hyperfine interaction parameters of the Mn^{++} ion, clearly demonstrating pronounced coupling of the ion to $\text{Ca}(\text{OH})_2$ lattice vibrations.

As a result of the vibrational effects observed for the $\text{Ca}(\text{OH})_2:\text{Mn}^{++}$ system, it was decided that the Cu^{++} ion, well known for its ability to couple strongly to lattice distortions of high symmetry systems by a Jahn-Teller coupling mechanism, would be an interesting candidate for study as a dilute substitutional impurity in the $\text{Ca}(\text{OH})_2$ system.

$\text{Ca}(\text{OH})_2$ crystals of a workable size (about 5 mm per side) were easily grown from solution by a slow diffusion technique, and traces of copper impurity were found to enter the lattice readily when present in solution. A preliminary investigation of the $\text{Ca}(\text{OH})_2:\text{Cu}^{++}$ system indicated that

the cupric E.P.R. lines were intense, reasonably narrow, and observable over a wide temperature range (including room temperature). When sample temperatures were below 150°K , three highly anisotropic, almost axial Cu^{++} spectra were observed which closely resembled spectra associated with manifestations of a static Jahn-Teller effect in other cupric systems. When sample temperatures were above 150°K , a single, slightly anisotropic Cu^{++} spectrum was observed which was similar to spectra associated with examples of a dynamic Jahn-Teller effect in other cupric systems. In addition, the high temperature spectrum exhibited the peculiar property of existing as an approximate average of the three low temperature spectra. Consequently, the preliminary observations encouraged the more detailed E.P.R. investigation of $\text{Ca}(\text{OH})_2 : \text{Cu}^{++}$ and $\text{Ca}(\text{OD})_2 : \text{Cu}^{++}$ systems upon which this thesis is based.

The Jahn-Teller effect, which occurs when certain ions couple to their nearest neighbours in a high symmetry complex, was first predicted in a theorem postulated by Jahn and Teller¹⁷ about thirty-eight years ago. This theorem predicts that any non-linear complex having an electronically degenerate ground state is intrinsically unstable, and that it will distort in a manner such that the degeneracy is lifted and the overall ground state energy of the complex is lowered. The sole exception to this rule is the Kramers degeneracy present for all odd-electron atoms.


Over the last sixteen years, Jahn-Teller effects have been observed for the orbital doublet (^2E) state in cubic symmetry in a number of systems, including $\text{AgCl} : \text{Cu}^{++}$, $\text{NaCl} : \text{Ag}^{++}$, $\text{LiCl} : \text{Ag}^{++}$, $\text{KCl} : \text{Ag}^{++}$, $\text{CaO} : \text{Ni}^{3+}$, $\text{LiF} : \text{Ni}^{+}$, $\text{NaF} : \text{Ni}^{+}$, $\text{CaF}_2 : \text{Y}^{++}$, $\text{Al}_2\text{O}_3 : \text{Pd}^{3+}$, $\text{A}_2\text{O}_3 : \text{Ni}^{3+}$, $\text{MgO} : \text{Ni}^{+}$, and $\text{CaF}_2 : \text{Ti}^{3+}$.¹⁸⁻³⁵ Experimental studies by Coffman²⁶⁻²⁸ on $\text{MgO} : \text{Cu}^{++}$ by Hochli and Estle²⁹ on $\text{CaF}_2 : \text{Sc}^{++}$, and

by Hochli³⁰ on $\text{SrF}_2 : \text{Sc}^{++}$, have revealed the existence of a type of dynamic Jahn-Teller effect originating from the zero-point motion of ions in the ground state. During this same period, earlier theoretical treatments of these problems³¹⁻³⁴ have been extended, mainly by O'Brien, Bersuker and Ham.³⁵⁻³⁷

An extensive review of Jahn-Teller effects observed in solids was written by Sturge³⁸ in 1967. It considered in detail the manifestation of Jahn-Teller effects in optical and in some aspects of E.P.R. spectra of ions in solids, and in a variety of other solid state phenomena. A later review by Ham³⁹ in 1968 dealt exclusively with the influence of the Jahn-Teller effect on E.P.R. spectra. In it, Ham formulated a generalized approach to the problem for the cases of strong, intermediate, and weak coupled systems in both the orbital doublet and the orbital triplet states. The two reviews, and the more recent book by Abragam and Bleaney,⁴⁰ generally reflect the state of understanding of the Jahn-Teller effect on the spectra of ions in solids.

Until the present investigation,^{41,42} however, the treatment of the Jahn-Teller effect associated with the orbital doublet (^2E) state has dealt only with systems involving cubic or octahedral symmetry. In the $\text{Ca}(\text{OH})_2$ system, the Cu^{++} impurities substitute for Ca^{++} ions at sites of D_{3d} symmetry, which are one step removed from octahedral symmetry. Hence, the results of a detailed investigation of the E.P.R. spectra associated with $\text{Ca}(\text{OH})_2 : \text{Cu}^{++}$ and $\text{Ca}(\text{OD})_2 : \text{Cu}^{++}$ systems presented in this thesis represent the first attempt at extending the treatment of orbital doublet states to Jahn-Teller systems with lower than cubic symmetry.

Generally speaking, most details of the Cu^{++} spectra agree well with the predictions of the theory developed for orbital doublet states in Jahn-Teller systems of D_{3d} symmetry. Nevertheless, there do remain some aspects of $\text{Ca}(\text{OH})_2 : \text{Cu}^{++}$ -type systems which require further investigation before the nature of these systems is completely understood. It is hoped that the results presented in this thesis will stimulate new experimental interest in similar systems.



II. CRYSTALLOGRAPHY

X-ray studies⁴³⁻⁴⁵ have shown that $\text{Ca}(\text{OH})_2$ single crystals belong to a hexagonal system with space group $P(3,2/m,1)$, and are of CdI_2 -type. The calcium atoms lie in invariant positions $(0,0,0)$, with point symmetry D_{3d} , while the oxygen and hydrogen atoms are located at positions $\pm(1/3, 2/3, z_o)$ and $\pm(1/3, 2/3, z_h)$ respectively, both with point symmetry $3m$.

The $\text{Ca}(\text{OH})_2$ structure consists of layers of two sheets of hydroxyls parallel to the (0001) plane, with a sheet of Ca atoms sandwiched between them. As shown in Fig.1, each Ca atom sits in the centre of six neighbouring OH groups. These form an octahedron about it which is slightly compressed along the hexagonal or c axis of the crystal. The opposed hydroxyl sheets are bound together by weak van der Waals' forces. Neutron diffraction studies⁴⁶ have indicated that the thermal motion of the hydrogens is confined mainly to the hydrogen layers normal to the c axis. As a result, there are no hydrogen bonds between layers, as is readily confirmed by the observed softness (2 on Moh's scale) and a perfect cleavage in the (0001) plane.

Copper atoms enter the lattice as substitutional impurities at Ca sites. The symmetry of such a site occupied by Cu^{++} is changed from D_{3d} by a strong Jahn-Teller coupling of the Cu^{++} ion to distortions of its nearest neighbours. Bonds with four planar hydroxyls appear to determine the symmetry axis of the paramagnetic centre, as is illustrated in Fig.1.

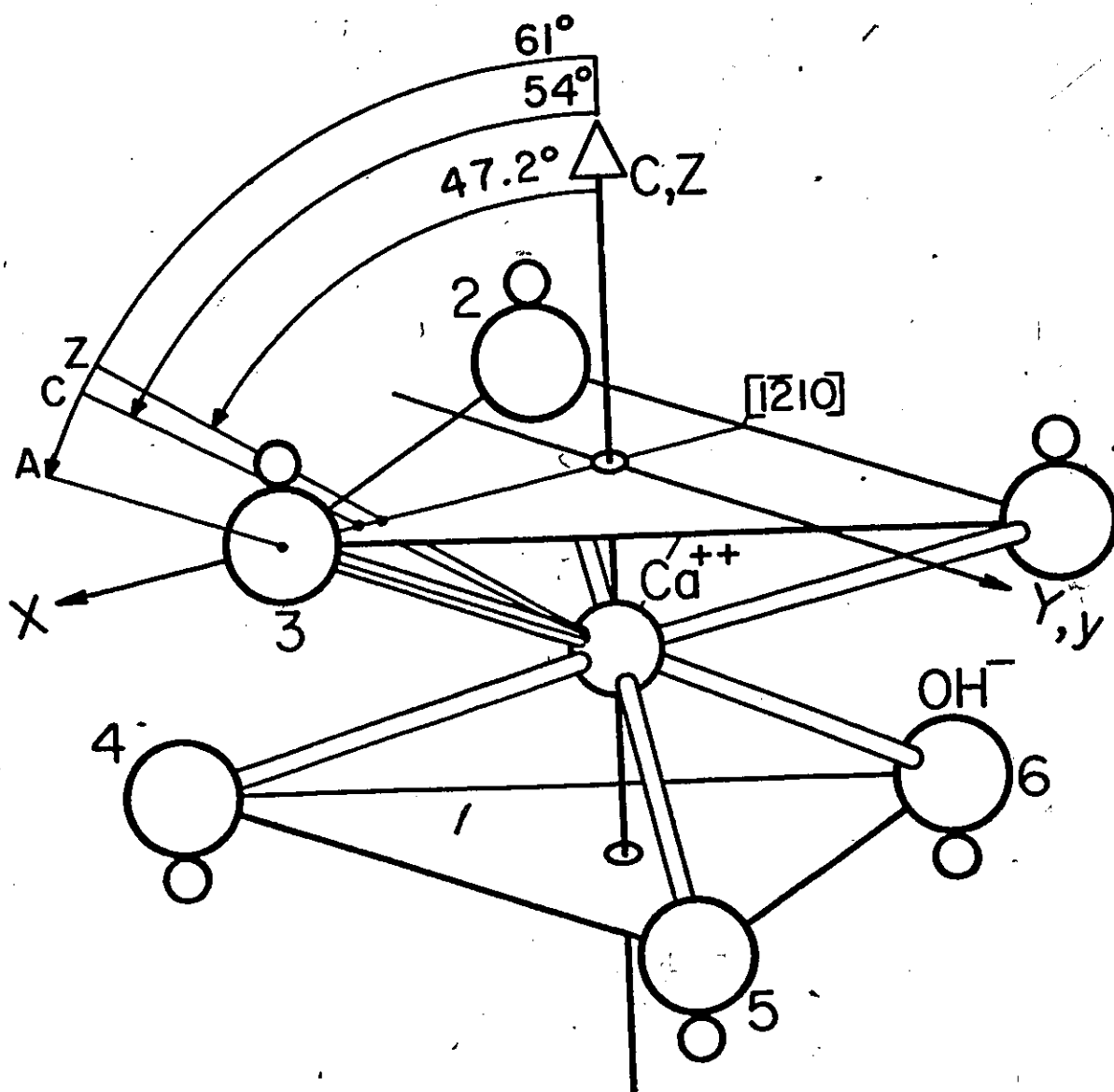


Fig.1 Geometry of a Ca^{++} site in $\text{Ca}(\text{OH})_2$. Lines A and C indicate the directions of the $\text{Ca}-\text{O}$ bond in $\text{Ca}(\text{OH})_2$ and in undistorted octahedrons respectively. The plane of hydroxyls 1, 2, 4 and 5 is angled at 42.5° to the trigonal axis (line C, Z). The co-ordinate systems (X, Y, Z) and (x, y, z) have the Ca site as their origin.

III. THEORY

A. THE FREE CUPRIC ION

The ground state of the free Cu^{++} ion is a 2D term that exhibits a five-fold electronic orbital degeneracy typical of a single d hole. The Hamiltonian that describes this system may be expressed in the following way, with terms listed in the order of their magnitude:

$$H = V_F + V_{LS} + V_I + V_H + V_Q + V_h. \quad (1)$$

In this equation,

$$V_F = \sum_{k=1}^N \left(\frac{p_k^2}{2m} - \frac{Ze^2}{r_k} \right) + \sum_{k>j=1}^N \frac{e^2}{r_{kj}} \quad (1a)$$

is the sum of kinetic and Coulomb energies,

$$V_{LS} = \sum_{j,k=1}^N \left(a_{jk} \vec{I}_j \cdot \vec{s}_k + b_{jk} \vec{I}_j \cdot \vec{I}_k + c_{jk} \vec{s}_j \cdot \vec{s}_k \right) \quad (1b)$$

is the spin orbit interaction,

$$V_I = 2\gamma\beta\beta_n \sum_{k=1}^N \left\{ \frac{(\vec{I}_k - \vec{s}_k) \cdot \vec{I}}{r_k^3} + \frac{3(\vec{r}_k \cdot \vec{s}_k)(\vec{r}_k \cdot \vec{I})}{r_k^5} + \frac{8\pi\delta(r_k)(\vec{s}_k \cdot \vec{I})}{3} \right\} \quad (1c)$$

is the hyperfine interaction, including the anomalous interaction of s electrons with the nucleus,

$$V_H = \sum_{k=1}^N \beta (\vec{l}_k + 2\vec{s}_k) \cdot \vec{H} \quad (1d)$$

is the electronic Zeeman term,

$$V_Q = \frac{e^2 Q}{2I(2I-1)} \sum_{k=1}^N \left(\frac{I(I+1)}{r_k^3} - \frac{3(\vec{r}_k \cdot \vec{I})^2}{r_k^5} \right) \quad (1e)$$

is the nuclear quadrupole term, and

$$V_h = \gamma_n \beta_n \vec{H} \cdot \vec{I} \quad (1f)$$

is the nuclear Zeeman term. The symbols found in these and all subsequent equations are defined in Appendix A.

B. SPLITTING OF $3d^9 \ ^2D$ ORBITALS BY CRYSTAL FIELDS OF VARIOUS SYMMETRIES

When a Cu^{++} ion is located in a dielectric crystal, it is subjected to an electrostatic field of strength and symmetry determined by the positions and charge distributions of neighbouring ions. The interaction of Cu^{++} with this crystal field adds a term, V_T , to the free ion Hamiltonian given in Eq.(1). This term, larger in magnitude than all terms of Eq.(1) except V_F , is responsible for lifting the orbital degeneracy of 3d orbitals in the manner illustrated in Fig.2 for Stark fields of successively lower symmetry. It should be noted that the trigonal component of a D_{3d} symmetry field splits the excited triplet into a doublet and a singlet, but fails, however, to lift the degeneracy of the ground doublet. Furthermore, there is no first order spin orbit splitting of this 2E state in O_h or in D_{3d} symmetry.

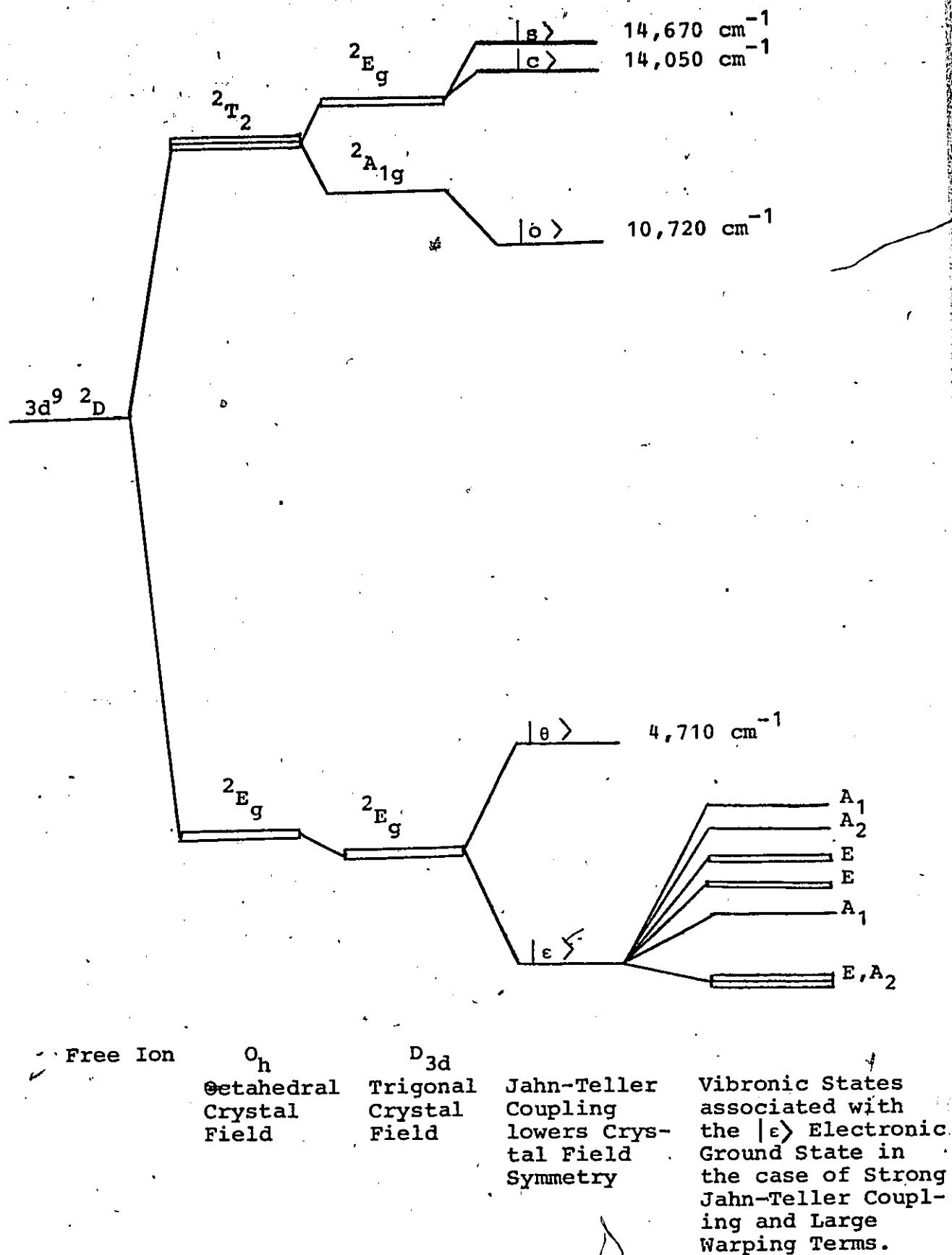


Fig.2 Crystal field splitting of the $3d^9 2D$ term.

C. CRYSTAL FIELD INTERACTION OF Cu^{++} WITH THE $\text{Ca}(\text{OH})_2$ LATTICE IN THE ABSENCE OF JAHN-TELLER COUPLING

Ignoring the effect of Jahn-Teller coupling for the present, the interaction of the Cu^{++} ion with the electrostatic field generated by six nearest neighbour OH^- ions at the Cu^{++} site in the $\text{Ca}(\text{OH})_2$ lattice is defined by the Hamiltonian term

$$V_T = \sum_{i=1}^6 - \frac{|ee^-|}{|\vec{R}_i - \vec{r}|} \quad (2)$$

For pure 3d orbitals in the point charge model approximation, Eq.(2) can be expanded in electronic spherical harmonics to give the result

$$V_T = -|ee^-| \left[\frac{3r^2}{R^3} f_{20} Y_{20}(\theta, \phi) + \frac{3r^4}{4R^5} \left[f_{40} Y_{40}(\theta, \phi) + 2\sqrt{35} f_{43} (Y_{4-3}(\theta, \phi) + Y_{4-3}^*(\theta, \phi)) \right] \right], \quad (3)$$

when the quantization axis of the system coincides with the trigonal axis of the complex (i.e. X,Y,Z co-ordinate system of Fig.1). It is more convenient, however, to redefine V_T in terms of the following real linear combinations of spherical harmonics:

$$\begin{aligned} Z_{10}(\theta, \phi) &= Y_{10}(\theta, \phi), \\ Z_{1m}^C(\theta, \phi) &= \frac{\sqrt{2}}{2} \left[Y_{1-m}(\theta, \phi) + Y_{1-m}^*(\theta, \phi) \right], \\ Z_{1m}^S(\theta, \phi) &= i\frac{\sqrt{2}}{2} \left[Y_{1-m}(\theta, \phi) - Y_{1-m}^*(\theta, \phi) \right], \end{aligned} \quad (4)$$

which are specifically defined in Appendix C for $l=2,4$ in both spherical harmonic and rectangular co-ordinate representations. A further simplification is incurred by

defining the parameters

$$A_{40} = \frac{-3}{4R^5} |ee'| \langle r^4 \rangle ,$$

$$A_{20} = \frac{-3}{R^3} |ee'| \langle r^2 \rangle ,$$

$$\delta = \frac{A_{20}}{A_{40}} \quad (5)$$

where $\langle r^k \rangle$ is the electronic expectation value of the operator r^k given by the integral $\int_0^\infty R_{3d}^* R_{3d} r^{k+2} dr$. Then, the crystal field interaction is given by

$$V_T = A_{40} \left[\delta f_{20} Z_{20}(\theta, \phi) + f_{40} Z_{40}(\theta, \phi) + 2\sqrt{70} f_{43} Z_{43}^C(\theta, \phi) \right] , \quad (6)$$

where V_T has matrix elements, as specified in Appendix D, between the angular parts of the real 3d orbitals Z_{20} , Z_{21}^C , Z_{22}^C , Z_{21}^S , and Z_{22}^S .

Preliminary calculations were made using the point charge estimates for $\text{Ca}(\text{OH})_2$ parameters listed in Appendix E, and the relationships developed in Appendix D. It was found that the crystal field interaction splits the 2D ground term of Cu^{++} into a ground $1E_g$ doublet, an excited A_{1g} singlet, and an excited $2E_g$ doublet with eigenstates

$$|\epsilon\rangle = -\sin v |Z_{21}^S\rangle + \cos v |Z_{22}^S\rangle ,$$

$$|\theta\rangle = \sin v |Z_{21}^C\rangle + \cos v |Z_{22}^C\rangle ,$$

$$|0\rangle = |z_{20}\rangle$$

$$|C\rangle = \sin v |z_{22}^C\rangle - \cos v |z_{21}^C\rangle$$

$$|S\rangle = \sin v |z_{22}^S\rangle + \cos v |z_{21}^S\rangle \quad (7)$$

respectively. Moreover, these initial computations indicated that an estimated δ -value of approximately 1.5 required a value of about 49° for v in Eq.(7). The additional experimental observation that the \tilde{g} tensor symmetry axis is directed at 47.5° to the trigonal axis (i.e. exactly perpendicular to the plane containing four OH^- ions), justifies fixing v at 47.5° . Then, δ is treated as one of several parameters to be determined by a computer fit to experimental data. Final results of such a fitting procedure indicate a value of 2.03 for δ . Furthermore, if $A_{40} = -5040\text{cm}^{-1}$, then the levels A_{1g} and $2E_g$ are 10,370 and $10,970\text{cm}^{-1}$ above the ground doublet.

Often it is convenient to calculate matrix elements of the remaining spin dependent terms in the co-ordinate system (x,y,z) defined in Fig.1. This is particularly the case when using perturbation theory to evaluate theoretical spin-Hamiltonian parameters for comparison with those measured for the experimental spin-Hamiltonian, defined by Eq.(9). Transformations of the orbital functions, z_{2i} , have been derived for a counter-clockwise rotation of co-ordinate axes by α about the Y-axis, and are specified in Appendix F. Since v was previously defined equal to α , the real linear combinations of d orbitals which transform as bases of the irreducible representations $1E_g$, A_{1g} , and $2E_g$ in the co-ordinate system (x,y,z) are:

$$|\epsilon\rangle = |xy\rangle,$$

$$|\theta\rangle = \frac{3\sqrt{3}\sin^2\alpha\cos\alpha}{2}|z^2\rangle + \frac{\cos\alpha(\cos^2\alpha-1)}{2}|x^2-y^2\rangle + \sin\alpha(3\cos^2\alpha-1)|zx\rangle,$$

$$|O\rangle = \frac{3\cos^2\alpha-1}{2} |z^2\rangle + \frac{\sqrt{3}\sin^2\alpha}{2} |x^2-y^2\rangle - \sqrt{3}\sin\alpha\cos\alpha |zx\rangle,$$

$$|C\rangle = -\frac{\sqrt{3}\sin\alpha(3\cos^2\alpha-1)}{2} |z^2\rangle + \frac{\sin\alpha(3\cos^2\alpha+1)}{2} |x^2-y^2\rangle + \cos\alpha(3\sin^2\alpha-1) |zx\rangle,$$

$$|S\rangle = |zy\rangle, \quad (8)$$

respectively. $|z^2\rangle = |z_{20}(x,y,z)\rangle$, $|zx\rangle = |z_{21}^C(x,y,z)\rangle$, $|x^2-y^2\rangle = |z_{22}^C(x,y,z)\rangle$, $|zy\rangle = |z_{21}^S(x,y,z)\rangle$ and $|xy\rangle = |z_{22}^S(x,y,z)\rangle$ have been introduced to simplify notation.

D. THE EXPERIMENTAL SPIN-HAMILTONIAN

For the purpose of analysis and presentation of experimental data, the $\text{Ca}(\text{OH})_2:\text{Cu}^{++}$ system can be conveniently treated as a spin doublet whose behaviour is described by the spin-Hamiltonian

$$H_{\text{spin}} = \beta \vec{S} \cdot \vec{g} \cdot \vec{H} + \vec{I} \cdot \vec{A} \cdot \vec{S} + \vec{I} \cdot \vec{Q} \cdot \vec{I} - \gamma \beta_n \vec{I} \cdot \vec{H}. \quad (9)$$

Matrix elements of this spin-Hamiltonian, operating within the $|S, I, M_S, m_I\rangle$ manifold where $S=1/2$ and $I=3/2$, are listed in Appendix G.

E. THE ELECTRONIC SPIN-HAMILTONIAN USING A PERTURBATION APPROACH

1. Introduction to a Perturbation Approach

In the analysis of other systems in which the Cu^{++} ion is located at sites of octahedral or trigonal symmetry, it has often been possible to view Jahn-Teller coupling as a mechanism which induces a tetragonal distortion. The resulting tetragonal component of crystal field splits the ground orbital doublet, leaving the Cu^{++} ground state as a spin doublet.

In such cases, there are no zero order matrix elements of the spin-orbit interaction. All admixtures of excited orbitals into the Cu^{++} ground state by spin-orbit terms of higher order are very small. Moreover, the second order matrix element between the states split by Jahn-Teller coupling, $|\epsilon\rangle$ and $|\theta\rangle$, is of negligible magnitude, unless the crystal field at the Cu^{++} site contains a large trigonal component. For these reasons, it has usually been possible to justify the use of perturbation techniques when relating theoretical parameters of the Cu^{++} systems to those measured for the experimental spin-Hamiltonian.

When perturbation theory is used in formulating spin-Hamiltonian terms which are correct to second order, the true Hamiltonian is written as

$$H = H_0 + H_1 + H_2 \quad (10)$$

H_0 is the electrostatic interaction (including crystal field effects), H_1 is the spin-orbit coupling interaction and H_2 is the sum of remaining magnetic and quadrupole interactions. The eigenstates of H_0 , considered as zero order states, are represented by $|kM_s\rangle$ where $k=\epsilon, \theta, O, C$, and S , and where $M_s=\pm 1/2$ are the spin states. Then the matrix $\langle \epsilon M'_s | H_1 + H_2 | \epsilon M_s \rangle$ represents the zero order contribution to the spin-Hamiltonian. It contains no terms linear in the orbital angular momentum operators L_x , L_y , and L_z since $\langle \epsilon M'_s | L_p | \epsilon M_s \rangle = 0$ for $p=x, y, z$. The off-diagonal matrix elements, $\langle k M'_s | H_1 + H_2 | \epsilon M_s \rangle$, on the other hand, admix excited orbitals into the ground orbital through spin-orbit coupling. As a result, the first order ground spin doublet becomes

$$|\epsilon M_s\rangle' = |\epsilon M_s\rangle + \sum_k \frac{\langle k M'_s | \lambda \vec{L} \cdot \vec{S} | \epsilon M_s \rangle}{-\Delta_k} |k M'_s\rangle \quad (11)$$

The second order contributions to the spin-Hamiltonian are obtained by evaluating $(H_1 + H_2)$ within the states $|\epsilon M_s\rangle$, and neglecting third order terms.

2. g-Factor

Contributions to the \tilde{g} tensor of the spin-Hamiltonian defined in Eq. (9) arise from consideration of the electronic Zeeman term,

$$H_Z = \beta \vec{H} \cdot (g_0 \vec{S} + \vec{L}) \quad (12)$$

To a second order approximation in spin-orbit coupling, the \tilde{g} tensor elements are

$$g_{pq} = g_0 \delta_{pq} - 2\lambda \Lambda_{pq} \quad (13)$$

where

$$\Lambda_{pq} = \sum_n \frac{\langle \epsilon | L_p | n \rangle \langle n | L_q | \epsilon \rangle}{\Delta_n} \quad (14)$$

With the aid of Table H3 in Appendix H, the principal components of the spin-Hamiltonian \tilde{g} tensor are defined in the (x, y, z) co-ordinate system to be:

$$g_{xx} = g_0 - 2\lambda \left\{ \frac{\sin^2 \alpha (3\cos^2 \alpha - 1)^2}{\Delta_\theta} + \frac{3\sin^2 \alpha \cos^2 \alpha}{\Delta_0} + \frac{\cos^2 \alpha (3\sin^2 \alpha - 1)^2}{\Delta_c} \right\},$$

$$g_{yy} = g_0 - \frac{2\lambda}{\Delta_s},$$

$$g_{zz} = g_0 - 2\lambda \left\{ \frac{\cos^2 \alpha (3\cos^2 \alpha - 1)^2}{\Delta_\theta} + \frac{3\sin^4 \alpha}{\Delta_0} + \frac{\sin^2 \alpha (3\cos^2 \alpha + 1)^2}{\Delta_c} \right\}, \quad (15)$$

where $\alpha = 47.5^\circ$. Particularly noteworthy in these expressions is the occurrence of terms involving Δ_θ , which, although zero for octahedral complexes ($\alpha = 54.3^\circ$), are far too large to be neglected in the cases such as Ca(OH)_2 .

For numerical evaluation of the various parameters, λ/Δ_i , account should be taken of covalency effects by substituting ζ_n and ζ_i for λ , and by multiplying the matrix elements of Table H3 by the appropriate orbital reduction factors k_n and k_i .⁴⁷⁻⁵⁰ Moreover, the \tilde{g} tensor elements should be expressed correctly to third order perturbation.⁵¹⁻⁵³ Third order expressions, however, are not easily derived because of their complexity. In fact, it is more convenient to evaluate these parameters by a computer fitting process which involves direct diagonalization of a Hamiltonian containing all crystal field, spin-orbit coupling, and Jahn-Teller coupling interactions. This latter procedure will be discussed in detail in section F.

3. Hyperfine Structure

The magnetic hyperfine interaction between electronic and nuclear magnetic moments is given in operator form by the electronic Hamiltonian term⁵⁴

$$V_I = -P\{(\kappa - 4/7)\tilde{S} \cdot \tilde{I} + 1/7(\tilde{L} \cdot \tilde{S})(\tilde{L} \cdot \tilde{I}) + (\tilde{L} \cdot \tilde{I})(\tilde{L} \cdot \tilde{S}) - \tilde{L} \cdot \tilde{I}\}, \quad (16)$$

where $P = 2\gamma\beta\beta_n \langle r^{-3} \rangle$ and κ is the hyperfine contact constant. To a second order approximation in spin-orbit coupling, the hyperfine interaction contribution to the spin-Hamiltonian of Eq. (9) is specified by the hyperfine tensor \tilde{A} , with elements

$$A_{pq} = -P \left[(\kappa \delta_{pq} + 2\lambda \Lambda_{pq}) + 2/7 (l_{pq} - \lambda \Lambda'_{pq}) \right] S_q I_p. \quad (17)$$

P , κ , and Λ_{pq} have been defined previously, and

$$l_{pq} = 1/2 \langle \epsilon | L_p L_q + L_q L_p | \epsilon \rangle - 1/3 L(L+1) \delta_{pq}, \quad (18)$$

$$\Lambda'_{pq} = 1/2 \sum_{t,r} \epsilon_{ptr} \sum_n \langle \epsilon | L_r | n \rangle \langle n | L_q L_t + L_t L_q | \epsilon \rangle (k_r / \Delta_n). \quad (19)$$

The k_r are the orbital reduction factors mentioned previously. Tensor elements Λ_{pq} , l_{pq} and Λ'_{pq} , which are tabulated in

Appendices I, J, and K, include the appropriate orbital reduction factors. With the aid of these tables, the elements of the spin-Hamiltonian tensor, \tilde{A} , are approximated to second order by the expressions:

$$\frac{-A_{xx}}{P} = \kappa - \Delta g_{xx} - \frac{2}{7} - \frac{2\lambda}{7} \left\{ \left(\frac{0.412}{\Delta_{\theta}} + \frac{0.719}{\Delta_c} + \frac{0.301}{\Delta_o} \right) k_{\parallel} + \frac{1.500}{\Delta_s} k_{\perp} \right\};$$

$$\begin{aligned} \frac{-A_{yy}}{P} = \kappa - \Delta g_{yy} - \frac{2}{7} - \frac{2\lambda}{7} \left\{ \left(\frac{0.412}{\Delta_{\theta}} + \frac{0.719}{\Delta_c} + \frac{0.301}{\Delta_o} \right) k_{\parallel} \right. \\ \left. + \left(\frac{0.111}{\Delta_{\theta}} + \frac{0.432}{\Delta_c} + \frac{1.116}{\Delta_o} \right) k_{\perp} \right\}; \end{aligned}$$

$$\frac{-A_{zz}}{P} = \kappa - \Delta g_{zz} + 4/7 + \frac{2\lambda}{7} \left(\frac{0.111}{\Delta_{\theta}} + \frac{0.432}{\Delta_c} + \frac{1.116}{\Delta_o} + \frac{1.500}{\Delta_s} \right) k_{\perp};$$

$$\begin{aligned} \frac{-A_{xz}}{P} = 2\lambda \left\{ \left(\frac{-0.019}{\Delta_{\theta}} + \frac{0.106}{\Delta_c} + \frac{0.232}{\Delta_o} \right) k_{\parallel} + \left(\frac{-0.034}{\Delta_{\theta}} + \frac{0.372}{\Delta_c} \right. \right. \\ \left. \left. + \frac{0.406}{\Delta_o} \right) k_{\perp} \right\}; \end{aligned}$$

$$\begin{aligned} \frac{-A_{zx}}{P} = 2\lambda \left\{ \left(\frac{-0.034}{\Delta_{\theta}} + \frac{0.372}{\Delta_c} + \frac{0.406}{\Delta_o} \right) k_{\parallel} + \left(\frac{-0.104}{\Delta_{\theta}} + \frac{0.347}{\Delta_c} \right. \right. \\ \left. \left. + \frac{0.446}{\Delta_o} \right) k_{\perp} \right\}. \quad (20) \end{aligned}$$

It should be noted that \tilde{A} is a traceless asymmetric tensor which contributes off-diagonal terms to the hyperfine tensor. As a result, failure of the z axes of experimental \tilde{g} and \tilde{A} tensors to coincide should not prove surprising.

4. Quadrupole Interaction

The nuclear electric quadrupole interaction is given in operator form by the electronic Hamiltonian term^{55,56}

$$V_Q = - \frac{e^2 Q}{I(2I-1)} \langle r_q^{-3} \rangle \xi \frac{1}{2} [3(\vec{L} \cdot \vec{I})^2 + 3/2(\vec{L} \cdot \vec{I}) - L(L+1)I(I+1)] \quad (21)$$

where $\xi = 2/2I$ for Cu^{++} . Because of the small magnitude of this interaction, it is necessary to retain only the diagonal terms. Hence, to a first order approximation, Eq. (21) reduces to the form

$$V_Q = \left[- \frac{3e^2 Q}{2I(2I-1)} \langle r_q^{-3} \rangle \xi \right]_{p,q} \frac{1}{2} \frac{I_p I_q}{p q} \quad (22)$$

Assuming that $\langle r_q^{-3} \rangle = 8.265$ a.u., the term in brackets has a value of 5.3G, and the non-zero components of the spin-Hamiltonian \bar{Q} tensor are $Q_{zz} = 10.6\text{G}$ and $Q_{xx} = Q_{yy} = -5.3\text{G}$.

Moreover, $Q' = |Q_{xx} - Q_{yy}| = 0$.

F. THE JAHN-TELLER COUPLING INTERACTION (STATIC DEFORMATION TERM)

At this point, consideration must be given to the effect of Jahn-Teller coupling between the Cu^{++} ion and the $\text{Ca}(\text{OH})_2$ lattice. The Jahn-Teller theorem predicts the existence of at least one distortion of an XY_6 complex from a highly symmetrical arrangement. The possible distortions from an equilibrium configuration are defined by the set of normal co-ordinates listed in Appendix L. They have the property of transforming in the same way as the irreducible representations of the point group D_{3d} , and can be viewed as small departures from the D_{3d} configuration.

Assuming that the OH^- ions are not necessarily at their equilibrium positions, a position vector $\vec{S}_i = \vec{R}_i + \vec{\sigma}_i$

is defined to specify the location of the i^{th} ion. \vec{R}_i defines its equilibrium location and $\vec{\sigma}_i$, its displacement from equilibrium. With the further assumption that $|\vec{\sigma}_i| \ll |\vec{R}_i|$, the electrostatic energy of the $\text{Ca}(\text{OH})_2: \text{Cu}^{++}$ system is given by the expansion

$$V = \sum_m \left[\frac{4\pi}{5} A Z_{2m}^* r^2 z_{2m} + \frac{4\pi}{9} F Z_{4m}^* r^4 z_{4m} \right], \quad (23)$$

where $A = - \frac{|ee'|}{s^3}$ and $F = - \frac{|ee'|}{s^5}$. The Z_{im}^* and Z_{im} ,

are functions of the polar angles of \vec{S}_i and \vec{r} , respectively. By expanding Eq. (23) in a Taylor series about the equilibrium configuration, the crystal field interaction is given in terms of ionic displacement, $\vec{\sigma}_i$, as

$$V = V_0 + \sum_i (\vec{\nabla} V)_0 \cdot \vec{\sigma}_i. \quad (24)$$

V_0 and $(\vec{\nabla} V)_0$ are evaluated at equilibrium. The first term in this series, V_0 , is identical with the trigonal crystal field term, V_T , defined by Eq. (6). The second term, linear in configurational distortion, is the Jahn-Teller coupling as defined by van Vleck.⁵⁷

The term $\sum_i (\vec{\nabla} V)_0 \cdot \vec{\sigma}_i$ was expanded by Holuj et al.⁵⁸ for the $\text{Ca}(\text{OH})_2$ lattice. Taking only the Z_{2m}^* terms of V into account, $\sum_i (\vec{\nabla} V)_0 \cdot \vec{\sigma}_i$ was found to span the entire set of normal co-ordinates listed in Appendix L. Each term in the expansion exists as a product of an electronic operator, an orbit-lattice coupling coefficient, and a normal co-ordinate. The only terms which actually come into play in Jahn-Teller coupling are those which lower the energy of the Cu^{++} system by splitting its ground doublet. For octahedral complexes, this splitting is related to deformations which transform as the θ and ϵ components of the irreducible representation

E_g of the point group O_h .⁵⁹ Consequently, it is assumed that similar deformations will be responsible for lifting the electronic degeneracy here. As illustrated in Fig.L-1, these types of distortion are present in the $\text{Ca}(\text{OH})_2$ lattice. They occur as linear combinations of normal co-ordinates, and are defined as

$$\begin{aligned} Q_\theta &= q_1^C \sin\gamma - q_2^C \cos\gamma, \\ Q_\epsilon &= -q_1^S \sin\gamma + q_2^S \cos\gamma. \end{aligned} \quad (25)$$

In such cases where the Born-Oppenheimer condition is satisfied, the degenerate levels are separated by an energy which is linearly dependent on the magnitude of Q_θ or Q_ϵ . Considering only those terms of $\sum_i (\vec{\nabla}V)_0 \cdot \vec{\sigma}_i$ which contain Q_θ and Q_ϵ , matrix elements of the Jahn-Teller coupling interaction have been evaluated in the manifold of $|\theta\rangle$ and $|\epsilon\rangle$. They have the form

$$W_{JT} = -C_E (Q_\theta \tilde{U}_\theta + Q_\epsilon \tilde{U}_\epsilon), \quad (26)$$

where

$$C_E = \frac{15\sqrt{3}}{14} \frac{A}{R} \langle r^2 \rangle \sin\alpha \sin\gamma (\sin\alpha \sin\gamma + 4\cos\alpha \cos\gamma). \quad (27)$$

\tilde{U}_θ and \tilde{U}_ϵ are identical to the Pauli matrices $-\vec{\sigma}_z$ and $\vec{\sigma}_x$.

The Jahn-Teller distortions, Q_θ and Q_ϵ , can be re-expressed in polar co-ordinates ρ and θ as

$$\begin{aligned} Q_\theta &= \rho \cos\theta, \\ Q_\epsilon &= \rho \sin\theta, \end{aligned} \quad (28)$$

where ρ defines their magnitude and θ , their direction. The distortion magnitudes are limited at some finite, non-zero value by the presence in the lattice of quasi-elastic forces. These forces cause the energy of both ground orbitals to increase by an amount quadratic in their magnitude. The distortion orientations, as well, are restricted when account is

taken of small anharmonic terms of order higher than second in Q_θ and Q_ϵ . For instance, the "warping term" introduced by Öpik and Pryce,⁶⁰

$$V_{OP} = A_3 Q_\theta (Q_\theta^2 - 3Q_\epsilon^2) = A_3 \rho^3 \cos 3\theta, \quad (29)$$

reduces the number of stable distortions to three. It is apparent that a negative value of A_3 requires that θ equal 0° , 120° or 240° , and moreover, that potential barriers of magnitude $2|A_3\rho^3|$ separate these allowed distortions with regard to variations in the parameter θ .

Experimental data has indicated that Jahn-Teller coupling in the $\text{Ca(OH)}_2:\text{Cu}^{++}$ system is restricted entirely to the Q_θ distortion. As a result, $\theta = 0^\circ$, and the electronic energies of the ground orbital doublet are

$$E_{|\epsilon\rangle} = E_0 - C_E \rho + \frac{1}{2} K \rho^2, \quad (30)$$

and

$$E_{|\theta\rangle} = E_0 + C_E \rho + \frac{1}{2} K \rho^2. \quad (31)$$

K is the elastic constant of the lattice in the absence of Jahn-Teller ions. The minimum of $E_{|\epsilon\rangle}$ is easily shown to occur when

$$\rho = \rho_{\text{MIN}} = \frac{C_E}{K} = \frac{A_\theta}{2C_E} \quad (32)$$

and

$$E_{|\epsilon\rangle} = E_0 - \frac{C_E^2}{2K} \quad (33)$$

For the stable configuration, the magnitude of the Jahn-Teller splitting for the 2E_g ground orbitals is $\frac{2C_E^2}{K}$.

G. THE COMPLETE ELECTRONIC HAMILTONIAN

As indicated previously, the approximate expressions derived by perturbation theory for spin-Hamiltonian \tilde{g} and \tilde{A} tensor elements must be correct to at least third order in spin-orbit coupling. Only then a satisfactory evaluation of system parameters k_1 , δ , κ , Q_0/R , ζ and Δ_1 is ensured. Because of the complicated nature of the third order expressions, a more convenient method of parameter evaluation is introduced. The parameters are treated as adjustable constants in the full electronic orbital Hamiltonian which contains crystal field, spin-orbit coupling and static Jahn-Teller deformation interactions. This Hamiltonian is defined by the expression

$$H_{ORB} = V_T + \zeta_n k_n S_z L_z + \zeta_1 k_1 (S_x L_x + S_y L_y) + \frac{15}{2} \sqrt{\frac{4\pi}{5}} \frac{|ee'| \langle r^2 \rangle}{R^3} \frac{Q_0}{R} (\sin^2 \gamma Z_{22}^C + 2 \sin \gamma \cos \gamma Z_{21}^C) \quad (34)$$

Matrix elements of H_{ORB} within the manifold spanned by Z_{2m} are tabulated in Appendix M. For a given set of parameters, this matrix is diagonalized and the corresponding ground state eigenfunction is determined. Theoretical \tilde{g} and \tilde{A} tensor elements are then calculated for this ground orbital and compared with experimental values. This procedure is repeated for many sets of parameters. The set which provides the best agreement is chosen. All additional Jahn-Teller computations are based on these parameters. Although agreement between calculated and experimental spin-Hamiltonian values could probably be improved by the introduction of additional parameters, this will not greatly affect the values obtained for ζ , k_1 , κ , $\frac{Q_0}{R}$, δ and Δ_1 .

H. DYNAMIC JAHN-TELLER EFFECT

For very low temperatures, strong Jahn-Teller coupling, and large energy barriers between distorted configurations, the XY_6 complexes are equally distributed among three equivalent vibronic ground states. Each individual complex is essentially frozen into one configuration for a period of time that is long, compared to that for an E.P.R. transition to occur. As a result, the observed low, temperature E.P.R. spectrum should consist of three equally populated sets of transitions, each exhibiting identical characters, but differing only in the directions of their respective magnetic axes.

At higher temperatures, low lying vibronic states become populated at the expense of the ground vibronic triplet according to the Boltzmann distribution. This leads to a corresponding reduction in the intensity of the low temperature spectrum, and may even result in the appearance of new spectra. According to O'Brien,⁶¹ the first excited vibronic state belongs to the A_1 representation. An E.P.R. spectrum resulting from this state is described by the isotropic g factor:

$$g_{A_1} = g_0 + 4u \quad , \quad (35)$$

where it is assumed that $u = \frac{\lambda}{\Delta_s}$ (approximately). Consequently, the thermal population of excited vibronic states is one possible mechanism that could be responsible for the appearance of a spectrum associated with a dynamic Jahn-Teller effect.

Alternatively, Abragam and Pryce⁶² viewed the high temperature spectrum as an average of the three spectra observed at lower temperatures. A mechanism which may be responsible for such averaging is portrayed in Fig.3.

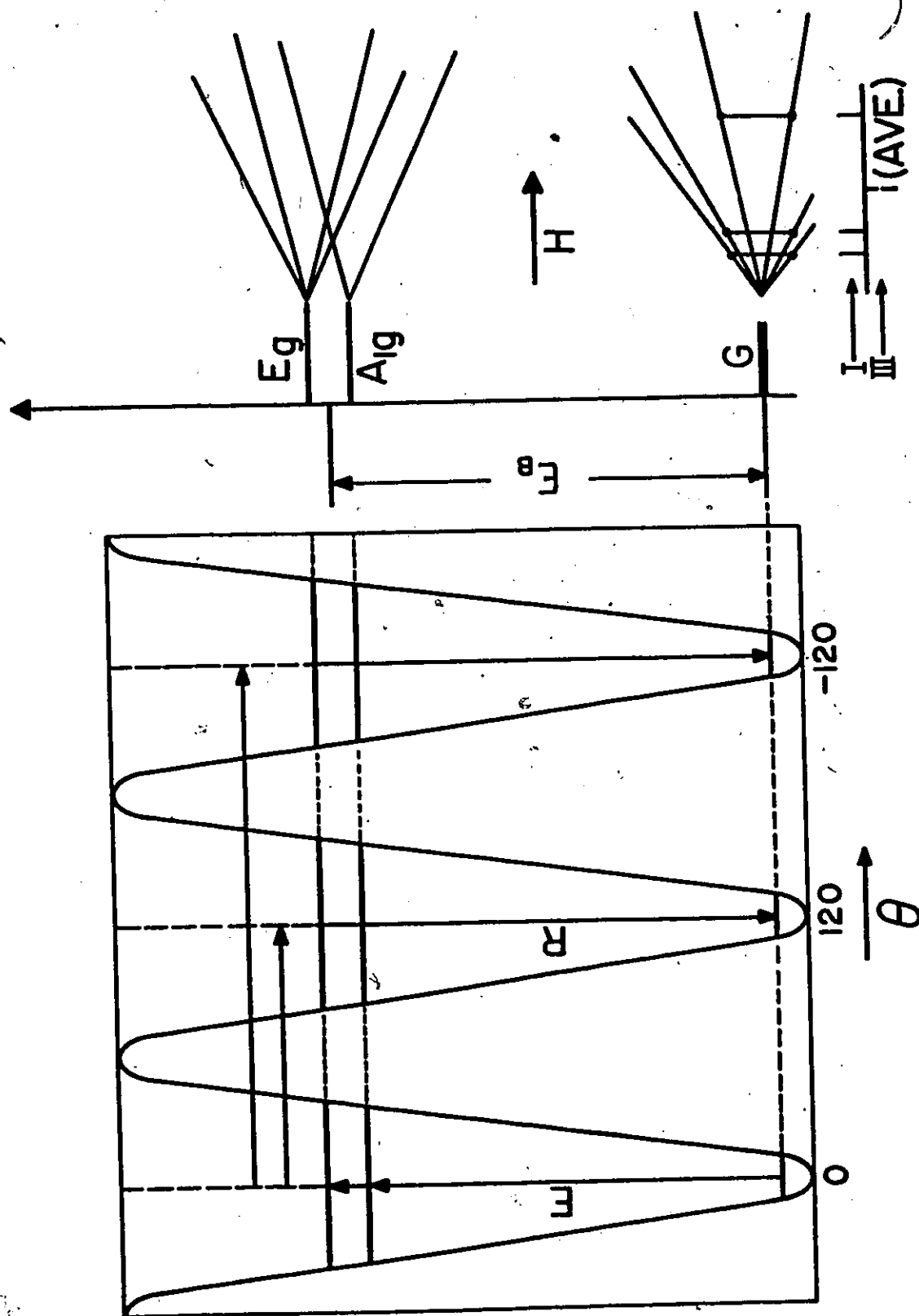


Fig.3 Averaging of the low temperature Cu^{++} spectrum by thermal reorientation of the elongated octahedral complex.

The XY_6 complex is raised by phonon absorption to some excited vibronic state, from which it can decay with equal probability into any one of the three vibronic ground states associated with distorted configurations. The participating excited states lie high enough relative to the energy barrier so that tunneling from one distortion to another is possible. At higher temperatures, a larger number of phonons with enough energy to activate such reorientations are available. The increased probability of a transition from one distorted configuration to another reduces the time, τ , required for configurational reorientation. When τ becomes short with respect to the time of an E.P.R. transition, the complex assumes all three distorted configurations many times during the transition. In this case, the observed spectrum is described by the averaged parameters of the individual low temperature spectra. These are derived in Appendix N, and are given by the following relations:

$$g_{\text{ave}} = g_{zz} \cos^2 \alpha + g_{xx} \sin^2 \alpha$$

$$g_{\text{ave}} = \frac{1}{2}(g_{zz} \sin^2 \alpha + g_{xx} \cos^2 \alpha + g_{yy}) \quad (36)$$

Analogous equations hold for the hyperfine tensor. If this is the mechanism responsible for the high temperature spectrum, then the reorientation time, τ , is given by:

$$\tau \propto \exp\left(\frac{E_B}{kT}\right) \quad (37)$$

For such a case, the intensity of the low temperature spectrum is proportional to τ , while that of the high temperature spectrum is proportional to $1/\tau$. Hence, a temperature variation study of spectral intensities can be expected to establish the size of the energy barrier separating distorted configurations, correct at least to an order of magnitude.

IV INSTRUMENTATION AND MEASUREMENT TECHNIQUES

A. K Band Spectrometer

A block diagram is presented in Fig. 4 of the bridge type of spectrometer used for anisotropy and temperature dependence studies of the Cu^{++} spectra over the temperature range 78°K to 300°K .

The cavity assembly is illustrated in greater detail in Fig. 5. It consists of a pyrex cylinder coated on the inside with silver oxide paint, and then baked at 710°C until the paint was bonded to the glass. After removal of the surface oxide, gold was sputtered onto the exposed silver surface. A brass cage and bottom plate are used to mount the cavity to the waveguide, and to support a crystal rotating mechanism.⁶³ This cavity operates in the TE_{011} mode with a loaded Q of about 2,500.

Experiments at any temperature lower than room temperature are possible with this system. A plastic cup sealed with glycerine to the brass flange directly above the cavity, allows the cavity assembly to be evacuated while immersed in a liquid refrigerant. A heater attached to the bottom plate of the cavity, can be used to establish a temperature gradient along the length of the cavity cage. Thermal conduction from the sample to the cage via the quartz sample pin and the rotator mechanism, and radiation transfer from the sample to its surroundings, establish an equilibrium temperature above the refrigerant boiling point temperature. The temperature of the sample is monitored by an uncalibrated copper-constantan thermocouple, which enters the cavity through the bottom plate and extends to the sample along the cavity axis. Accuracy in temperature measurements is estimated to be of the order of $\pm 2^{\circ}\text{K}$.

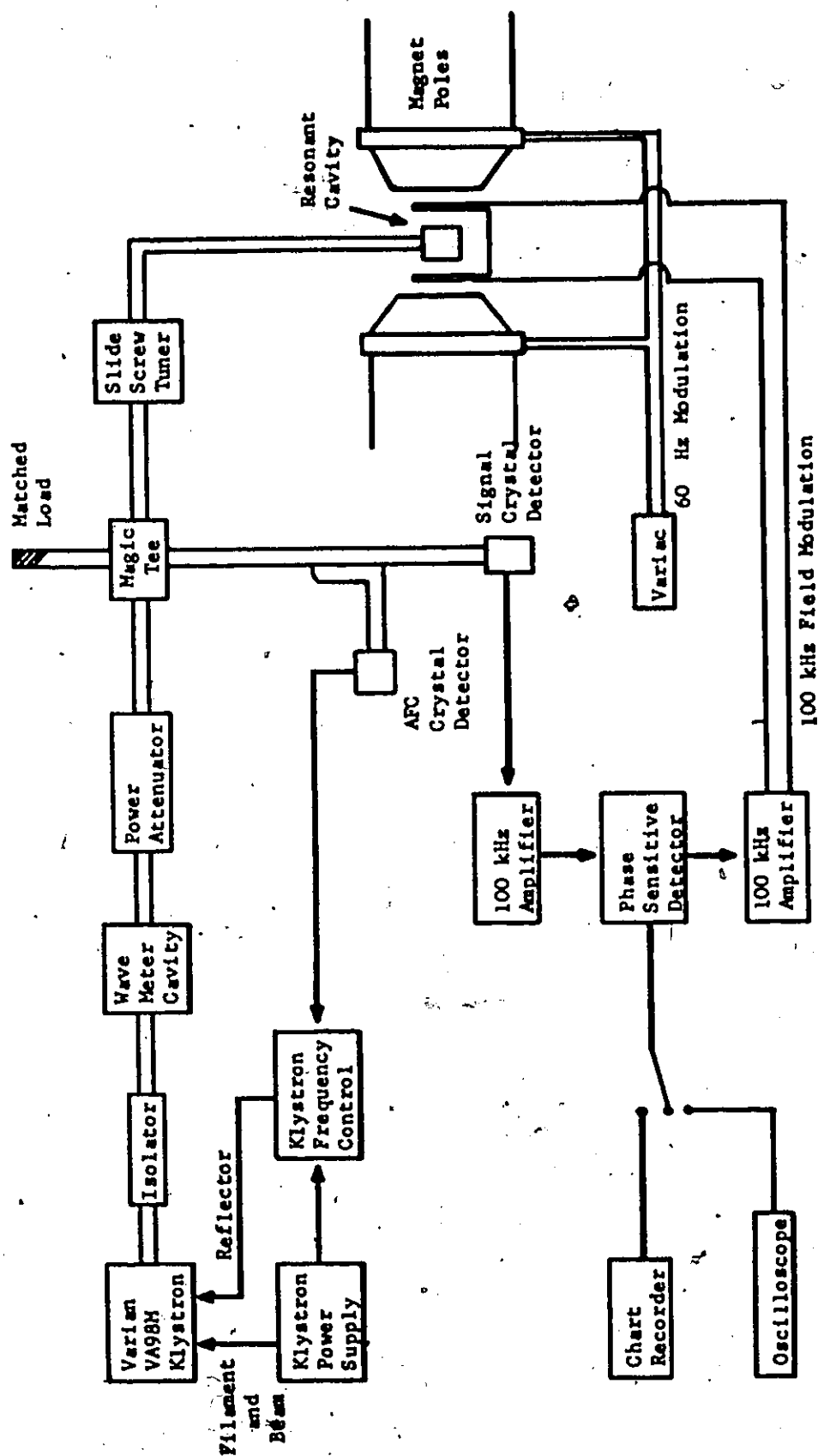


Fig. 4 Block diagram of the K band E.P.R. spectrometer.



Fig.5 The K band cavity assembly.

B. X Band Spectrometer

An X band spectrometer of the type illustrated in Fig.6, was employed for studies involving the application of uniaxial stress to the sample in the temperature range 4.2°K to 300°K . This spectrometer is easily converted from bridge to superheterodyne operation. Superheterodyne operation was utilized only for experiments at 4.2°K when saturation effects required a 50db reduction of the microwave power.

The X band cavity assembly includes all the facilities described above for the K band assembly. In addition, such features as an internal 100 kHz modulation loop, and an optional polystyrene vise for uniaxial stress experiments, are available. These modifications are shown in Fig.7. The bottom half of the vise is fitted into the bottom plate of the cavity. The top half terminates in a long stainless steel rod, which extends through an O-ring vacuum seal at the top of the apparatus. A force is supplied to this rod by a lever and hydraulic piston system. The magnitude of this force at the sample, is directly proportional to the weight hanging from the lever. When the vise assembly is used, the sample rests on a flat brass disc which sits on top of a polystyrene rod. A heater is attached to a brass finger which extends up the axis of the polystyrene rod and the cavity to terminate at the brass disc. This arrangement allows the temperature of the sample to be varied while it is under stress. An uncalibrated copper-constantan thermocouple located at the bottom of the brass disc was used to monitor temperatures.

C. E.P.R. Measurements

Experiments were carried out using 12 inch and 15 inch Varian magnets, both equipped with Fieldial regulation, as well as the K band and X band spectrometer systems discussed above. Klystron frequencies of about 9.2 GHz, were locked to the resonant frequencies of the sample cavities. E.P.R. signals were phase sensitive detected, using a 100 kHz magnetic

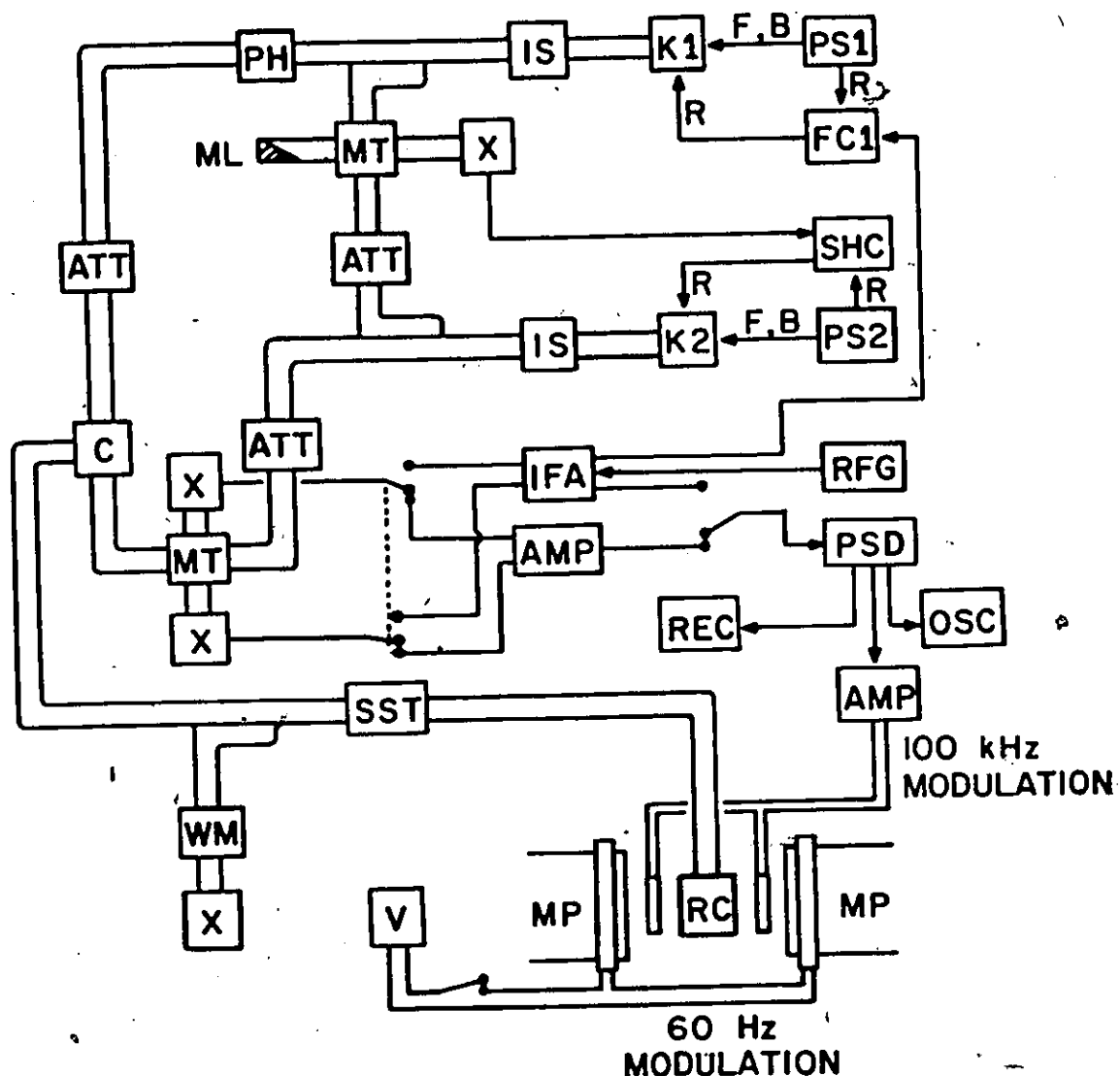


Fig.6 Block diagram of the X band E.P.R. spectrometer. Components are labelled as follows: K1,klystron 1; K2,klystron 2; PS1,power supply 1; PS2,power supply 2; FC1,klystron 1 frequency control; SHC,klystron 2 superheterodyne control; IS,isolator; PH,phase shifter; ATT,attenuator; ML,matched load; MT,magic tee; X,crystal detector; C,circulator; SST,slide screw tuner; WM,wave meter cavity; RC,resonant cavity; MP,magnet pole; IFA, IF amplifier; RFG, RF gain control; AMP,100 kHz amplifier; PSD,phase sensitive detector; REC, recorder; OSC,oscilloscope; V,variatic; P,filaments; B,beam; R,reflector.

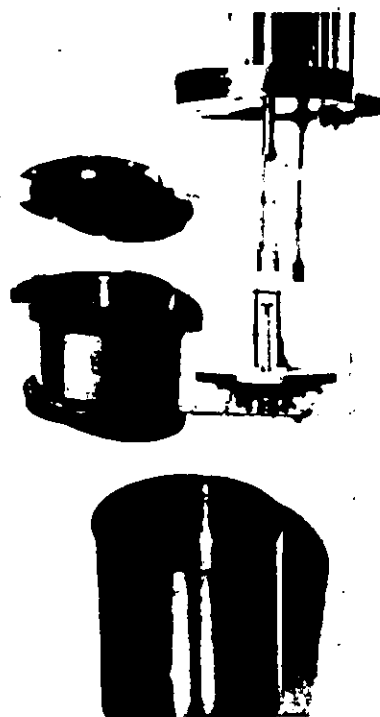


Fig.7 The X band cavity used in uniaxial stress and temperature dependence experiments.

field modulation technique. Application of an additional 60 Hz magnetic field modulation to the system, made it possible to observe first derivatives of the resonant lines on the oscilloscope. Resonant fields were measured by simultaneously superimposing the E.P.R. signal and a proton signal, obtained from an N.M.R. magnetometer, on a double-beam oscilloscope, and carefully noting the oscillation frequency of the magnetometer. All such E.P.R. measurements were calibrated to the resonant field of the well known DPPH radical which has an isotropic g-value of 2.0036. Errors in resonant field measurements are estimated to be less than 2G for spectra I, II, and IV which had line widths in the range 3G to 5G, and less than 4G for the broader lines of spectrum III.

V. EXPERIMENTAL OBSERVATIONS AND RESULTS

A. General Remarks

The E.P.R. spectra of $\text{Ca(OH)}_2\text{:Cu}^{++}$ and $\text{Ca(OD)}_2\text{:Cu}^{++}$ single crystals are very similar. The observed spectrum can be divided into two spectra, I and III, associated with a Jahn-Teller ion, and two additional spectra, II and IV, associated with non-Jahn-Teller ions. The spectra, I, II, and IV, each consist of three sets, labelled a, b, and c, of four hyperfine structure lines. All three sets of I are shown in Fig.8a for a general orientation of magnetic field(\vec{H}), where they are completely resolved. The doubling of each set is real. The spectrum is a superposition of the spectra of both the $^{63}\text{Cu}^{++}$ and the $^{65}\text{Cu}^{++}$ isotopes, which occur naturally with a relative abundance ratio of 69.1 : 30.9. At temperatures above 150°K , I is replaced by III, which is shown in Fig.8b.

Differences have also been observed between the spectra of the two samples. The line width of about 5G in the Ca(OH)_2 case is reduced to about 3G when the hydrogens are replaced by deuterons. This results in improved resolution, and makes possible the measurement of forbidden transitions ($\Delta m_I = \pm 1, \pm 2$), which arise from the electric quadrupole interaction. On the other hand, a superhyperfine structure is observed only for the Ca(OH)_2 samples. The hyperfine set, Ia, in Fig.8a indicates the presence of a variable number of superhyperfine subcomponents. Similar superhyperfine structure is observed for the non-Jahn-Teller spectra, II and IV.

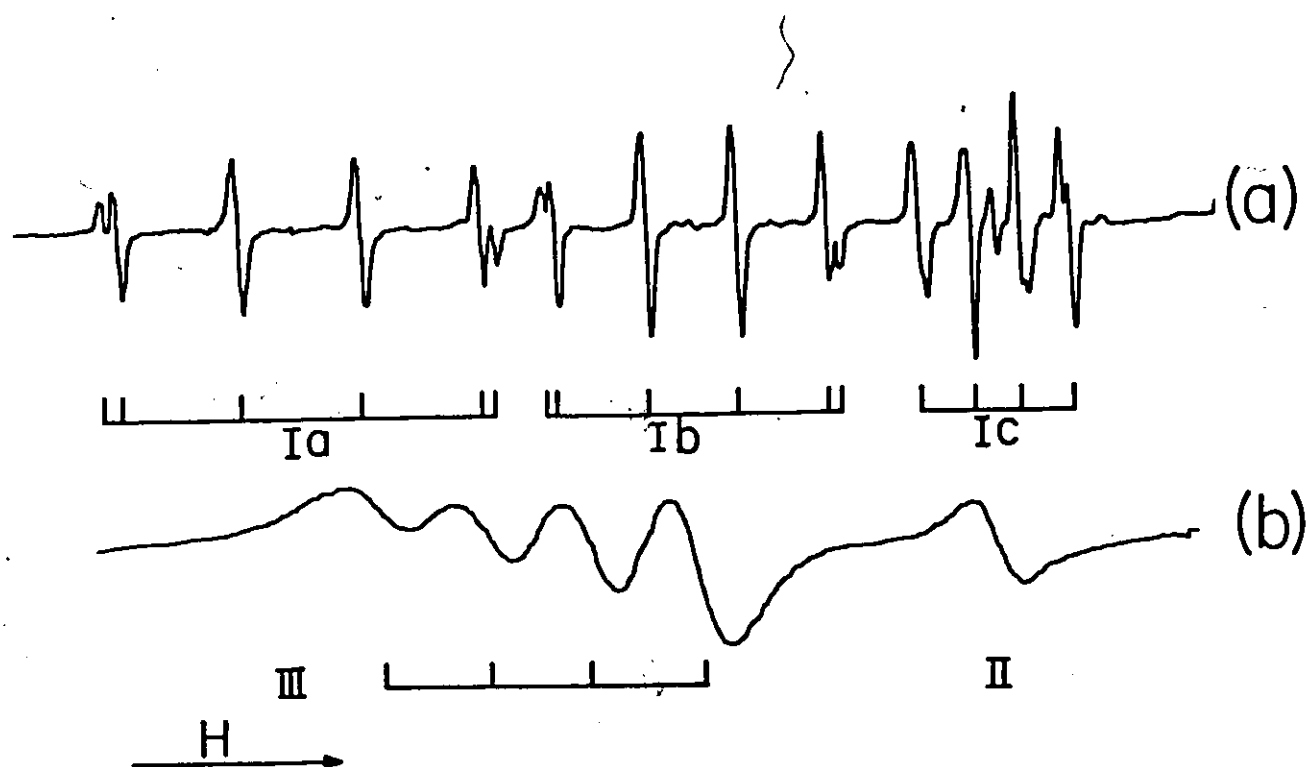


Fig. 8 Typical Jahn-Teller spectra of a $\text{Ca}(\text{OH})_2:\text{Cu}^{++}$ system for general orientations of H .
 (a) illustrates the three sets of I at 87°K.
 (b) is a room temperature example of III.

B. The Jahn-Teller Cupric Ion

1. Low Temperature Spectrum

i) Angular variation

Spectrum I is associated with the Jahn-Teller Cu^{++} ion for temperatures below 140°K . The angular variation is almost axial, but exhibits a pronounced asymmetry in the $(1\bar{2}10)$ plane which contains the x and z magnetic axes. This arises from a lack of coincidence of \vec{g} and \vec{A} tensor axes. For example, the hyperfine tensor is rotated 4.2° about the $(1\bar{2}10)$ direction (i.e. y axis) with respect to the \vec{g} tensor. Additionally, it is significant that the xy plane of the \vec{g} tensor approximately coincides with the plane containing hydroxyls 1, 2, 4, and 5 in Fig. 1. The z axis of the tensor is directed at a 13° angle to the line joining hydroxyls 3 and 6 in the normal Ca^{++} site.

Recordings of spectrum I are presented in Fig.9 for significant orientations of \vec{H} in the $(1\bar{2}10)$ plane. Throughout this plane, spectra Ib and Ic are superimposed, and for the special case of $\vec{H} // c$ axis, all three sets of spectra are coincident. Spectrum Ia collapses when the field is directed at -87° to the z axis. A similar collapse does not occur for an angle of -93° , clearly indicating the existence of asymmetry in this plane.

Angular variations of spectrum Ia in the xz and yz planes are illustrated in Figs.10 and 11 respectively, for a $\text{Ca}(\text{OD})_2$ host lattice. The region defined by $-60^\circ > \theta > -120^\circ$ expanded in order to show the variations observed for forbidden transitions over this range. The sudden appearance and rapid growth in intensity of these transitions relative to those normally allowed ($\Delta m_I = 0$), is indicated by the series of recordings in Fig.12.

ii) Quantitative Results for Spectrum I

Spectrum I was analysed using the spin-Hamiltonian given in Eq.(9). The results of this analysis are presented in Table I. α and β refer to the angles in the $(1\bar{2}10)$ plane between the symmetry axes of the \tilde{g} and \tilde{A} tensors and the c axis. Accurate quadrupole measurements are quoted only for Ca(OD):Cu^{++} , where parameter fitting was aided by the measurements of resolved transitions, $\Delta m_I = \pm 1, \pm 2$ over 60° intervals in both the xz and yz planes.

The spin-Hamiltonian parameters listed in column 5 were evaluated for $\text{Ca(OD)}_2: {}^{63}\text{Cu}^{++}$ by the methods outlined in chapter IIIG. They represent the best agreement that was obtained between experimental and calculated values. The hypothetical parameters given in Table II were used to arrive at these values, and hence, are assumed to be typical estimates of Cu^{++} parameters in Cu(OH)_2 and Cu(OD)_2 complexes.

iii) Superhyperfine Structure

In addition to the interactions described by the spin-Hamiltonian of Eq.(9), a partially resolved superhyperfine interaction was observed for $\text{Ca(OH)}_2:\text{Cu}^{++}$. Best resolution of the superhyperfine spectrum occurred when \vec{H} was along the $(10\bar{1}0)$ direction. Fig.13a shows that five superhyperfine components can be definitely counted for one hyperfine transition. The approximate magnitude of the splitting between components is $2.8 \pm 0.5G$. Significantly enough, for this \vec{H} direction, the four hydroxyl ions in the xy plane, (1,2,4, and 5 in Fig.1) are equivalent. It is expected that they should give rise to five superhyperfine components with relative intensities 1:4:6:4:1, if the interaction involves protons of only these four ions. Unfortunately, the resolution is not good enough to determine the relative intensities of the observed components accurately. Moreover, the series of recordings in Fig.13

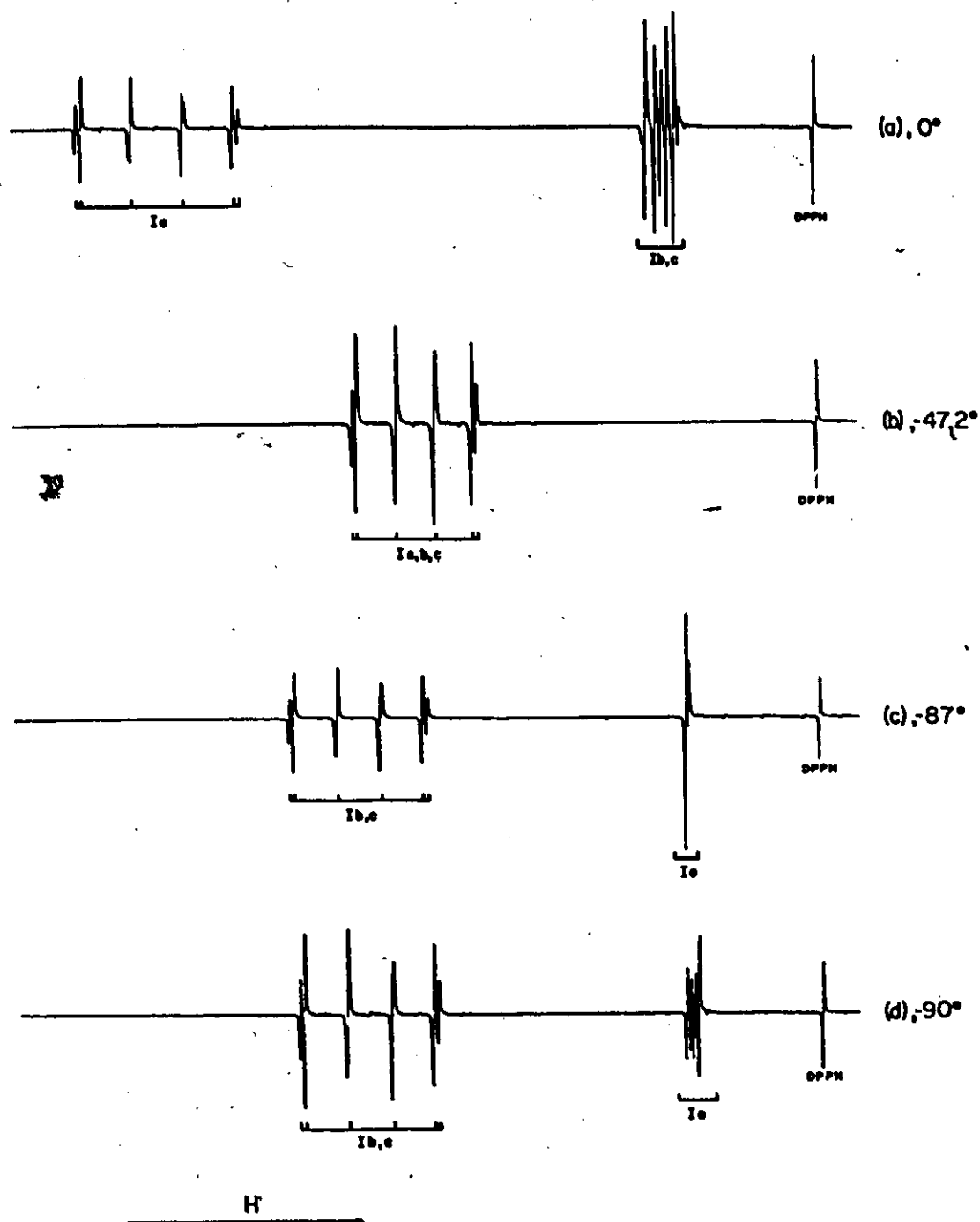


Fig.9 Recording of spectrum I for $\text{Ca}(\text{OD})_2:\text{Cu}^{++}$ at significant orientations of \vec{H} in the $(1\bar{2}10)$ plane at 80°K . Orientations of \vec{H} are given beside each trace as values of the azimuthal angle θ for the I_a system.

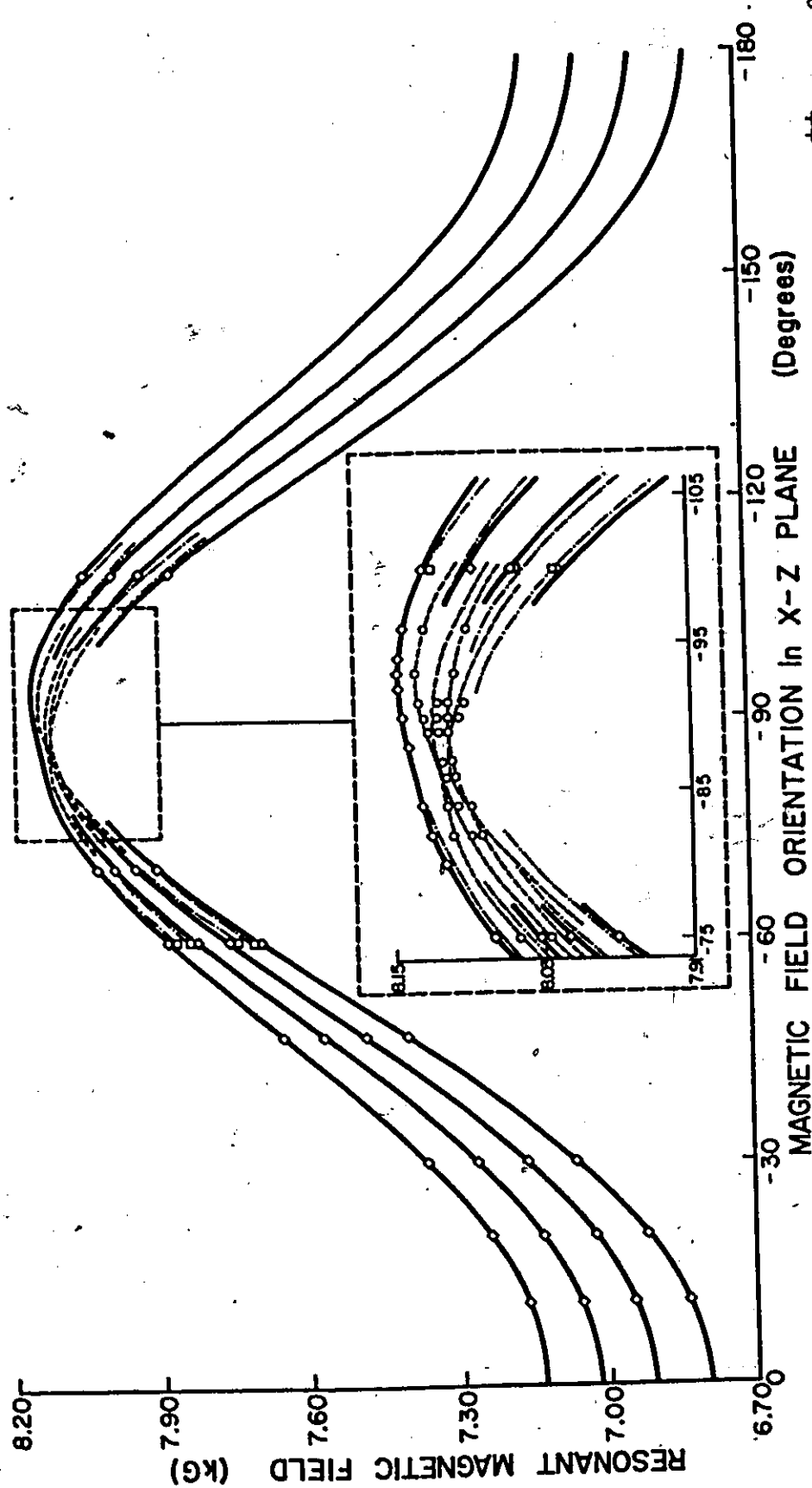


Fig. 10 Angular variation of spectrum Ia in the (11210) plane for $\text{Ca(OD)}_2:\text{Cu}^{++}$ at 80°K . Solid lines represent $\Delta m_I = 0$ transitions. Dash-dot lines represent $\Delta m_I = \pm 1$ transitions. Dashed lines represent $\Delta m_I = \pm 2$ transitions. The DPPH resonance occurs at 8.240 kg. Diamonds, squares, and circles indicate the measured resonant fields of $\Delta m_I = 0$, ± 1 and ± 2 transitions respectively.

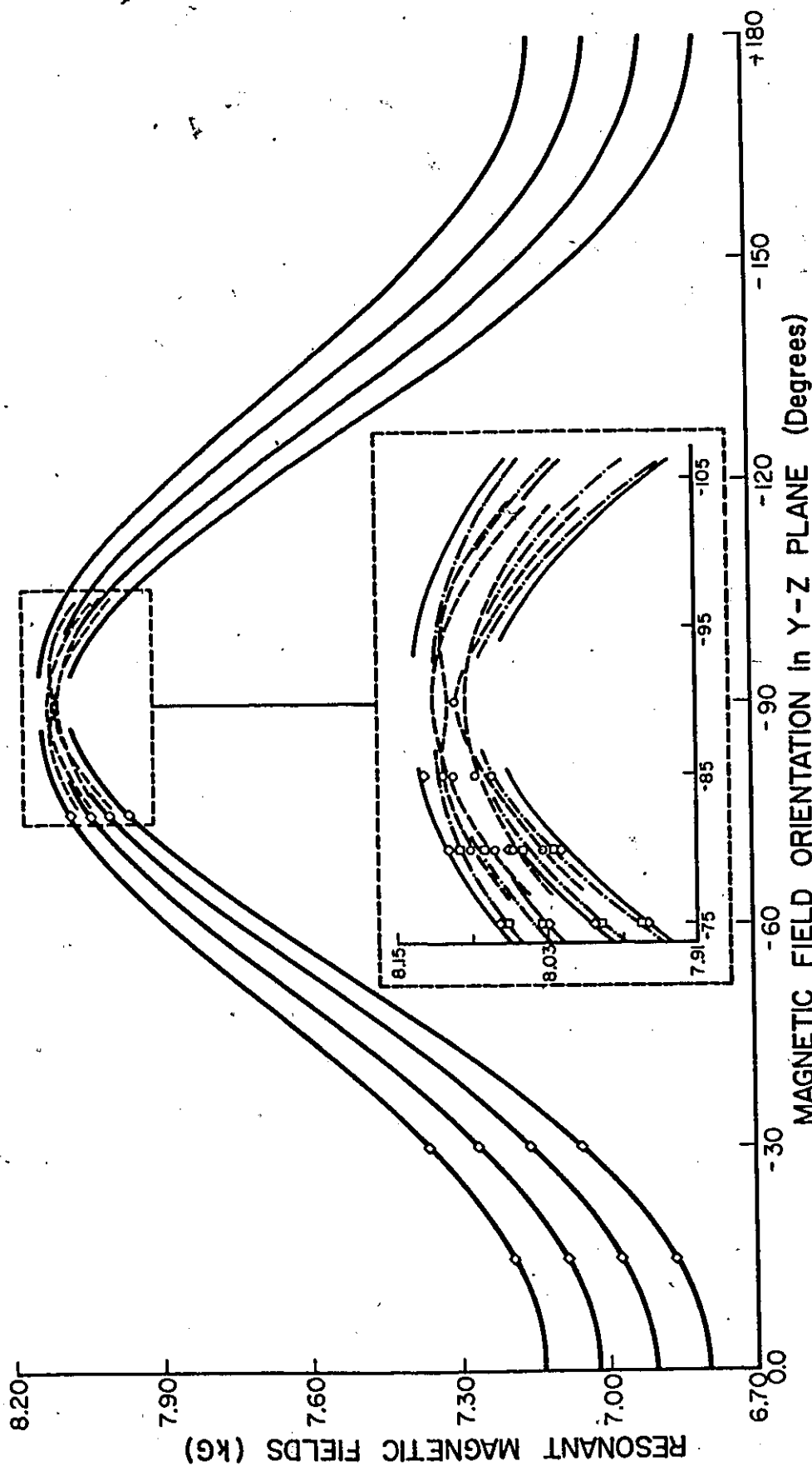


Fig. 11 Angular variation of spectrum Ia in the y-z plane for $\text{Ca(OD)}_2:\text{Cu}^{++}$ at 80°K . Solid lines represent $\Delta m_I = 0$ transitions. Dash-dot lines represent $\Delta m_I = \pm 1$ transitions. Dashed lines represent $\Delta m_I = \pm 2$ transitions. The DPPH resonance occurs at 8.240 kg. Diamonds, squares, and circles indicate the measured resonant fields of $\Delta m_I = 0$, ± 1 and ± 2 transitions respectively.

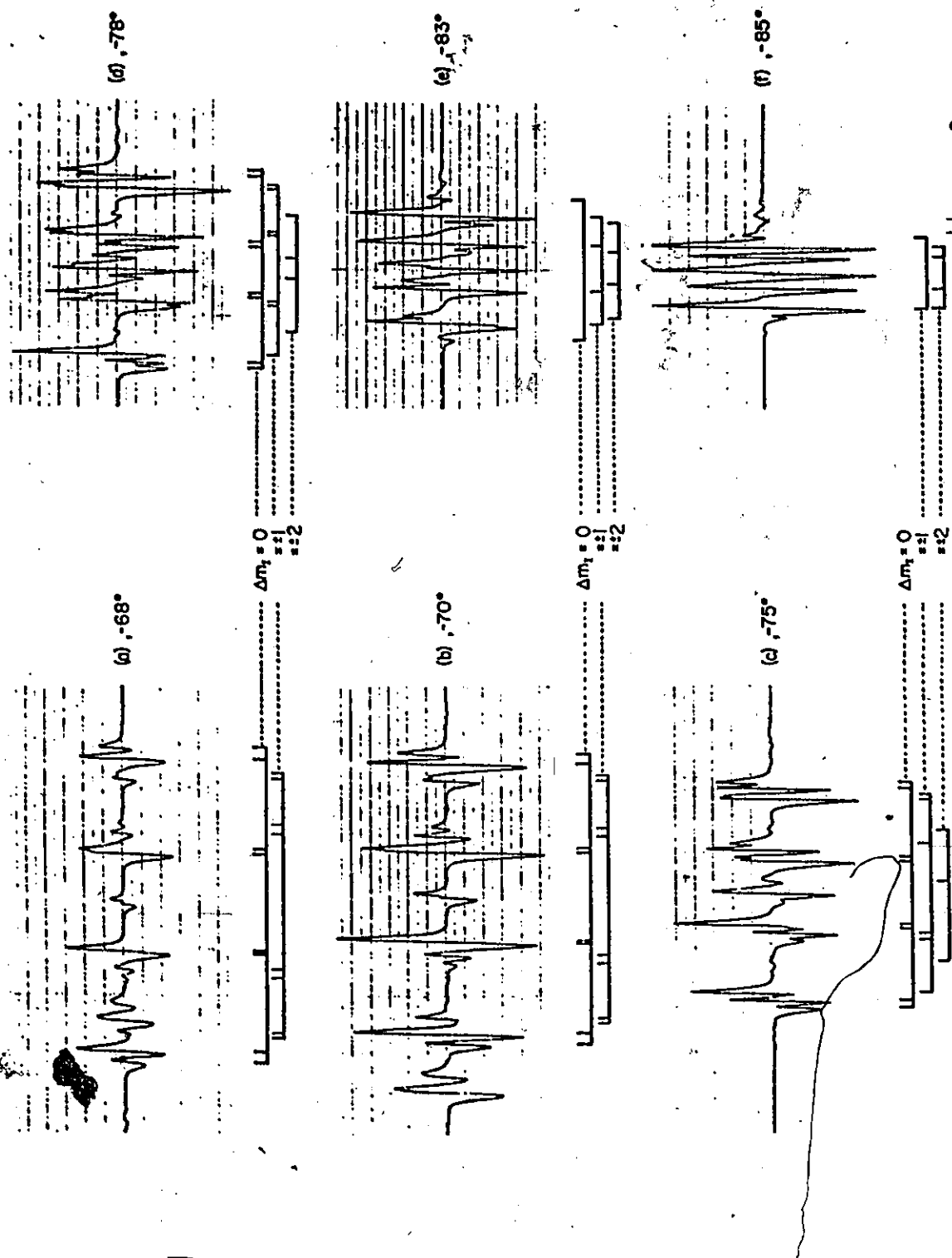


Fig. 12 Forbidden transitions of spectrum Ia observed for $\text{Ca(OD)}_2:\text{Cu}^{++}$ at 80°K over the range of azimuthal angle $-68^\circ \geq \theta \geq -85^\circ$ in the y-z plane.

TABLE I

Spin-Hamiltonian Parameters Of Jahn-Teller
Coupled $\text{Ca}(\text{OH})_2:\text{Cu}^{++}$ And $\text{Ca}(\text{OD})_2:\text{Cu}^{++}$ Complexes

PARAMETER	$\text{Ca}(\text{OH})_2:^{63}\text{Cu}^{++}$	$\text{Ca}(\text{OD})_2:^{63}\text{Cu}^{++}$	$\text{Ca}(\text{OD})_2:^{65}\text{Cu}^{++}$	CALCULATED [†] VALUE
g_{zz}	2.418 ± 0.002	2.416 ± 0.001	2.416 ± 0.001	2.415
g_{xx}	2.075 ± 0.002	2.074 ± 0.002	2.074 ± 0.002	2.083
g_{yy}	2.071 ± 0.002	2.076 ± 0.002	2.076 ± 0.002	2.066
$A_{zz}(\text{G})$	-132.0 ± 0.5	-133.8 ± 0.5	-144.0 ± 0.5	-132.2
$A_{xx}(\text{G})$	-2.4 ± 2.0	2.9 ± 2.0	3.5 ± 2.0	16.6
$A_{yy}(\text{G})$	-5.0 ± 5.0	-1.1 ± 2.0	-1.1 ± 2.0	-9.3
$A_{xz}(\text{G})$	10.0 ± 1.0	10.0 ± 1.0	10.0 ± 2.0	16.0
$Q_{zz}(\text{G})$	*	15.0 ± 1.5	15.0 ± 3.0	10.0
$Q_{xx}(\text{G})$	*	5.0 ± 3.0	5.0 ± 4.0	0
α	$47.2 \pm 0.5^\circ$	$47.5 \pm 0.5^\circ$	$47.2 \pm 0.5^\circ$	**
β	$51.5 \pm 1.0^\circ$	$51.5 \pm 1.0^\circ$	$51.4 \pm 1.0^\circ$	**

[†] Calculated values of Spin-Hamiltonian parameters were evaluated using the set of parameters listed in Table II.

* Value could not be determined from experimental data available.

** Value was not calculated.

TABLE II

Parameters Of Cu^{++} In $\text{Ca}(\text{OD})_2$. Estimated Values Are Based On Best Agreement With Experimental Measurements In The Manner Described In Chapter IIIG. - In Determining These Values, It Has Been Assumed That $A_{40} = -5040 \text{ cm}^{-1}$ And $\nu = \alpha = 47.5^\circ$.

PARAMETER	ESTIMATED VALUE	ESTIMATED ERROR
$\tau (\text{cm}^{-1})$	-625	± 50
k_{\parallel}	0.89	± 0.05
k_{\perp}	0.96	± 0.05
$\frac{Q_{\theta}}{R}$	0.18	± 0.02
κ	0.37	± 0.02
δ	2.03	± 0.20
$\Delta_{\theta} (\text{cm}^{-1})$	4,710	± 1500
$\Delta_{\text{O}} (\text{cm}^{-1})$	10,720	± 1000
$\Delta_{\text{C}} (\text{cm}^{-1})$	14,046	± 1000
$\Delta_{\text{S}} (\text{cm}^{-1})$	14,671	± 1000

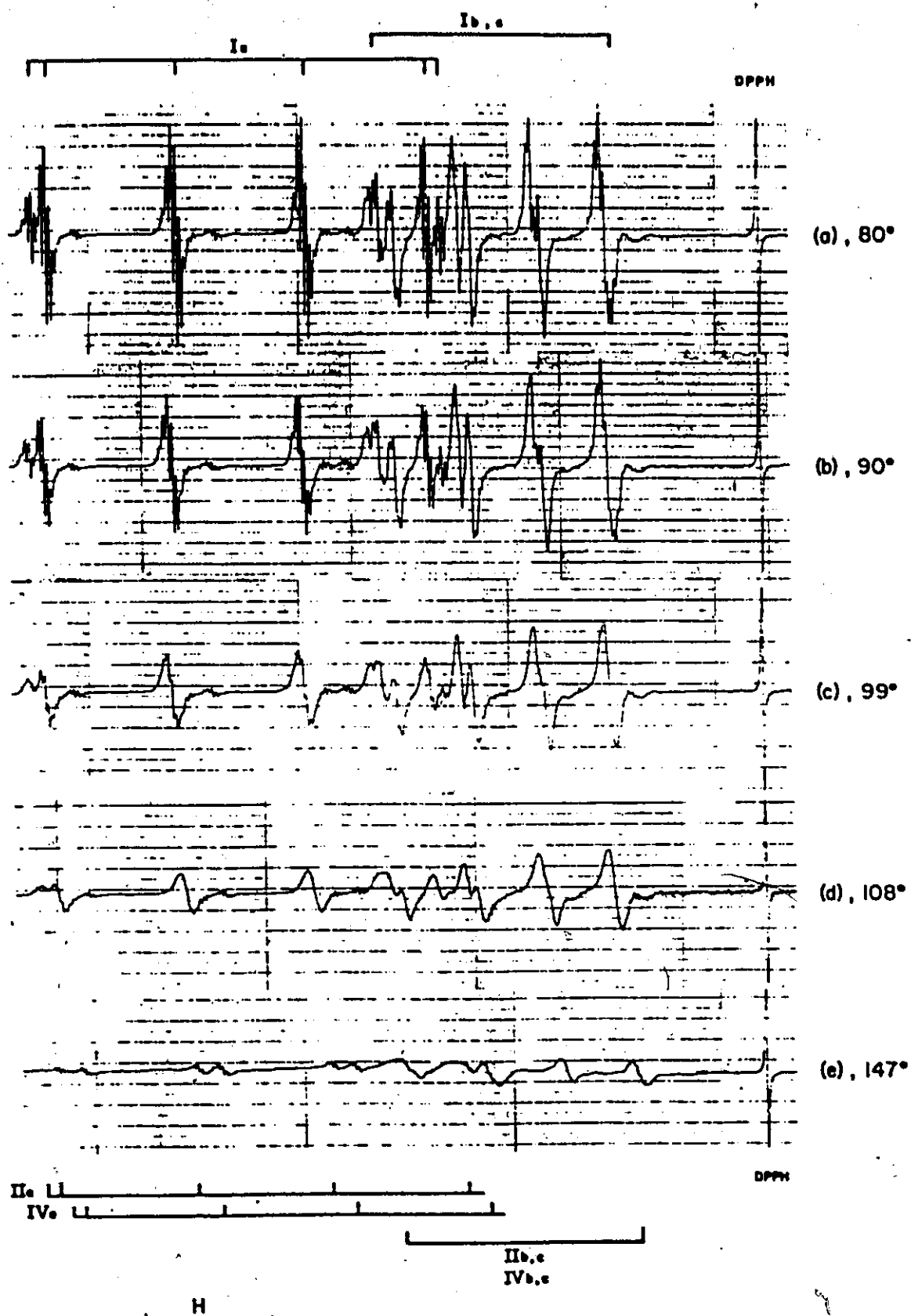


Fig.13 Superhyperfine structure of $\text{Ca(OH)}_2:\text{Cu}^{++}$ systems at various temperatures from 80°K to 147°K for $\vec{H} // [10\bar{1}0]$. Temperatures in $^{\circ}\text{K}$ are given beside each trace.

indicate that at 80°K , the line widths of the superhyperfine components are still decreasing with temperature. Attempts to obtain better resolution by working at 4.2°K have, however, proven unsuccessful. Saturation at such low temperatures, could be overcome only by 60db, or greater, attenuation of the incident microwave power. This resulted in poor sensitivity. Likewise, attempts to observe ENDOR transitions were also unsuccessful.

Further consideration of Fig.13 indicates that line widths increase rapidly with temperature. The superhyperfine components are unresolved at temperatures higher than 115°K .

In the case of the $\text{Ca}(\text{OD})_2:\text{Cu}^{++}$ system, no superhyperfine structure was observed.

2. High Temperature Spectrum

The sequence of events which occur as the temperature is varied over the range 80°K to 300°K is outlined in Fig.14 for $\text{Ca}(\text{OH})_2:\text{Cu}^{++}$, and in Fig.15 for $\text{Ca}(\text{OD})_2:\text{Cu}^{++}$. In both cases, the transition from I to III occurs at about 150°K , and spectrum III reaches a peak intensity near 210°K . The lines broaden and disappear below 300°K for $\text{Ca}(\text{OD})_2:\text{Cu}^{++}$, but are still observable at temperatures higher than 300°K for $\text{Ca}(\text{OH})_2:\text{Cu}^{++}$.

Spectrum III was analysed employing the spin Hamiltonian of Eq.(9). The results are listed in Table III. g_n^{AVE} and A_n^{AVE} were the only parameters obtained for $\text{Ca}(\text{OD})_2:\text{Cu}^{++}$ because the lines broadened and vanished as the orientation of \vec{H} was varied from the c axis.

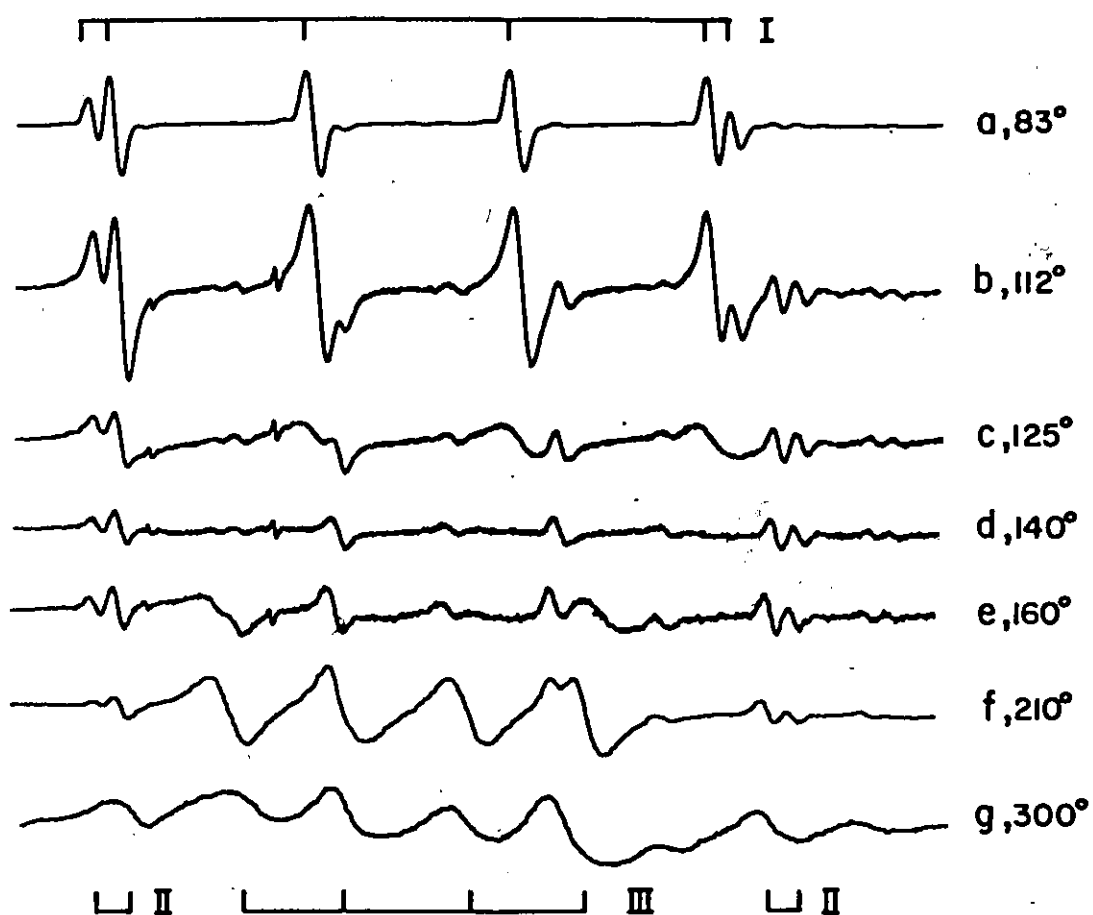


Fig. 14 Temperature dependence of $\text{Ca(OH)}_2:\text{Cu}^{++}$ spectra at K band for the case when $\vec{H} \parallel c$. Temperatures in °K are given beside each trace. \vec{H} increases from left to right.

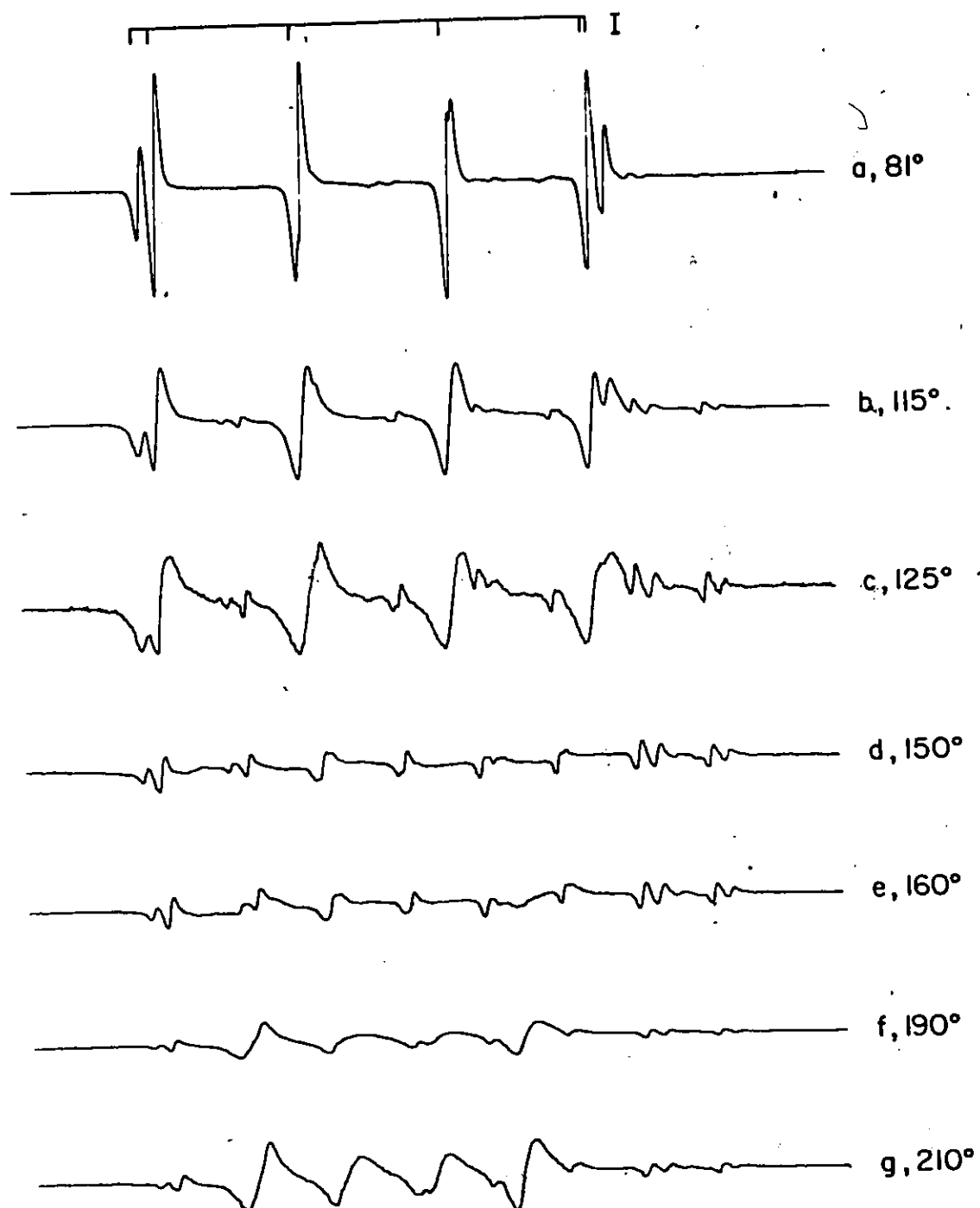


Fig. 15 Temperature dependence of $\text{Ca(OD)}_2:\text{Cu}^{++}$ spectra at K band for the case when $\vec{H} \parallel c$. Temperatures in °K are given beside each trace. \vec{H} increases from left to right.

TABLE III
Spin-Hamiltonian Parameters Of The Dynamic Jahn-Teller Effect Spectrum, III, In
 $\text{Ca(OH)}_2\text{:Cu}^{++}$ And $\text{Ca(OD)}_2\text{:Cu}^{++}$ Systems

HOST LATTICE	PARAMETER	VALUES CALCULATED FROM PARAMETERS OF SPECTRUM I				EXPERIMENTAL PARAMETERS				
		Eq. (35)		Eq. (36)		K BAND				X BAND
		63_{Cu}^{++}	65_{Cu}^{++}	63_{Cu}^{++}	65_{Cu}^{++}	182°K	217°K	280°K	300°K	300°K
Ca(OH)_2	g_{\parallel}	2.167	*	2.233	*	**	2.241 ± 0.001	**	2.242 ± 0.001	2.238 ± 0.001
	g_{\perp}	2.167	*	2.166	*	**	**	**	2.172 ± 0.001	2.170 ± 0.001
	$A_{\parallel}(\text{G})$	*	*	-52.9	*	**	-58.2 ± 2.0	**	-49.9 ± 2.0	-47.8 ± 2.0
	$A_{\perp}(\text{G})$	*	*	-43.4	*	**	**	**	-33.0 ± 2.0	-35.8 ± 2.0
Ca(OD)_2	g_{\parallel}	2.171	2.171	2.232	2.232	2.239 ± 0.001	2.239 ± 0.001	2.240 ± 0.001	**	**
	g_{\perp}	2.171	2.171	2.167	2.167	**	**	**	**	**
	$A_{\parallel}(\text{G})$	*	*	-50.2	-53.9	-58.7 ± 2.0	-56.5 ± 2.0	-52.6 ± 2.0	**	**
	$A_{\perp}(\text{G})$	*	*	-41.0	-43.8	**	**	**	**	**

* Value could not be calculated from experimental data available.

** Value was not measured.

3. The Transition Temperature

The relationship between spectra I and III was investigated further, through a detailed temperature dependence study of their respective intensities. Experimental measurements were made at X and K band frequencies for several magnetic field orientations. Graphs similar to those found in Fig.16 were obtained by plotting logarithms of first derivative peak to peak heights, $\text{Log } I_p$, versus inverse temperatures, T^{-1} .

C. NON-JAHN-TELLER CUPRIC IONS

1. Qualitative Discussion of Spectra I and II

As in the case of spectrum I, spectra II and IV are almost axial, and exhibit asymmetry in the $(1\bar{2}10)$ plane. A recording of the spectra for a general orientation in this plane can be found in Fig.17. The intensity ratio of spectra II : spectra IV is about 5:4 at 140°K . From Fig.18, it can be seen that this ratio increases to at least 5:1 at 4.2°K . A study of angular variations indicates that the symmetry axes of spectra II and IV are rotated about $(1\bar{2}10)$ direction with respect to the z axis of spectrum I, by approximately 1.5° and -0.8° respectively.

A partially resolved superhyperfine structure was observed only for the Ca(OH)_2 samples. As in the case of spectrum I, five components can definitely be counted at the same special orientations. The degree to which the superhyperfine transitions are resolved is virtually independent of temperature over the range 80°K to 160°K , as can be seen in Fig.13. Above 160°K , the components begin to broaden, and by 200°K , the superhyperfine structure is completely unresolved.

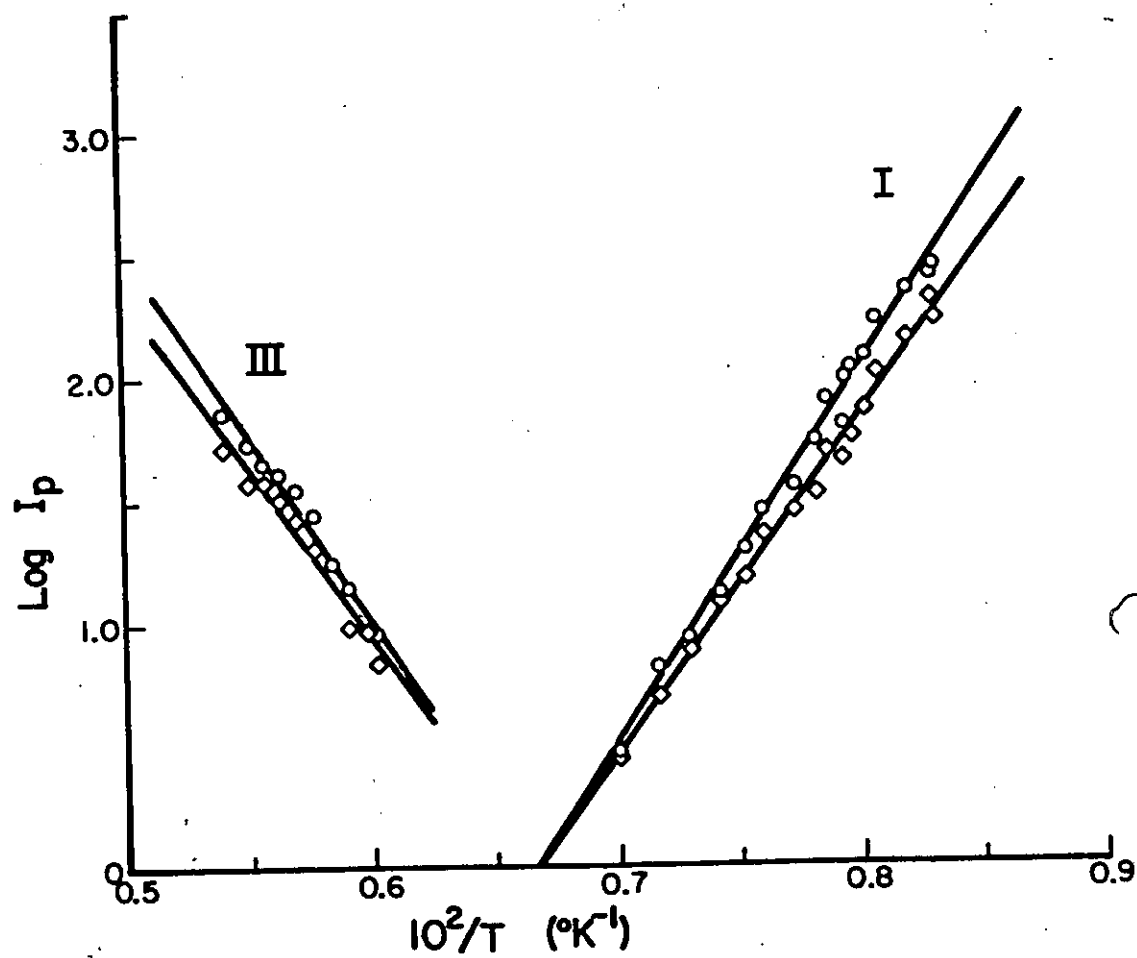


Fig.16 Plots of $\text{Log } I_p$ versus T^{-1} for spectra I and III.

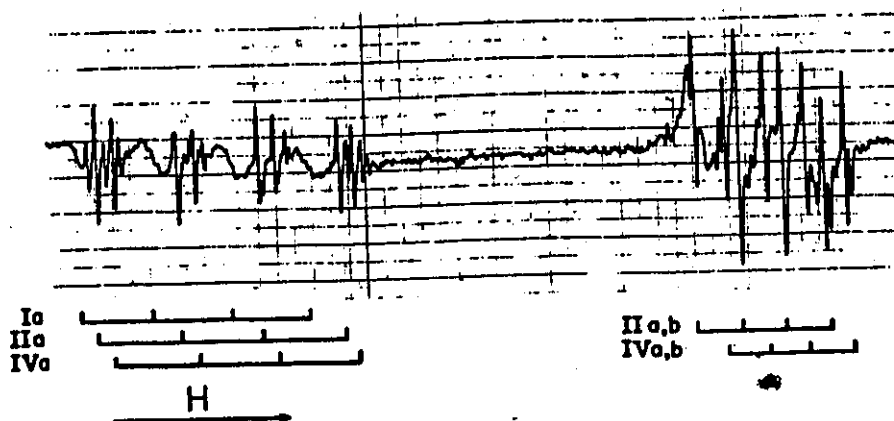


Fig.17 Recording of the non-Jahn-Teller spectra II and IV for a general orientation of \vec{H} in the $(1\bar{2}10)$ plane at 140°K . The low temperature Jahn-Teller spectrum I, and a third non-Jahn-Teller spectrum are also present.

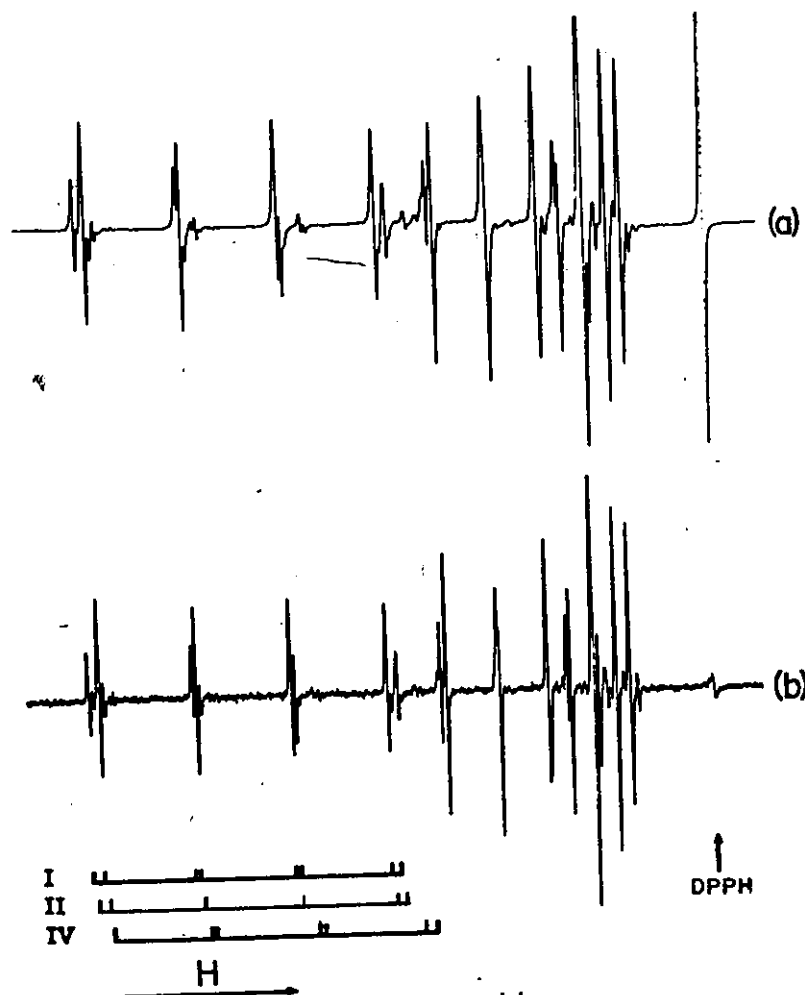


Fig.18 Recordings of the $\text{Ca}(\text{OD})_2:\text{Cu}^{++}$ spectrum for a general orientation of \vec{H} in the $(10\bar{1}0)$ plane. (a) is at 80°K and (b) is at 4.2°K . A comparison of (a) and (b) indicates a change in the relative populations of spectra II and IV.

Finally, from Fig. 17, there is evidence of the existence of even more sets of spectra similar to II and IV, but of lower intensity. These are shifted towards slightly higher magnetic fields.

2. Quantitative Results for Spectra II and IV

The spin Hamiltonian of Eq. (9) was used to analyse spectra II and IV. The data obtained from this analysis is summarized in Table IV. Lack of forbidden transition measurements prevented the accurate determination of quadrupole parameters.

D. APPLIED STRESS

Stress was applied to $\text{Ca}(\text{OH})_2:\text{Cu}^{++}$ samples along the $(10\bar{1}0)$ direction, which is perpendicular to two opposing flat sides of the hexagonal crystal. The lines of stress through the crystal assumed a hexagonal pattern, making the application of uniaxial stress impossible. The sample also cleaved very easily along planes parallel to this direction so that a quantitative study of applied stress was unfeasible. Nevertheless, a qualitative study of the effects of stress at 4.2°K is presented in Fig. 19. One set of Jahn-Teller spectra, Ia, is observed to diminish in intensity with respect to the other two sets, Ib and Ic.

Application of uniaxial stress along the c axis, although convenient experimentally, affected all three Jahn-Teller configurations equivalently. The E.P.R. lines of spectra I, II, and IV, suffered noticeable but relatively equal broadening, as illustrated by the recordings in Fig. 20. However, no change in the Jahn-Teller transition temperature was observed, and the samples appeared to suffer permanent strain in the course of this experiment.

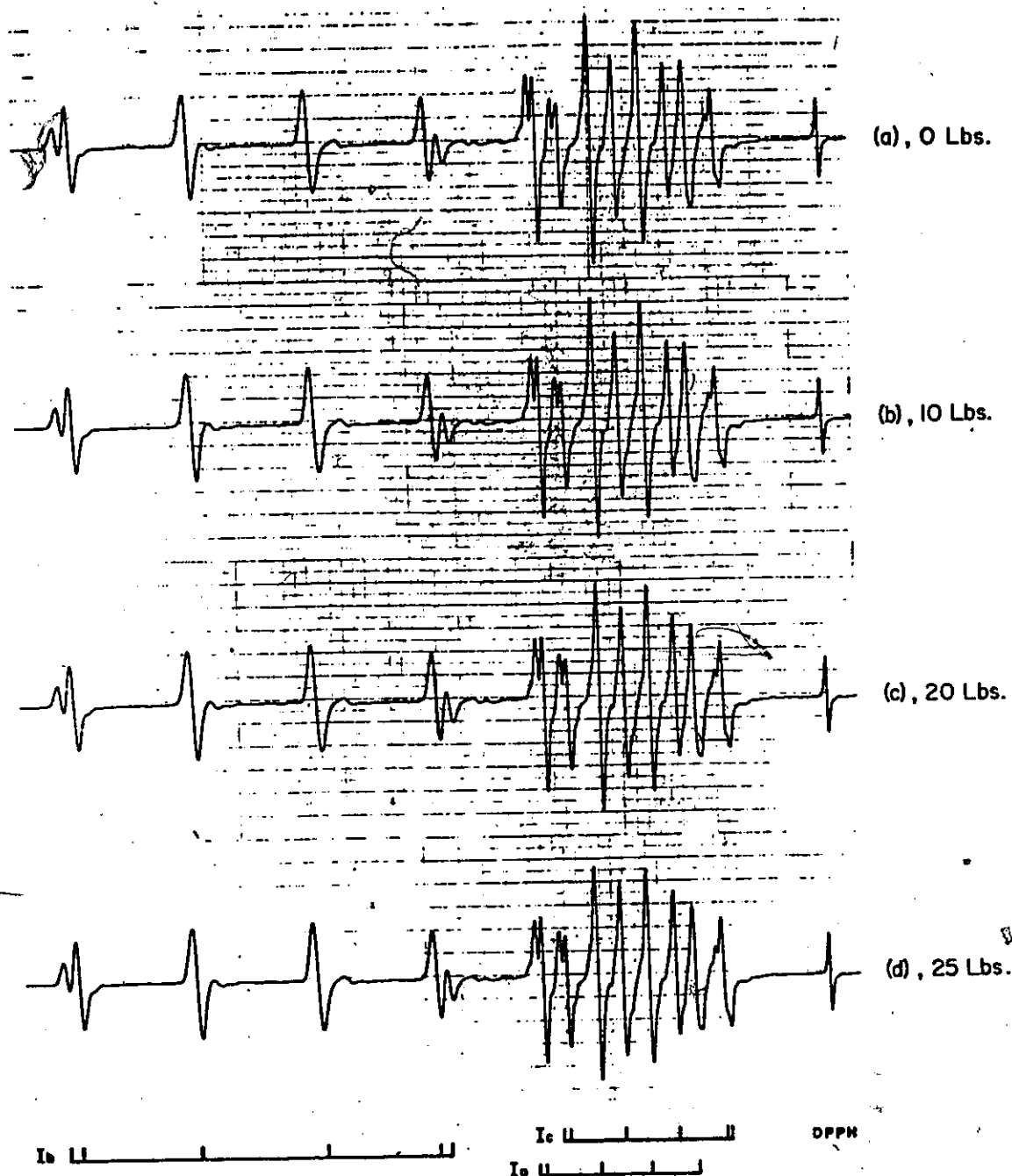


Fig. 19 Effect of uniaxial stress when applied to $\text{Ca}(\text{OH})_2:\text{Cu}^{++}$ along the $[10\bar{1}0]$ direction at 4.2°K . H is along a general direction in the $(10\bar{1}0)$ plane. Forces of the magnitudes listed beside each trace were applied to a sample with an average cross-section of 1.5×10^{-2} sq.in. (approximately).

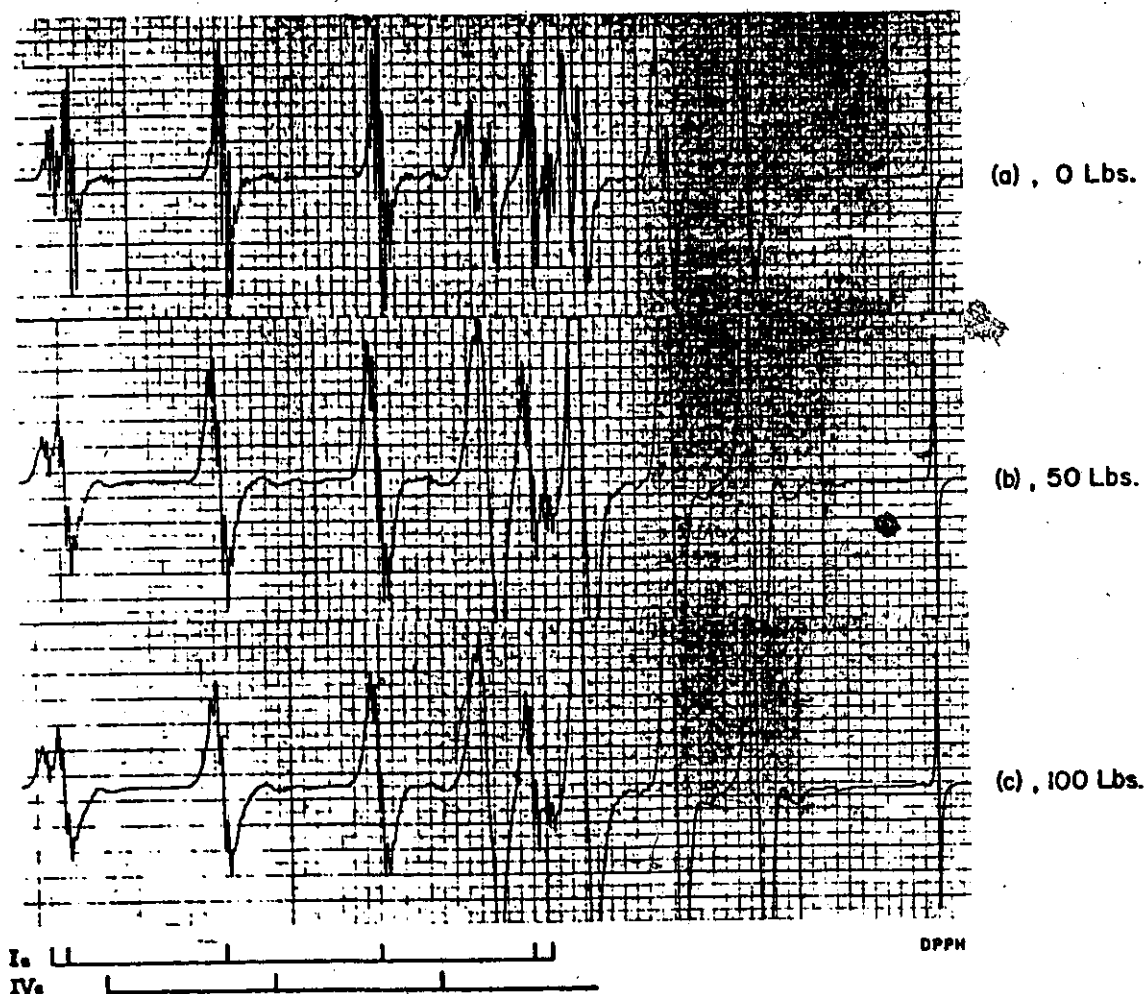


Fig.20 Effect of uniaxial stress when applied to $\text{Ca(OH)}_2:\text{Cu}^{++}$ along the $[0001]$ direction at 80°K for $\vec{H} \parallel [10\bar{1}0]$. Forces of the magnitudes listed beside each trace were applied to a sample with a cross-sectional area of 1.7×10^{-2} sq.in. (approx.).

TABLE IV

Spin-Hamiltonian Parameters Of Non-Jahn-Teller Coupled
 $\text{Ca}(\text{OH})_2:\text{Cu}^{++}$ And $\text{Ca}(\text{OD})_2:\text{Cu}^{++}$ Complexes

COMPLEX	$\text{Ca}(\text{OH})_2:\text{Cu}^{++}$		$\text{Ca}(\text{OD})_2:\text{Cu}^{++}$	
SPECTRUM	II	IV	II	IV
g_{zz}	2.397 ± 0.003	2.397 ± 0.003	2.396 ± 0.003	2.397 ± 0.003
g_{xx}	2.070 ± 0.005	2.070 ± 0.005	2.071 ± 0.003	2.071 ± 0.003
g_{yy}	2.064 ± 0.005	2.064 ± 0.005	2.076 ± 0.003	2.074 ± 0.003
$A_{zz}(\text{G})$	-141.0 ± 3.0	-141.0 ± 3.0	-142.0 ± 2.0	-142.0 ± 2.0
$A_{xx}(\text{G})$	$ A_{xx} < 6$	$ A_{xx} < 5$	14.0 ± 2.0	13.0 ± 2.0
$A_{yy}(\text{G})$	$ A_{yy} < 10$	$ A_{yy} < 10$	28.0 ± 2.0	24.5 ± 2.0
$A_{xz}(\text{G})$	10.0 ± 3.0	10.0 ± 3.0	10.0 ± 2.0	10.0 ± 2.0
α	$46^\circ \pm 1^\circ$	$48^\circ \pm 1^\circ$	$46^\circ \pm 1^\circ$	$48^\circ \pm 1^\circ$
β	$49^\circ \pm 2^\circ$	$52^\circ \pm 2^\circ$	$50^\circ \pm 2^\circ$	$52^\circ \pm 2^\circ$

E. RADIATION DAMAGE

The $\text{Ca}(\text{OH})_2:\text{Cu}^{++}$ and $\text{Ca}(\text{OD})_2:\text{Cu}^{++}$ samples were x-irradiated at 80°K and neutron irradiated at room temperature. No change was observed in the spectra of these crystals.

VI. DISCUSSION OF THE RESULTS

A. The Jahn-Teller Cupric Ion

1. Low Temperature Spectrum

At temperatures below 140°K , the observed E.P.R. spectrum, I, is a superposition of spectra associated with three distinct Cu^{++} complexes (a, b, and c). The individual spectra are identical in every respect, and are characteristic of an orbital singlet, spin doublet system. However, only one Ca^{++} site exists in the hexagonal $\text{Ca}(\text{OH})_2$ unit cell where Cu^{++} can enter the lattice as a substitutional impurity. As a result, I must be viewed as an experimental manifestation of a static Jahn-Teller effect in $\text{Ca}(\text{OH})_2$ -type lattices.

Furthermore, experimental data suggests that the Cu^{++} impurities form strong σ -bonds with four planar ligands. The xy plane of the \tilde{g} tensor coincides with a plane containing four hydroxyls while its z-axis forms an angle of 13° with the 3-Cu-6 bond, as illustrated in Fig.1. Also, a resolved, five-line superhyperfine structure is observed when a magnetic field is applied along the $[10\bar{1}0]$ direction where the four planar OH^- are equivalent. As a result of this type of planar bonding, some unique features of both "static" and dynamic Jahn-Teller effects are observed in $\text{Ca}(\text{OH})_2:\text{Cu}^{++}$ systems. For instance, the principal axes of the \tilde{g} and \tilde{A} tensors of spectra associated with the static case deviate noticeably from the cubic axes of the complex.

Moreover, for a specific spectrum, the principal axes of the \bar{g} tensor do not coincide with those of the \bar{A} tensor, a phenomenon predicted by perturbation theory as a result of substantial admixture of $|\theta\rangle$ into the ground level $|\epsilon\rangle$ by spin-orbit coupling. Finally, the \bar{g} and \bar{A} tensors of the spectrum associated with the dynamic case exhibit marked anisotropy. Each of these features has not been reported in the analysis of other cupric systems.

Prior to this investigation, cupric Jahn-Teller complexes have always been approximated as tetragonally distorted octahedrons. This approximation is generally valid as long as any trigonal component present in the system is small (i.e. $\alpha = 54.7^\circ \pm 2^\circ$). However, in highly trigonal complexes such as $\text{Ca}(\text{OH})_2:\text{Cu}^{++}$ (i.e. $\alpha = 47.5^\circ$), this is not the case. Moreover, an interpretation of the E.P.R. spectrum in terms of trigonal rather than cubic symmetry reveals some interesting consequences. First, the \bar{g} tensor axes are allowed to vary substantially from the cubic axes of the complex. Second, sizeable amounts of excited orbitals, including the nearby orbital $|\theta\rangle$ (i.e. $\sim 4,700 \text{ cm}^{-1}$), are admixed into the ground state. As a result, not only does the validity of a perturbation theory calculation of spin-Hamiltonian parameters become questionable, but also hopelessly complicated. Third, the failure of \bar{g} and \bar{A} tensor principal axes to coincide is actually predicted. It is obvious, therefore, that highly trigonal cupric complexes cannot be analysed using perturbation theory developed for tetragonally distorted octahedrons. This point has been overlooked or oversimplified by many authors.

Spectrum I was analysed by assuming a symmetry imposed on the Cu^{++} site by the static Jahn-Teller deformation. The results of this analysis are presented in

Table II. Estimates of the separation energy, Δ_θ , of the 2E_g ground doublet, and of the deformation magnitude, Q_θ , are included along with the parameters normally quoted for cupric systems such as Δ_o , Δ_c , Δ_s and κ .

From this data, it is possible to evaluate several parameters which describe the static Jahn-Teller effect occurring in $\text{Ca}(\text{OH})_2:\text{Cu}^{++}$. First, C_E is computed to have an experimental value of $13,100 \text{ cm}^{-1}/R$. This agrees reasonably well with point-charge-model calculations which give a value of $12,500 \text{ cm}^{-1}/R$, provided that the dipole moment of the OH^- ions is taken into account.⁶⁴ It should be noted that the coefficient C_E in this analysis is equivalent to van Vleck's coefficient V in tetragonal cases.⁶⁵⁻⁶⁶ Next, the splitting of the 2E_g orbital by Jahn-Teller coupling was found directly and is about $(4,710 \pm 1500) \text{ cm}^{-1}$. As a result, the Jahn-Teller stabilization energy is estimated to be $(1,180 \pm 400) \text{ cm}^{-1}$ for this system. Finally, the magnitude of the distortion from the original D_{3d} symmetry is given by $\rho_{\text{MIN}} = Q_\theta = (.18)R = 0.426 \text{ \AA}$. This suggests that in the distorted configuration, the 1-Cu-4 and 2-Cu-5 bonds in Fig.1 contract by about 0.184 \AA while the 3-Cu-6 bond expands by twice that value.

It is interesting to examine the similarities which exist for both the trigonal and tetragonal cases of Jahn-Teller effect. Both are described by "Mexican-hat" shaped potential sheets, are separated at equilibrium by $\Delta_\theta = 2C_E^2/K$, and have a stabilization energy equal to $C_E^2/2K$. Even the distortions responsible for Jahn-Teller coupling, are very much alike for both cases.

When the OH^- were replaced by OD^- ions, the spectral lines of Cu^{++} were found to be very narrow (i.e. $\sim 3\text{G}$). This provided an excellent opportunity to accurately measure the hyperfine structure and quadrupole interactions of

the two naturally abundant Cu isotopes. From Table I data, it is apparent that all parameters except those pertaining to the hyperfine interaction are identical within experimental error. The magnitude of the hyperfine interaction, however, is larger for $^{65}\text{Cu}^{++}$ by a factor of 1.070. This value agrees well with the factor 1.071 obtained by comparing the nuclear gyromagnetic ratios of these isotopes.

2. High Temperature Spectrum

The angular variations of spectra I and III in the $(1\bar{2}10)$ or xz plane are superimposed in Fig.21. A most significant observation emerges from this figure. The resonant fields of III are approximate averages of those observed for the three sets, a, b and c, of I at all orientations in this plane.

Two possible mechanisms that might account for the appearance of III at high temperatures have been discussed. The first of these suggests that III is associated with the E.P.R. of a thermally populated vibronic state. If this were so, an isotropic g-factor given by Eq.(34) is expected. If, on the other hand, a thermally activated reorientation of the complex is responsible for III, the spin Hamiltonian parameters should agree with those calculated from Eq.(35). The data in Table III appears to support the latter mechanism.

The experimental points fall on straight lines in Fig.16. This suggests the existence of exponential relationships $I_{PI} \propto \exp(\Delta_D/kT)$ and $I_{PIII} \propto \exp(-\Delta_A/kT)$, over the temperature ranges $120^\circ\text{--}140^\circ\text{K}$ and $160^\circ\text{--}190^\circ\text{K}$ respectively, similar to that found in Eq.(36). Average decay energies, $\Delta_D(\text{OH}) = (1400 \pm 300)\text{cm}^{-1}$ and $\Delta_D(\text{OD}) = (1100 \pm 200)\text{cm}^{-1}$ were obtained for the $\text{Ca}(\text{OH})_2:\text{Cu}^{++}$ and $\text{Ca}(\text{OD})_2:\text{Cu}^{++}$ systems, respectively.

The growth of III gave activation energies $\Delta_A(\text{OH}) = (1200 \pm 300) \text{ cm}^{-1}$ and $\Delta_A(\text{OD}) = (1200 \pm 200) \text{ cm}^{-1}$. These values, however, can be viewed only as representing order of magnitude determinations for the following reasons. First, the temperature ranges over which the growth and decay phenomena can be studied are limited. Second, it is estimated that temperature gradients in the sample may result in errors as large as $\pm 2^\circ \text{ K}$. Third, a degree of uncertainty is present in determinations of I_p because the observed spectrum is a partially resolved superposition of spectra from two Cu^{++} isotopes. Fourth, different growth and decay rates exist among the various hyperfine components. Finally, a more precise quantitative analysis of this phenomenon would require a temperature variation study of line peak heights, I_L . The values of decay and activation energies quoted above were obtained from an investigation of first derivative peak to peak heights, I_p . Since $I_L \propto (I_p) \cdot (\text{first derivative line width})$, and since the lines of I are broadened while those of III are narrowed by increasing temperature, plots of I_L versus T^{-1} would provide reduced values of Δ_A and Δ_D .

As discussed by Wilson, Holuj and Hedgecock⁶⁷ for $\text{Ca}(\text{OH})_2:\text{Cu}^{++}$, if Δ_A and Δ_D are assumed to represent the same energy, E_B , then the spectrum III can be explained in the following way. By means of thermal excitation to higher levels and relaxation back into one of the energetically equivalent ground state distortions, the system associated with spectrum I, is able to jump in a random fashion between the three configurations available to it at any orientation of \vec{H} . When the jumping frequency is high enough, spectrum III appears as an experimental manifestation of the "hindered" rotation being executed by the system about the c axis. E_B represents the energy barrier which must be overcome when the system passes from one configuration to another. In systems with strong Jahn-Teller coupling such as $\text{Ca}(\text{OH})_2:\text{Cu}^{++}$ and $\text{Ca}(\text{OD})_2:\text{Cu}^{++}$, it is likely that this energy

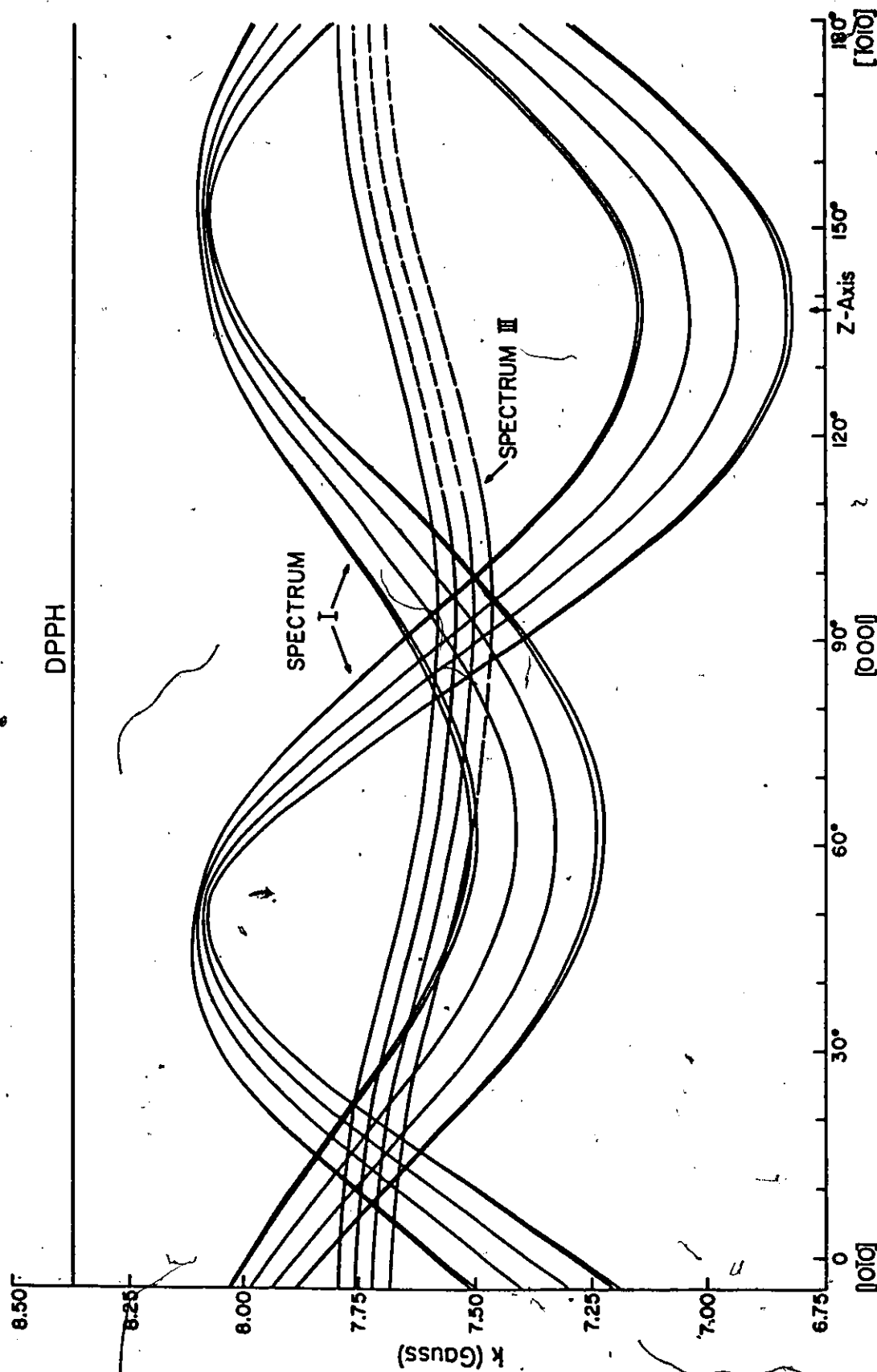


Fig.21 Angular variation of the Jahn-Teller spectra of $\text{Ca(OH)}_2:\text{Cu}^{++}$ in the (1210) plane. The curves for I and III were obtained at temperatures of 85° and 300°K, respectively.

barrier is the "warping term", $A_{30}^3 \cos 3\theta$, which was originally introduced by Opik and Pryce.⁶⁸ They estimated $|A_{30}^3|$ to be 700cm^{-1} for Cu^{++} complexes, indicating a value of about 1400cm^{-1} for the barrier height. The values of E_B obtained for the systems fall in the range $900\text{-}1700\text{cm}^{-1}$, and thus, are in a reasonable agreement with the Opik and Pryce value.

B. NON-JAHN-TELLER CUPRIC IONS

The Cu^{++} systems associated with spectra II and IV have not been identified. From the parameters listed in Table III, and from angular variation studies of these spectra, it appears that these systems are similar to the Jahn-Teller system associated with spectrum I, but are somehow stabilized in one of the three possible distortions of the cupric complex. Similar non-Jahn-Teller spectra were observed by Low and Suss⁶⁹ in $\text{CaO}:\text{Cu}^{++}$.

SUMMARY AND CONCLUSIONS

The E.P.R. spectra of $\text{Ca}(\text{OH})_2:\text{Cu}^{++}$ and $\text{Ca}(\text{OD})_2:\text{Cu}^{++}$ systems have been investigated thoroughly over the temperature range 4.2°K to 360°K . For $T < 140^\circ\text{K}$, the spectra suggest that Cu^{++} is subjected to a static Jahn-Teller deformation. A detailed analysis, aided by narrow line widths for $\text{Ca}(\text{OD})_2:\text{Cu}^{++}$ spectra, revealed two interesting points. First, it established that the \tilde{g} tensor symmetry axes, oriented approximately at 47.5° to the hexagonal c axis, are displaced considerably from the cubic axes of the complex (i.e. 54.7° to c axis). Significantly enough, they are directed perpendicular to planes containing four hydroxyls, a fact which is verified by the observation of a five line superhyperfine structure at certain orientations of the $\text{Ca}(\text{OH})_2:\text{Cu}^{++}$ system.. It should be noted that this peculiarity of these systems is responsible for some unique features of both the "static" and the "dynamic" Jahn-Teller effects. Second, it determined that the principal axis of the hyperfine-structure tensor differed noticeably ($\sim 4^\circ$) from those of the \tilde{g} tensor. In addition, the analysis yielded accurate quadrupole measurements for the $\text{Ca}(\text{OD})_2:\text{Cu}^{++}$ system. The experimental spin-Hamiltonian parameters of the low temperature spectra associated with these systems are listed in Table I.

Furthermore, by assuming the symmetry imposed on the Cu^{++} site by the static Jahn-Teller deformation, order of magnitude estimates have been obtained for several Jahn-Teller effect parameters in addition to the normally quoted Cu^{++} parameters such as δ , κ , Δ_s , Δ_o and Δ_c . These include the magnitudes of the coupling coefficient, C_E , the Jahn-Teller stabilization energy, E_{JT} , the splitting of the ground E_g orbital, and the actual deformation, Q_8 .

responsible for the static Jahn-Teller effect. In addition, analysis on this basis appears to account for unique features of these systems such as the orientation of \tilde{g} tensor symmetry axis, and the appearance of off-diagonal hyperfine structure terms.

Upon warming, the intensity of the low-temperature spectra, I, gradually decreases and virtually vanishes at 145°K, only to be replaced at a slightly higher temperature by a single spectrum, III, consisting of weak broad lines that grow in intensity with temperature. The decay of I and the growth of III appear to follow an Orbach type of relaxation process, and provide an order of magnitude estimate of the potential barrier height, or "warping term", separating the distorted configurations of the complex. Moreover, spectrum III is interpreted as originating from a rapid reorientation of the complex among its distortions. This interpretation is based on the fact that both the \tilde{g} and the \tilde{A} tensors of III are axial, having elements that are almost exact averages of the corresponding elements of spectrum I. As a result, spectrum III is unique in the literature on the Jahn-Teller effect, standing in contrast to all previously observed cases where isotropic spectra only were reported.

APPENDIX A

DEFINITION OF SYMBOLS USED IN MATHEMATICAL RELATIONSHIPS

- H , the Hamiltonian which describes the energy of the free cupric ion
- V_i , the Hamiltonian term which specifies the i^{th} inter-action
- p_k , the linear momentum of k^{th} electron of the cupric ion
- r_k , the co-ordinates which located the k^{th} electron relative to the cupric ion centre
- m , the mass of the electron
- e , the electrostatic charge of an electron
- Z , the atomic number of an atom
- r_{kj} , the magnitude of separation between the k^{th} and j^{th} electrons
- \vec{l}_k , the orbital angular momentum of k^{th} electron
- \vec{s}_k , the spin angular momentum of k^{th} electron
- \vec{L} , the total electronic orbital angular momentum of the ion
- \vec{S} , the total electronic spin angular momentum of the ion
- \vec{I} , the total nuclear spin angular momentum of the ion
- γ_n , the nuclear gyromagnetic ratio
- β , the Bohr magneton

β_n , the nuclear magneton

\vec{H} , the external applied magnetic field

Q , the electric quadrupole moment

$\nabla^2 V$, the gradient of electrostatic field at the ionic nucleus

e^- , the electrostatic charge associated with each OH^- ligand

\vec{R}_i , the position vector locating the equilibrium position of the i^{th} ligand relative to the centre of the cupric ion

\vec{r} , the position vector locating the paramagnetic hole of the cupric ion relative to the ionic centre

$Y_{lm}(\theta, \phi)$, spherical harmonic functions, specifically those defined to order $l = 4$ in Appendix B

γ , the angle between the Ca-OH bond and the trigonal axis of the $Ca(OH)_2$ complex

$$f_{20} = \sqrt{\frac{4\pi}{5}} (3\cos^2\gamma - 1)$$

$$f_{40} = \sqrt{\frac{4\pi}{9}} (35\cos^4\gamma - 30\cos^2\gamma + 3)$$

$$f_{43} = \sqrt{\frac{4\pi}{9}} (\sin^3\gamma \cos\gamma)$$

$Z_{lm}^i(\theta, \phi)$, real linear combinations of spherical harmonics defined for $l = 2, 4$ in Appendix C

$\langle r^k \rangle = \int R_{3d}^* R_{3d} r^{k+2} dr$, the expectation value of the electronic operator r^k

- R_{3d} , the radial component of a 3d orbital
 v , the angle whose sine and cosine define fractions of z_{2m}^i orbitals present in the eigenstates of the $3d^9$ hole located in a D_{3d}^5 symmetry crystal field
 α , the angle about the Y-axis defined in Fig. 1 by which the (x,y,z) co-ordinate system is rotated with respect to the (X,Y,Z) co-ordinate system.
 \tilde{g} , the g tensor
 \tilde{A} , the hyperfine interaction tensor
 \tilde{Q} , the quadrupole interaction tensor
 L_p , $p = x, y, z$, angular momentum operators defined in Appendix H
 λ , the spin-orbit constant for the free Cu^{++} ion
 g_0 , the free electron g-factor
 g_{pq} , $p, q = x, y, z$, the pq element of the \tilde{g} tensor
 δ_{pq} , $p, q = x, y, z$, the Dirac delta function
 Δ_i , $i = 0, o, c, s$, the energy of the i^{th} excited orbital above the ground orbital in the Cu^{++} system
 ζ_o, ζ_1 , spin-orbit covalency factors
 k_o, k_1 , orbital reduction factors
 κ , the hyperfine contact constant

$\langle r_q^{-3} \rangle$, the expectation value of the operator r_q^{-3} where r_q is the effective electronic radius as seen by the Cu nucleus in the electric quadrupole interaction

\vec{S}_i , the position vector locating the instantaneous position of the i^{th} ligand relative to the centre of the cupric ion

$\vec{\sigma}_i$, the displacement vector locating the instantaneous position of the i^{th} ligand relative to its equilibrium position

Q_i , distortions of the $\text{Ca}(\text{OH})_2$ lattice from its equilibrium configuration

q_i^j , normal co-ordinates of D_{3d} symmetry

W_{JT} , the matrix elements of the Jahn-Teller coupling interaction within the manifold of degenerate ground orbitals $|\epsilon\rangle$ and $|\theta\rangle$

C_E , the Jahn-Teller coupling constant

U_θ , a matrix identical to the Pauli matrix $-\vec{\sigma}_z$

U_E , a matrix identical to the Pauli matrix $\vec{\sigma}_x$

A_3 , the Opik and Pryce coupling constant

K , the elastic constant of the lattice in the absence of Jahn-Teller coupling

τ , the time required for configurational reorientation of the $\text{Ca}(\text{OH})_2$ complex from one J.T. distortion to another

$g_{\parallel}^{\text{AVE}}$, g_{\perp}^{AVE} , are parameters obtained by averaging the principal value of the \tilde{g} tensor measured for the three static distortions of the $\text{Ca}(\text{OH})_2\text{:Cu}^{++}$ complex

E_B , the energy barrier separating the distorted configurations

T , the temperature in $^{\circ}\text{K}$

APPENDIX B

NORMALIZED SPHERICAL HARMONICS $Y_{\ell m}(\theta, \phi)$

TO ORDER $\ell = 4$

General Definition:

$$Y_{\ell m}(\theta, \phi) = (-1)^t \left(\frac{2\ell + 1}{4\pi} \right)^{\frac{1}{2}} \left(\frac{(\ell - |m|)!}{(\ell + |m|)!} \right)^{\frac{1}{2}} P_{\ell}^m(\cos \theta) e^{im\phi}$$

where $t = m$ for $m \geq 0$

$t = 0$ for $m \leq 0$

$$P_{\ell}^m(\cos \theta) = (1 - \cos^2 \theta)^{\frac{1}{2}|m|} \left(\frac{d}{d \cos \theta} \right)^{|m|} P_{\ell}(\cos \theta)$$

$$P_{\ell}(\cos \theta) = \frac{1}{2^{\ell} \ell!} \left(\frac{d}{d \cos \theta} \right)^{\ell} (\cos^2 \theta - 1)^{\ell}$$

Expressions for the spherical harmonics up to the order $\ell = 4$ are summarized in Table B1 for both spherical and rectangular co-ordinate representations.

TABLE B1

Spherical Harmonics to Order $l = 4$ in Spherical
Co-ordinate and Rectangular Co-ordinate Representations

Spherical Harmonic	Spherical Co-ordinate Representation	Rectangular Co-ordinate Representation
$Y_{00}(\theta, \phi)$	$\left(\frac{1}{4\pi}\right)^{1/2}$	$\left(\frac{1}{4\pi}\right)^{1/2}$
$Y_{10}(\theta, \phi)$	$\left(\frac{3}{4\pi}\right)^{1/2} \cos \theta$	$\left(\frac{3}{4\pi}\right)^{1/2} \frac{z}{r}$
$Y_{1\pm 1}(\theta, \phi)$	$\mp \left(\frac{3}{8\pi}\right)^{1/2} \sin \theta e^{\pm i\phi}$	$\mp \left(\frac{3}{8\pi}\right)^{1/2} \frac{(x \pm iy)}{r}$
$Y_{20}(\theta, \phi)$	$\left(\frac{5}{16\pi}\right)^{1/2} (3 \cos^2 \theta - 1)$	$\left(\frac{5}{16\pi}\right)^{1/2} \frac{(3z^2 - r^2)}{r^2}$
$Y_{2\pm 1}(\theta, \phi)$	$\mp \left(\frac{15}{8\pi}\right)^{1/2} \sin \theta \cos \theta e^{\pm i\phi}$	$\mp \left(\frac{15}{8\pi}\right)^{1/2} \frac{z(x \pm iy)}{r^2}$
$Y_{2\pm 2}(\theta, \phi)$	$\left(\frac{15}{32\pi}\right)^{1/2} \sin^2 \theta e^{\pm i2\phi}$	$\left(\frac{15}{32\pi}\right)^{1/2} \frac{(x \pm iy)^2}{r^2}$
$Y_{30}(\theta, \phi)$	$\left(\frac{7}{16\pi}\right)^{1/2} (5 \cos^3 \theta - 3 \cos \theta)$	$\left(\frac{7}{16\pi}\right)^{1/2} \frac{z(5z^2 - 3r^2)}{r^3}$
$Y_{3\pm 1}(\theta, \phi)$	$\mp \left(\frac{21}{64\pi}\right)^{1/2} \sin \theta (5 \cos^2 \theta - 1) e^{\pm i\phi}$	$\mp \left(\frac{21}{64\pi}\right)^{1/2} \frac{(x \pm iy)(5z^2 - r^2)}{r^3}$
$Y_{3\pm 2}(\theta, \phi)$	$\left(\frac{105}{32\pi}\right)^{1/2} \sin^2 \theta \cos \theta e^{\pm i2\phi}$	$\left(\frac{105}{32\pi}\right)^{1/2} \frac{z(x \pm iy)^2}{r^3}$
$Y_{3\pm 3}(\theta, \phi)$	$\mp \left(\frac{35}{64\pi}\right)^{1/2} \sin^3 \theta e^{\pm i3\phi}$	$\mp \left(\frac{35}{64\pi}\right)^{1/2} \frac{(x \pm iy)^3}{r^3}$
$Y_{40}(\theta, \phi)$	$\left(\frac{9}{256\pi}\right)^{1/2} (35 \cos^4 \theta - 30 \cos^2 \theta + 3)$	$\left(\frac{9}{256\pi}\right)^{1/2} \frac{(35z^4 - 30z^2 r^2 + 3r^4)}{r^4}$
$Y_{4\pm 1}(\theta, \phi)$	$\mp \left(\frac{45}{64\pi}\right)^{1/2} \sin \theta (7 \cos^3 \theta - 3 \cos \theta) e^{\pm i\phi}$	$\mp \left(\frac{45}{64\pi}\right)^{1/2} \frac{(x \pm iy)(7z^3 - 3zr^2)}{r^4}$
$Y_{4\pm 2}(\theta, \phi)$	$\left(\frac{45}{128\pi}\right)^{1/2} \sin^2 \theta (7 \cos^2 \theta - 1) e^{\pm i2\phi}$	$\left(\frac{45}{128\pi}\right)^{1/2} \frac{(x \pm iy)^2 (7z^2 - r^2)}{r^4}$
$Y_{4\pm 3}(\theta, \phi)$	$\mp \left(\frac{315}{64\pi}\right)^{1/2} \sin^3 \theta \cos \theta e^{\pm i3\phi}$	$\mp \left(\frac{315}{64\pi}\right)^{1/2} \frac{z(x \pm iy)^3}{r^4}$
$Y_{4\pm 4}(\theta, \phi)$	$\left(\frac{315}{512\pi}\right)^{1/2} \sin^4 \theta e^{\pm i4\phi}$	$\left(\frac{315}{512\pi}\right)^{1/2} \frac{(x \pm iy)^4}{r^4}$

APPENDIX C

REAL ANGULAR FUNCTIONS $Z_{\ell m}(\theta, \phi)$, $\ell = 2$ and 4

General Definition:

$$Z_{\ell 0}(\theta, \phi) = Y_{\ell 0}(\theta, \phi)$$

$$Z_{\ell m}^C(\theta, \phi) = \frac{\sqrt{2}}{2} [Y_{\ell m}(\theta, \phi) + Y_{\ell -m}^*(\theta, \phi)]$$

$$Z_{\ell m}^S(\theta, \phi) = i \frac{\sqrt{2}}{2} [Y_{\ell -m}(\theta, \phi) - Y_{\ell -m}^*(\theta, \phi)]$$

Expressions for these real angular functions in both spherical harmonic and rectangular co-ordinate representations are summarized in Table C1 for angular momentum values $\ell = 2$ and 4 .

TABLE C1

Real Angular Functions, $Z_{lm}(\theta, \phi)$, $l = 2$ and 4

$Z_{lm}(\theta, \phi)$	Spherical Harmonic Representation	Rectangular Co-ordinate Representation
$Z_{20}(\theta, \phi)$	$Y_{20}(\theta, \phi)$	$(\frac{5}{16\pi})^{\frac{1}{2}} \frac{(3z^2 - r^2)}{r^2}$
$Z_{21}^2(\theta, \phi)$	$\frac{\sqrt{2}}{2} [Y_{2-1}(\theta, \phi) - Y_{21}(\theta, \phi)]$	$(\frac{15}{4\pi})^{\frac{1}{2}} \frac{(xz)}{r^2}$
$Z_{22}^C(\theta, \phi)$	$\frac{\sqrt{2}}{2} [Y_{2-2}(\theta, \phi) + Y_{22}(\theta, \phi)]$	$(\frac{15}{16\pi})^{\frac{1}{2}} \frac{(x^2 - y^2)}{r^2}$
$Z_{21}^S(\theta, \phi)$	$\frac{i\sqrt{2}}{2} [Y_{2-1}(\theta, \phi) + Y_{21}(\theta, \phi)]$	$(\frac{15}{4\pi})^{\frac{1}{2}} \frac{(yz)}{r^2}$
$Z_{22}^S(\theta, \phi)$	$\frac{i\sqrt{2}}{2} [Y_{2-2}(\theta, \phi) - Y_{22}(\theta, \phi)]$	$(\frac{15}{4\pi})^{\frac{1}{2}} \frac{(xy)}{r^2}$
$Z_{40}(\theta, \phi)$	$Y_{40}(\theta, \phi)$	$(\frac{9}{256\pi})^{\frac{1}{2}} \frac{(35z^4 - 30z^2r^2 + 3r^4)}{r^4}$
$Z_{41}^C(\theta, \phi)$	$\frac{\sqrt{2}}{2} [Y_{4-1}(\theta, \phi) - Y_{41}(\theta, \phi)]$	$(\frac{45}{32\pi})^{\frac{1}{2}} \frac{x(7z^3 - 3zr^2)}{r^4}$
$Z_{42}^C(\theta, \phi)$	$\frac{\sqrt{2}}{2} [Y_{4-2}(\theta, \phi) + Y_{42}(\theta, \phi)]$	$(\frac{45}{32\pi})^{\frac{1}{2}} \frac{(x^2 - y^2)(7z^2 - r^2)}{r^4}$
$Z_{43}^C(\theta, \phi)$	$\frac{\sqrt{2}}{2} [Y_{4-3}(\theta, \phi) - Y_{43}(\theta, \phi)]$	$(\frac{315}{32\pi})^{\frac{1}{2}} \frac{(3z)(x^2 - 3y^2)}{r^4}$
$Z_{44}^C(\theta, \phi)$	$\frac{\sqrt{2}}{2} [Y_{4-4}(\theta, \phi) + Y_{44}(\theta, \phi)]$	$(\frac{315}{256\pi})^{\frac{1}{2}} \frac{(x^4 + y^4 - 6x^2y^2)}{r^4}$
$Z_{41}^S(\theta, \phi)$	$\frac{i\sqrt{2}}{2} [Y_{4-1}(\theta, \phi) + Y_{41}(\theta, \phi)]$	$(\frac{45}{32\pi})^{\frac{1}{2}} \frac{y(7z^3 - 3zr^2)}{r^4}$
$Z_{42}^S(\theta, \phi)$	$\frac{i\sqrt{2}}{2} [Y_{4-2}(\theta, \phi) - Y_{42}(\theta, \phi)]$	$(\frac{45}{8\pi})^{\frac{1}{2}} \frac{(xy)(7z^2 - r^2)}{r^4}$
$Z_{43}^S(\theta, \phi)$	$\frac{i\sqrt{2}}{2} [Y_{4-3}(\theta, \phi) + Y_{43}(\theta, \phi)]$	$(\frac{315}{32\pi})^{\frac{1}{2}} \frac{(zy)(3x^2 - y^2)}{r^4}$
$Z_{44}^S(\theta, \phi)$	$\frac{i\sqrt{2}}{2} [Y_{4-4}(\theta, \phi) - Y_{44}(\theta, \phi)]$	$(\frac{315}{2\pi})^{\frac{1}{2}} \frac{(xy)(x^2 - y^2)}{r^4}$

APPENDIX

POINT CHARGE MODEL CRYSTAL FIELD EIGENVALUES

AND EIGENVECTORS

The crystal field interaction matrix expressed within the manifold spanned by the real linear combinations of $3d^9$ 2D orbitals z_{20} , z_{21}^C , z_{22}^C , z_{21}^S , and z_{22}^S is

	$ z_{20}\rangle$	$ z_{21}^C\rangle$	$ z_{22}^C\rangle$	$ z_{21}^S\rangle$	$ z_{22}^S\rangle$
$\langle z_{20} $	A	0	0	0	0
$\langle z_{21}^C $	0	B	C	0	0
$\langle z_{22}^C $	0	C	D	0	0
$\langle z_{21}^S $	0	0	0	B	-C
$\langle z_{22}^S $	0	0	0	-C	D

where $A = \frac{2}{7} A_{40} [\delta f_{20} + f_{40}]$

$B = \frac{1}{7} A_{40} [\delta f_{20} - 4/3 f_{40}]$

$C = 10/3 f_{43} A_{40}$

$D = -2/7 A_{40} [\delta f_{20} - 1/6 f_{40}]$

(D.1)

and $f_{20} = 3 \cos^2 \gamma - 1$

$f_{40} = 35 \cos^4 \gamma - 30 \cos^2 \gamma + 3$

$f_{43} = \sin \gamma \cos \gamma$

(D.2)

This matrix is easily diagonalized by considering each of the submatrices (A) , $\begin{pmatrix} B & C \\ C & D \end{pmatrix}$ and $\begin{pmatrix} B & -C \\ -C & D \end{pmatrix}$ individually: (A) is already diagonal, while both $\begin{pmatrix} B & C \\ C & D \end{pmatrix}$ and $\begin{pmatrix} B & -C \\ -C & D \end{pmatrix}$ give rise to the same secular equation, namely

$$\begin{aligned} (B - E)(D - E) - C^2 &= 0 \\ E^2 - (B + D)E + B.D - C^2 &= 0 \end{aligned} \quad (D.3)$$

The roots of this secular equation are the elements of the diagonalized submatrices, and are given by

$$\begin{aligned} E_{\pm} &= \frac{(B + D) \pm \sqrt{(B + D)^2 - 4(B.D - C^2)}}{2} \\ &= \frac{-A_{40}}{14} (\delta f_2 \ 0 + f_4 \ 0) \\ &\quad \pm \frac{A_{40}}{14} (3\delta f_2 \ 0 - 5/3 f_4 \ 0) \sqrt{1 + \left(\frac{140 f_4 \ 3}{9\delta f_2 \ 0 - 5f_4 \ 0} \right)^2} \end{aligned} \quad (D.4)$$

Hence, the eigenvalues of the crystal field interaction matrix are given by A , E_+ and E_- .

The eigenvectors describing states with eigenvalues A , E_+ and E_- are $|0\rangle$, $|\theta\rangle$, $|c\rangle$, $|\epsilon\rangle$, and $|s\rangle$ given by

$$\begin{pmatrix} |0\rangle \\ |\theta\rangle \\ |c\rangle \\ |\epsilon\rangle \\ |s\rangle \end{pmatrix} = S \cdot \begin{pmatrix} |z_2 \ 0\rangle \\ |z_2^C \ 1\rangle \\ |z_2^C \ 2\rangle \\ |z_2^S \ 1\rangle \\ |z_2^S \ 2\rangle \end{pmatrix} \quad (D.5)$$

where S is a unitary matrix such that

$$S \cdot \begin{pmatrix} A & 0 & 0 & 0 & 0 \\ 0 & B & C & 0 & 0 \\ 0 & C & D & 0 & 0 \\ 0 & 0 & 0 & B & -C \\ 0 & 0 & 0 & -C & 0 \end{pmatrix} \cdot S^{-1} = \begin{pmatrix} A & 0 & 0 & 0 & 0 \\ 0 & E_+ & 0 & 0 & 0 \\ 0 & 0 & E_- & 0 & 0 \\ 0 & 0 & 0 & E_+ & 0 \\ 0 & 0 & 0 & 0 & E_- \end{pmatrix} \quad (D.6)$$

In the case at hand, S has the form

$$S = \begin{pmatrix} 1 & 0 & 0 & 0 & 0 \\ 0 & \sin v & \cos v & 0 & 0 \\ 0 & -\cos v & \sin v & 0 & 0 \\ 0 & 0 & 0 & -\sin v & \cos v \\ 0 & 0 & 0 & \cos v & \sin v \end{pmatrix} \quad (D.7)$$

where the value of v is a function of δ . Substitution of Eq. (D.7) and Eq. (D.1) into Eq. (D.6) establishes the relationship between v and δ to be:

$$\tan v - \cot v = \frac{1}{70f_4^3} [9f_2^2 \delta - 5f_4^2 \delta]$$

Hence, the eigenvectors of the crystal field interaction defined in the (x, y, z) co-ordinate system of Fig. 1 are:

$$\begin{aligned} |\epsilon\rangle &= \cos v |z_2^S 2\rangle - \sin v |z_2^S 1\rangle \\ |\theta\rangle &= \cos v |z_2^C 2\rangle + \sin v |z_2^C 1\rangle \\ |0\rangle &= |z_2 0\rangle \\ |c\rangle &= \sin v |z_2^C 2\rangle - \cos v |z_2^C 1\rangle \\ |s\rangle &= \sin v |z_2^S 2\rangle + \cos v |z_2^S 1\rangle \end{aligned} \quad (D.8)$$

APPENDIX E

POINT CHARGE MODEL ESTIMATES OF $\text{Ca}(\text{OH})_2\text{:Cu}$ SYSTEM PARAMETERS

PARAMETER	VALUE	UNITS
e	4.8027×10^{-10}	E.S. cgs units of charge
μ_{OH}	1.66×10^{-18}	(E.S. cgs units of charge) (cm)
γ	61°	
R	2.367×10^{-8} 4.48	cm Au
$\langle r^2 \rangle$	1.044	Au
$\langle r^4 \rangle$	2.671	Au
A_{20}	-7660	cm^{-1}
A_{40}	-5040	cm^{-1}
f_{20} f_{40} f_{43}	-0.2949 -2.1178 0.3244	
f_{20} f_{40} f_{40}	-0.3485 -2.5025 0.3833	
δ	1.52	

APPENDIX F

TRANSFORMATIONS OF THE Z_{2i} BASIS FUNCTIONS FOR A COUNTER-CLOCKWISE ROTATION OF CO-ORDINATE AXES BY α ABOUT THE Y AXIS IN FIG. 1

Let the co-ordinates of a point be (X, Y, Z) in the original system, and (x, y, z) in a system rotated counter-clockwise by α about the Y axis. Then,

$$\begin{pmatrix} X \\ Y \\ Z \end{pmatrix} = \begin{pmatrix} \cos \alpha & 0 & \sin \alpha \\ 0 & 1 & 0 \\ -\sin \alpha & 0 & \cos \alpha \end{pmatrix} \cdot \begin{pmatrix} x \\ y \\ z \end{pmatrix}, \quad (F.1)$$

defines the relationship between co-ordinates in the two systems. By applying the relationships of Eq. (F.1) to the rectangular co-ordinate definitions of the Z_{2i} functions listed in Table C1, it is easily shown that the transformations

$$\begin{pmatrix} Z_{20}(X, Y, Z) \\ Z_{21}^C(X, Y, Z) \\ Z_{22}^C(X, Y, Z) \end{pmatrix} = \begin{pmatrix} \frac{3 \cos^2 \alpha - 1}{2} & -\sqrt{3} \sin \alpha \cos \alpha & \frac{\sqrt{3}}{2} \sin^2 \alpha \\ \sqrt{3} \sin \alpha \cos \alpha & 2 \cos^2 \alpha - 1 & -\sin \alpha \cos \alpha \\ \frac{\sqrt{3}}{2} \sin^2 \alpha & \sin \alpha \cos \alpha & \frac{1 + \cos^2 \alpha}{2} \end{pmatrix} \cdot \begin{pmatrix} Z_{20}(x, y, z) \\ Z_{21}^C(x, y, z) \\ Z_{22}^C(x, y, z) \end{pmatrix} \quad (F.2)$$

and

$$\begin{pmatrix} Z_{21}^S(X, Y, Z) \\ Z_{22}^S(X, Y, Z) \end{pmatrix} = \begin{pmatrix} \cos \alpha & -\sin \alpha \\ -\sin \alpha & \cos \alpha \end{pmatrix} \cdot \begin{pmatrix} Z_{21}^S(x, y, z) \\ Z_{22}^S(x, y, z) \end{pmatrix} \quad (F.3)$$

define these functions in the rotated (x, y, z) co-ordinate system.

APPENDIX G

NON-ZERO MATRIX ELEMENTS OF THE SPIN HAMILTONIAN OF EQ.(9)
BETWEEN THE STATES $|1/2, m_S, 3/2, m_I\rangle$

m_S		1/2				-1/2			
	m_I	3/2	1/2	-1/2	-3/2	3/2	1/2	-1/2	-3/2
1/2	3/2	D_1	D_2	D_3	0	D_4	D_5	0	0
	1/2	D_2^*	D_6	D_7	D_8	D_9	D_{10}	D_{11}	0
	-1/2	D_3^*	D_7^*	D_{12}	D_{13}	0	D_{14}	D_{15}	D_{16}
	-3/2	0	D_8^*	D_{13}^*	D_{17}	0	0	D_{18}	D_{19}
-1/2	3/2	D_4^*	D_9^*	0	0	D_{20}	D_{21}	D_{22}	0
	1/2	D_5^*	D_{10}^*	D_{14}^*	0	D_{21}^*	D_{23}	D_{24}	D_{25}
	-1/2	0	D_{11}^*	D_{15}^*	D_{18}^*	D_{22}^*	D_{24}^*	D_{26}	D_{27}
	-3/2	0	0	D_{16}^*	D_{19}^*	0	D_{25}^*	D_{27}^*	D_{28}

$$D_1 = 1/4(2(g_{zz} - 3\gamma)H_z + 3(A_{zz} + 3Q_{zz} + Q_{xx} + Q_{yy}))$$

$$D_2 = \sqrt{3}/4(A_{xz} + 4Q_{xz} - 2\gamma H_x - i(A_{yz} + 4Q_{yz} - 2\gamma H_y))$$

$$D_3 = \sqrt{3}/2(Q_{xx} - Q_{yy} - 2iQ_{xy})$$

$$D_4 = 1/4(2g_{xx}H_x + 3A_{xz} - i(2g_{yy}H_y + A_{yz}))$$

$$D_5 = \sqrt{3}/4(A_{xx} - A_{yy} - 2iA_{xy})$$

$$D_6 = 1/4(2(g_{zz} - \gamma)H_z + A_{zz} + Q_{zz} + 7(Q_{xx} + Q_{yy}))$$

$$D_7 = 1/2(A_{xz} - 2\gamma H_x - i(A_{yz} - \gamma H_y))$$

$$D_8 = \sqrt{3}/2(Q_{xx} - Q_{yy} - 2iQ_{xy})$$

$$D_9 = \sqrt{3}/4(A_{xx} + A_{yy})$$

$$D_{10} = 1/4(2g_{xx}H_x + A_{xz} - i(2g_{yy}H_y + A_{yz}))$$

$$D_{11} = 1/2(A_{xx} - A_{yy} - 2iA_{xy})$$

$$D_{12} = 1/4(2(g_{zz} + \gamma)H_z - A_{zz} + Q_{zz} + 7(Q_{xx} + Q_{yy}))$$

$$D_{13} = \sqrt{3}/4(A_{xz} - 4Q_{xz} - 2\gamma H_x - i(A_{yz} - 4Q_{yz} - 2\gamma H_y))$$

$$D_{14} = 1/2(A_{xx} + A_{yy})$$

$$D_{15} = 1/4(2g_{xx}H_x - A_{xz} - i(2g_{yy}H_y - A_{yz}))$$

$$D_{16} = \sqrt{3}/4(A_{xx} - A_{yy} - 2iA_{xy})$$

$$D_{17} = 1/4(2(g_{zz} + 3\gamma)H_z - 3A_{zz} + 9Q_{zz} + 3(Q_{xx} + Q_{yy}))$$

$$D_{18} = \sqrt{3}/4(A_{xx} + A_{yy})$$

$$D_{19} = 1/4(2g_{xx}H_x - 3A_{xz} - i(2g_{yy}H_y - 3A_{yz}))$$

$$D_{20} = 1/4(-2(g_{zz} + 3\gamma)H_z - 3A_{zz} + 9Q_{zz} + 3(Q_{xx} + Q_{yy}))$$

$$D_{21} = \sqrt{3}/4(-A_{xz} + 4Q_{xz} - 2\gamma H_x + i(A_{yz} - 4Q_{yz} + 2\gamma H_y))$$

$$D_{22} = \sqrt{3}/2(Q_{xx} - Q_{yy} - 2iQ_{xy})$$

$$D_{23} = 1/4(-2(g_{zz} + \gamma)H_z - A_{zz} + Q_{zz} + 7(Q_{xx} + Q_{yy}))$$

$$D_{24} = 1/2(-A_{xz} - 2\gamma H_x + i(A_{yz} + \gamma H_y))$$

$$D_{25} = \sqrt{3}/2(Q_{xx} - Q_{yy} - 2iQ_{xy})$$

$$D_{26} = 1/4(-2(g_{zz} - \gamma)H_z + A_{zz} + Q_{zz} + 7(Q_{xx} + Q_{yy}))$$

$$D_{27} = \sqrt{3}/4(-A_{xz} - 4Q_{xz} - 2\gamma H_x + i(A_{yz} + 4Q_{yz} + 2\gamma H_y))$$

$$D_{28} = 1/4(-2(g_{zz} - 3\gamma)H_z + 3A_{zz} + 9Q_{zz} + 3(Q_{xx} + Q_{yy}))$$

In the above relationships, the principal components of \bar{A} and \bar{Q} are expressed in units of gauss, $\gamma = \frac{\beta_n \gamma_{Cu}}{\beta} = \frac{\gamma_{Cu}}{3676.4}$ and D^* is the complex conjugate of D .

APPENDIX H

PROPERTIES OF ANGULAR MOMENTUM OPERATORS L_x , L_y , L_z , L_+ AND L_- WITHIN MANIFOLDS SPANNED BY SECOND ORDER SPHERICAL HARMONICS, BY REAL LINEAR COMBINATIONS OF 3_d ORBITALS DEFINED Z_{2i} , AND BY CRYSTAL FIELD EIGENSTATES OF Cu^{++} TRANSFORMING AS REPRESENTATIONS $1E_g$, A_{1g} AND $2E_g$ IN D_{3d} SYMMETRY

General Relationships:

$$L_+ = L_x + iL_y$$

$$L_- = L_x - iL_y$$

$$L_x = 1/2(L_+ + L_-)$$

$$L_y = -i/2(L_+ - L_-)$$

$$L_z |Y_{L, -M_L}\rangle = -M_L \hbar |Y_{L, -M_L}\rangle$$

$$L_z |Y_{L, -M_L}^*\rangle = M_L \hbar |Y_{L, -M_L}^*\rangle$$

$$L_{\pm} |Y_{L, -M_L}\rangle = \sqrt{(L \mp M_L + 1)(L \pm M_L)} \hbar |Y_{L, -M_L \pm 1}\rangle$$

$$L_{\pm} |Y_{L, -M_L}^*\rangle = -\sqrt{(L \pm M_L + 1)(L \mp M_L)} \hbar |Y_{L, -M_L \mp 1}^*\rangle$$

TABLE H1

Functions Generated By The Angular Momentum Operators L_+ , L_- , And L_z Operating On The Spherical Harmonic Functions $|Y_2, -M\rangle$ And $|Y_2^*, -M\rangle$, $M = 0, 1, 2$.

OPERATOR	FUNCTION	GENERATED FUNCTION [†]
L_+	$ Y_2, 0\rangle$	$-\sqrt{6} Y_2^*, -1\rangle$
	$ Y_2, -1\rangle$	$\sqrt{6} Y_2, 0\rangle$
	$ Y_2, -2\rangle$	$2 Y_2, -1\rangle$
	$ Y_2^*, -1\rangle$	$-2 Y_2^*, -2\rangle$
	$ Y_2^*, -2\rangle$	0
L_-	$ Y_2, 0\rangle$	$\sqrt{6} Y_2, -1\rangle$
	$ Y_2, -1\rangle$	$2 Y_2, -2\rangle$
	$ Y_2, -2\rangle$	0
	$ Y_2^*, -1\rangle$	$-\sqrt{6} Y_2, 0\rangle$
	$ Y_2^*, -2\rangle$	$-2 Y_2^*, -1\rangle$
L_z	$ Y_2, 0\rangle$	0
	$ Y_2, -1\rangle$	$- Y_2, -1\rangle$
	$ Y_2, -2\rangle$	$-2 Y_2, -2\rangle$
	$ Y_2^*, -1\rangle$	$ Y_2^*, -1\rangle$
	$ Y_2^*, -2\rangle$	$2 Y_2^*, -1\rangle$

† The listed generated functions are multiplied by the common factor \hbar .

TABLE H2

Functions Generated By The Angular Momentum Operators L_x , L_y And L_z Operating On The Real Linear Combinations Of $3d$ Orbitals, z_{2i}

OPERATOR	FUNCTION	GENERATED FUNCTION [†]
L_x	$ z_{20}\rangle$	$-i\sqrt{3} z_{21}^s\rangle$
	$ z_{21}^c\rangle$	$-i z_{22}^s\rangle$
	$ z_{22}^c\rangle$	$-i z_{21}^s\rangle$
	$ z_{21}^s\rangle$	$i\sqrt{3} z_{20}\rangle + i z_{22}^c\rangle$
	$ z_{22}^s\rangle$	$i z_{21}^c\rangle$
L_y	$ z_{20}\rangle$	$i\sqrt{3} z_{21}^c\rangle$
	$ z_{21}^c\rangle$	$-i\sqrt{3} z_{20}\rangle + i z_{22}^c\rangle$
	$ z_{22}^c\rangle$	$-i z_{21}^c\rangle$
	$ z_{21}^s\rangle$	$i z_{22}^s\rangle$
	$ z_{22}^s\rangle$	$-i z_{21}^s\rangle$
L_z	$ z_{20}\rangle$	0
	$ z_{21}^c\rangle$	$i z_{21}^s\rangle$
	$ z_{22}^c\rangle$	$2i z_{22}^s\rangle$
	$ z_{21}^s\rangle$	$-i z_{21}^c\rangle$
	$ z_{22}^s\rangle$	$-2i z_{22}^c\rangle$

† The listed generated functions are multiplied by the common factor \hbar .

TABLE H3

Matrix-Elements Of The Angular Momentum Operators L_x , L_y And L_z Within The Manifold Spanned By The Real Cu^{++} Orbital Eigenfunctions $|\epsilon\rangle$, $|\theta\rangle$, $|\phi\rangle$, $|c\rangle$ And $|s\rangle$ Defined In The (x,y,z) Co-ordinate System Of Fig.1 By Eq. (8)

L_x	$ \epsilon\rangle$	$ \theta\rangle$	$ \phi\rangle$	$ c\rangle$	$ s\rangle$
$\langle\epsilon $	0	$-is(3c^2-1)$	$i\sqrt{3}sc$	$-ic(3s^2-1)$	0
$\langle\theta $	$is(3c^2-1)$	0	0	0	$-ic(3c^2-4)$
$\langle\phi $	$-i\sqrt{3}sc$	0	0	0	$i\sqrt{3}c^2$
$\langle c $	$ic(3s^2-1)$	0	0	0	$-is(3c^2-2)$
$\langle s $	0	$ic(3c^2-4)$	$-i\sqrt{3}c^2$	$is(3c^2-2)$	0

L_y	$ \epsilon\rangle$	$ \theta\rangle$	$ \phi\rangle$	$ c\rangle$	$ s\rangle$
$\langle\epsilon $	0	0	0	0	i
$\langle\theta $	0	0	$i\sqrt{3}s$	-i	0
$\langle\phi $	0	$-i\sqrt{3}s$	0	$i\sqrt{3}c$	0
$\langle c $	0	i	0	0	0
$\langle s $	-i	0	0	0	0

L_z	$ \epsilon\rangle$	$ \theta\rangle$	$ \phi\rangle$	$ c\rangle$	$ s\rangle$
$\langle\epsilon $	0	$ic(3c^2-1)$	$i\sqrt{3}s^2$	$-is(3c^2+1)$	0
$\langle\theta $	$-ic(3c^2-1)$	0	0	0	$-is(3c^2-1)$
$\langle\phi $	$-i\sqrt{3}s^2$	0	0	0	$i\sqrt{3}sc$
$\langle c $	$is(3c^2+1)$	0	0	0	$-ic(3s^2-1)$
$\langle s $	0	$is(3c^2-1)$	$-i\sqrt{3}sc$	$ic(3s^2-1)$	0

Each matrix element listed in the above table is multiplied by the common factor \hbar . The symbols s and c represent $\sin \alpha$ and $\cos \alpha$ in Eq.(8).

TABLE H4

Matrix Elements Of The Spin Orbit Interaction, $V_{LS} = \lambda \vec{L} \cdot \vec{S}$,
 Within The Manifold Spanned By The Coupled Real Orbital-
 Spin Functions $|z_{2\alpha}, M_S, M_S = \frac{1}{2}, -\frac{1}{2}\rangle$

$ z_{2\alpha}\rangle$		$ z_{20}\rangle$		$ z_{21}^C\rangle$		$ z_{22}^C\rangle$		$ z_{21}^S\rangle$		$ z_{22}^S\rangle$	
	M_S	$ \frac{1}{2}\rangle$	$ \frac{-1}{2}\rangle$	$ \frac{1}{2}\rangle$	$ \frac{-1}{2}\rangle$	$ \frac{1}{2}\rangle$	$ \frac{-1}{2}\rangle$	$ \frac{1}{2}\rangle$	$ \frac{-1}{2}\rangle$	$ \frac{1}{2}\rangle$	$ \frac{-1}{2}\rangle$
$\langle z_{20} $	$\langle \frac{1}{2} $	0	0	0	$-\frac{\sqrt{3}}{2}\lambda$	0	0	0	$i\frac{\sqrt{3}}{2}\lambda$	0	0
	$\langle \frac{-1}{2} $	0	0	$\frac{\sqrt{3}}{2}\lambda$	0	0	0	$i\frac{\sqrt{3}}{2}\lambda$	0	0	0
$\langle z_{21}^C $	$\langle \frac{1}{2} $	0	$\frac{\sqrt{3}}{2}\lambda$	0	0	0	$-\frac{\lambda}{2}$	$-\frac{i\lambda}{2}$	0	0	$\frac{i\lambda}{2}$
	$\langle \frac{-1}{2} $	$-\frac{\sqrt{3}}{2}\lambda$	0	0	0	$\frac{\lambda}{2}$	0	0	$\frac{i\lambda}{2}$	$\frac{i\lambda}{2}$	0
$\langle z_{22}^C $	$\langle \frac{1}{2} $	0	0	0	$\frac{\lambda}{2}$	0	0	0	$\frac{i\lambda}{2}$	$-i\lambda$	0
	$\langle \frac{-1}{2} $	0	0	$-\frac{\lambda}{2}$	0	0	0	$\frac{i\lambda}{2}$	0	0	$i\lambda$
$\langle z_{21}^S $	$\langle \frac{1}{2} $	0	$-i\frac{\sqrt{3}}{2}\lambda$	$\frac{i\lambda}{2}$	0	0	$-\frac{i\lambda}{2}$	0	0	0	$-\frac{\lambda}{2}$
	$\langle \frac{-1}{2} $	$-i\frac{\sqrt{3}}{2}\lambda$	0	0	$-\frac{i\lambda}{2}$	$-\frac{i\lambda}{2}$	0	0	0	$\frac{\lambda}{2}$	0
$\langle z_{22}^S $	$\langle \frac{1}{2} $	0	0	0	$-\frac{i\lambda}{2}$	$i\lambda$	0	0	$\frac{\lambda}{2}$	0	0
	$\langle \frac{-1}{2} $	0	0	$-\frac{i\lambda}{2}$	0	0	$-i\lambda$	$-\frac{\lambda}{2}$	0	0	0

Each matrix element is multiplied by the common factor \hbar^2

APPENDIX I

NON-ZERO ELEMENTS OF THE SECOND ORDER PERTURBATION

TENSOR Λ_{pq}

1. Elements of Λ_{pq} for a general angle α

$$\Lambda_{xx} = \left\{ \frac{\sin^2 \alpha (3\cos^2 \alpha - 1)^2}{\Delta_\theta} + \frac{3\sin^2 \alpha \cos^2 \alpha}{\Delta_o} + \frac{\cos^2 \alpha (3\sin^2 \alpha - 1)^2}{\Delta_c} \right\} k_\perp$$

$$\Lambda_{yy} = \frac{1}{\Delta_s} k_\perp$$

$$\Lambda_{zz} = \left\{ \frac{\cos^2 \alpha (3\cos^2 \alpha - 1)^2}{\Delta_\theta} + \frac{3\sin^4 \alpha}{\Delta_o} + \frac{\sin^2 \alpha (3\cos^2 \alpha - 1)^2}{\Delta_c} \right\} k_\parallel$$

$$\Lambda_{xz} = \Lambda_{zx} = \left\{ \frac{-\sin \alpha \cos \alpha (3\cos^2 \alpha - 1)^2}{\Delta_\theta} + \frac{3\sin^3 \alpha \cos \alpha}{\Delta_o} + \frac{\sin \alpha \cos \alpha (3\sin^2 \alpha - 1)(3\cos^2 \alpha + 1)}{\Delta_c} \right\} (k_\parallel + k_\perp)/2$$

2. Elements of Λ_{pq} for $\alpha = 47.5^\circ$

$$\Lambda_{xx} = \left\{ \frac{0.074}{\Delta_\theta} + \frac{0.744}{\Delta_o} + \frac{0.182}{\Delta_c} \right\} k_\perp$$

$$\Lambda_{yy} = \frac{1}{\Delta_s} k_\perp$$

$$\Lambda_{zz} = \left\{ \frac{0.062}{\Delta_\theta} + \frac{0.886}{\Delta_o} + \frac{3.052}{\Delta_c} \right\} k_\parallel$$

$$\Lambda_{xz} = \Lambda_{zx} = \left\{ \frac{-0.068}{\Delta_\theta} + \frac{0.812}{\Delta_o} + \frac{0.744}{\Delta_c} \right\} (k_\parallel + k_\perp)/2$$

APPENDIX J

ELEMENTS OF THE SECOND ORDER

PERTURBATION TENSOR l_{pq}

$$l_{xx} = -1$$

$$l_{yy} = -1$$

$$l_{zz} = 2$$

$$l_{pq} = 0 \quad \text{when } p \neq q$$

APPENDIX K

NON-ZERO ELEMENTS OF THE SECOND ORDER PERTURBATION TENSOR Λ_{pq}

1. Elements of Λ_{pq} for a general angle α

$$\Lambda_{xx} = \frac{(3c^2-1)}{2} \left\{ \frac{(3cs)^2}{\Delta_\theta} + \frac{3s^2(3c^2+1)}{\Delta_c} + \frac{3s^2}{\Delta_o} \right\} k_{\parallel} + \frac{3k_{\perp}}{2\Delta_s}$$

$$\Lambda_{yy} = -\frac{1}{2} \left\{ \frac{(3c^2-1)(3cs)^2}{\Delta_\theta} + \frac{3s^2(9c^4-1)}{\Delta_c} + \frac{3s^2(3c^2-1)}{\Delta_o} \right\} k_{\parallel} \\ + \frac{1}{2} \left\{ \frac{3s^2(3c^2-1)^2}{\Delta_\theta} + \frac{3c^2(3s^2-1)}{\Delta_c} + \frac{(3sc)^2}{\Delta_o} \right\} k_{\perp}$$

$$\Lambda_{zz} = -\frac{1}{2} \left\{ \frac{3s^2(3c-1)^2}{\Delta_\theta} + \frac{3c^2(3s^2-1)}{\Delta_c} + \frac{(3sc)^2}{\Delta_o} + \frac{3}{\Delta_s} \right\} k_{\perp}$$

$$\Lambda_{xz} = -\frac{3sc}{2} \left\{ \frac{(3c^2-1)^2}{\Delta_\theta} + \frac{(3c^2+1)(3s^2-1)}{\Delta_c} + \frac{3s^2}{\Delta_o} \right\} k_{\parallel}$$

$$\Lambda_{zx} = \frac{sc}{2} (3c^2-1) \left\{ \frac{9s^2}{\Delta_\theta} + \frac{3(3s^2-1)}{\Delta_c} - \frac{3}{\Delta_o} \right\} k_{\perp}$$

In the above relationships, $c = \cos \alpha$ and $s = \sin \alpha$ while k_{\parallel} and k_{\perp} are the appropriate orbital reduction factors.

2. Elements of Λ_{pq} for $\alpha = 47.5^\circ$

$$\Lambda_{xx} = \left\{ \frac{0.412}{\Delta_\theta} + \frac{0.719}{\Delta_c} + \frac{0.301}{\Delta_o} \right\} k_{\parallel} + \frac{1.5k_{\perp}}{\Delta_s}$$

$$\Lambda_{YY} = - \left\{ \frac{0.412}{\Delta_{\theta}} + \frac{0.719}{\Delta_C} + \frac{0.301}{\Delta_O} \right\} k_{\parallel} + \left\{ \frac{0.111}{\Delta_{\theta}} + \frac{0.432}{\Delta_C} + \frac{1.116}{\Delta_O} \right\} k_{\perp}$$

$$\Lambda_{ZZ} = - \left\{ \frac{0.111}{\Delta_{\theta}} + \frac{0.432}{\Delta_C} + \frac{1.116}{\Delta_O} + \frac{1.5}{\Delta_S} \right\} k_{\perp}$$

$$\Lambda_{XZ} = - \left\{ \frac{0.102}{\Delta_{\theta}} - \frac{1.116}{\Delta_C} - \frac{1.218}{\Delta_O} \right\} k_{\parallel}$$

$$\Lambda_{ZX} = \left\{ \frac{0.500}{\Delta_{\theta}} + \frac{0.174}{\Delta_C} - \frac{0.277}{\Delta_O} \right\} k_{\perp}$$

APPENDIX L
NORMAL CO-ORDINATES OF AN XY_6 COMPLEX
OF D_{3d} SYMMETRY

TABLE L1

Normal Co-ordinate	Symmetry	
q_{A1}	A_{1g}	$[X_1 + X_2 - 2X_3 - \sqrt{3}(Y_1 - Y_2)]/\sqrt{24}$
q_{A2}	A_{1g}	$(Z_1 + Z_2 + Z_3)/\sqrt{6}$
q_1^c	E_g, θ	$[X_1 + X_2 + 4X_3 - \sqrt{3}(Y_1 - Y_2)]/\sqrt{48}$
q_1^s	E_g, ϵ	$\frac{1}{2}[X_1 - X_2 - \sqrt{3}(Y_1 + Y_2)]$
q_2^c	E_g, θ	$(Z_1 + Z_2 - 2Z_3)/\sqrt{12}$
q_2^s	E_g, ϵ	$\frac{1}{2}(Z_1 - Z_2)$
q_3^c	E_g, θ	$[X_1 + X_2 - 2X_3 + \sqrt{3}(Y_1 - Y_2)]/\sqrt{24}$
q_3^s	E_g, ϵ	$[-\sqrt{3}(X_2 - X_1) + Y_1 + Y_2 - 2Y_3]/\sqrt{24}$
q_4^c	E_g, θ	$(X_1 + X_2 + X_3)/\sqrt{6}$
q_4^s	E_g, ϵ	$(Y_1 + Y_2 + Y_3)/\sqrt{6}$

In the above table, $(X_i, Y_i, Z_i) = (\vec{\sigma}_i - \vec{\sigma}_{i+3})$

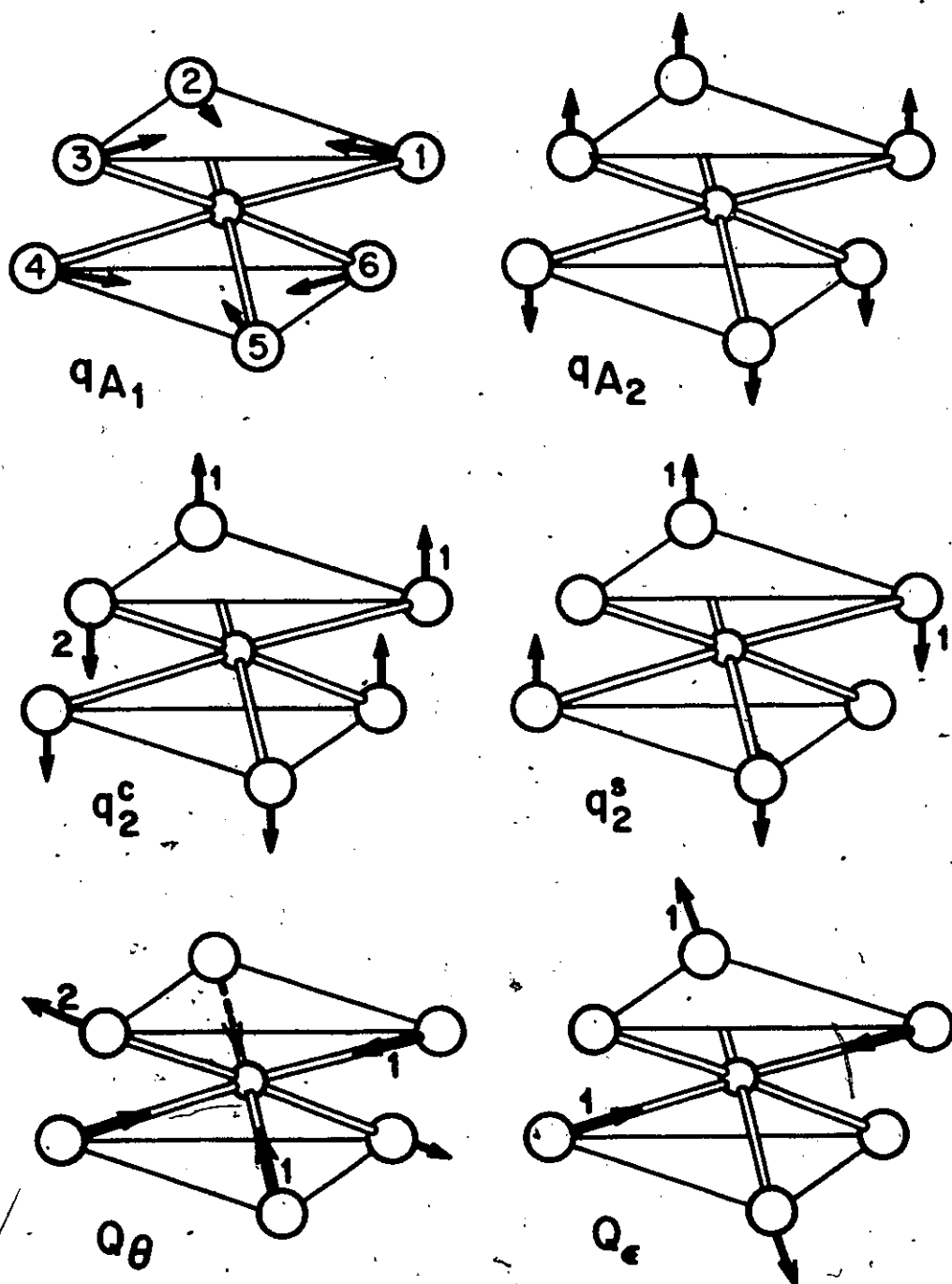


Fig. L1. Some of the normal modes of XY_6 complex with D_{3d} symmetry. Q_θ and Q_ϵ are defined in Eq. (25), the remaining ones in Table L1.

APPENDIX M

NON-ZERO MATRIX ELEMENTS OF THE COMPLETE
ELECTRONIC HAMILTONIAN, H_{ORB} , WITHIN THE MANIFOLD SPANNED
BY THE STATES $|z_{2i}, \pm 1/2\rangle$

$\langle z_{2i} $	$ z_{2i}\rangle$	$ z_{20}\rangle$		$ z_{21}^c\rangle$		$ z_{22}^c\rangle$		$ z_{21}^s\rangle$		$ z_{22}^s\rangle$	
	M_s	1/2	-1/2	1/2	-1/2	1/2	-1/2	1/2	-1/2	1/2	-1/2
$\langle z_{20} $	1/2	H_1	0	H_2	$-H_3$	H_4	0	0	H_7	0	0
	-1/2	0	H_1	H_3	H_2	0	H_4	H_7	0	0	0
$\langle z_{21}^c $	1/2	H_2	H_3	H_5	0	H_6	$-H_8$	$-H_9^x$	0	0	H_9
	-1/2	$-H_3$	H_2	0	H_5	H_8	H_6	0	H_9^x	H_9	0
$\langle z_{22}^c $	1/2	H_4	0	H_6	H_8	H_{10}	0	0	H_9	$-H_{12}$	0
	-1/2	0	H_4	$-H_8$	H_6	0	H_{10}	H_9	0	0	H_{12}
$\langle z_{21}^s $	1/2	0	$-H_7$	H_9^x	0	0	$-H_9$	H_{11}	0	H_{13}	$-H_8$
	-1/2	$-H_7$	0	0	$-H_9^x$	$-H_9$	0	0	H_{11}	H_8	H_{13}
$\langle z_{22}^s $	1/2	0	0	0	$-H_9$	H_{12}	0	H_{13}	H_8	H_{10}	0
	-1/2	0	0	$-H_9$	0	0	$-H_{12}$	$-H_8$	H_{13}	0	H_{10}

$$H_1 = \frac{2}{7} A_{40} (\delta f_{20} + f_{40})$$

$$H_2 = \frac{5}{7} A_{40} \delta f_{43} \frac{Q_8}{R}$$

$$H_3 = \frac{\sqrt{3}\lambda_1}{2}$$

$$H_4 = -\frac{5}{7} A_{40} \delta \frac{Q_0}{R} \sin^2 \gamma$$

$$H_5 = \frac{A_{40}}{21} (3\delta f_{20} - 4f_{40} + \frac{15\sqrt{3}}{2} \delta \frac{Q_0}{R} \sin^2 \gamma)$$

$$H_6 = \frac{10}{3} A_{40} f_{43} (\frac{3\sqrt{3}}{14} \delta \frac{Q_0}{R} + 1)$$

$$H_7 = \frac{i\sqrt{3}\lambda_1}{2}$$

$$H_8 = \frac{1}{2}\lambda_1$$

$$H_9 = \frac{i\lambda_1}{2} ; H_9^* = \frac{i\lambda_1}{2}$$

$$H_{10} = -\frac{A_{40}}{21} (6 \delta f_{20} - f_{40})$$

$$H_{11} = \frac{A_{40}}{21} (3\delta f_{20} - 4f_{40} - \frac{15\sqrt{3}}{2} \delta \frac{Q_0}{R} \sin^2 \gamma)$$

$$H_{12} = i\lambda_1$$

$$H_{13} = \frac{10}{3} A_{40} f_{43} (\frac{3\sqrt{3}}{14} \delta \frac{Q_0}{R} - 1)$$

The parameters δ , A_{40} , f_{20} , f_{40} and f_{43} have been defined in Appendix D, while $\lambda_n = \zeta_n k_n$ and $\lambda_1 = \zeta_1 k_1$ are spin-orbit coupling parameters which have been corrected for covalency effects.

APPENDIX N

SPIN-HAMILTONIAN PARAMETERS OF AN AVERAGED SPECTRUM I

Spectrum I consists of three component spectra, a, b, and c, which are described by tensors \tilde{g} , \tilde{A} , and \tilde{Q} . These tensors have equal principal values for all three components of spectrum I, but are expressed in three different co-ordinate systems with axes (x_n, y_n, z_n) respectively, where $n=a, b$, or c . Parameters of an averaged spectrum of I, are obtained by first rotating the respective co-ordinate systems of a, b, and c, to some common co-ordinate system with axes (x_A, y_A, z_A) . Then, the tensor elements of a, b, and c, are re-expressed in this new co-ordinate system and are averaged.

The z_n axis is directed at an angle α to the c axis for all three systems of I. For this reason, z_A is chosen to be parallel to this [0001] direction. For convenience, y_A is chosen to coincide with y_a along the $[1\bar{2}10]$ direction in the (0001) plane. Then, the transformation of co-ordinate system (x_A, y_A, z_A) is given by the relationship:

$$\begin{pmatrix} x_A \\ y_A \\ z_A \end{pmatrix} = \begin{pmatrix} \cos \alpha & 0 & \sin \alpha \\ 0 & 1 & 0 \\ -\sin \alpha & 0 & \cos \alpha \end{pmatrix} \cdot \begin{pmatrix} x_a \\ y_a \\ z_a \end{pmatrix}$$

for system a,

$$\begin{pmatrix} x_A \\ y_A \\ z_A \end{pmatrix} = \begin{pmatrix} \cos 120^\circ & \sin 120^\circ & 0 \\ -\sin 120^\circ & \cos 120^\circ & 0 \\ 0 & 0 & 1 \end{pmatrix} \cdot \begin{pmatrix} \cos \alpha & 0 & \sin \alpha \\ 0 & 1 & 0 \\ -\sin \alpha & 0 & \cos \alpha \end{pmatrix} \cdot \begin{pmatrix} x_b \\ y_b \\ z_b \end{pmatrix}$$

$$= \begin{pmatrix} -1/2 \cos \alpha & \sqrt{3}/2 & -1/2 \sin \alpha \\ -\sqrt{3}/2 \cos \alpha & -1/2 & -\sqrt{3}/2 \sin \alpha \\ -\sin \alpha & 0 & \cos \alpha \end{pmatrix} \cdot \begin{pmatrix} x_b \\ y_b \\ z_b \end{pmatrix}$$

for system b, and

$$\begin{pmatrix} x_A \\ y_A \\ z_A \end{pmatrix} = \begin{pmatrix} \cos(-120^\circ) & \sin(-120^\circ) & 0 \\ -\sin(-120^\circ) & \cos(-120^\circ) & 0 \\ 0 & 0 & 1 \end{pmatrix} \cdot \begin{pmatrix} \cos \alpha & 0 & \sin \alpha \\ 0 & 1 & 0 \\ -\sin \alpha & 0 & \cos \alpha \end{pmatrix} \cdot \begin{pmatrix} x_c \\ y_c \\ z_c \end{pmatrix}$$

$$= \begin{pmatrix} -1/2 \cos \alpha & -\sqrt{3}/2 & -1/2 \sin \alpha \\ \sqrt{3}/2 \cos \alpha & -1/2 & \sqrt{3}/2 \sin \alpha \\ -\sin \alpha & 0 & \cos \alpha \end{pmatrix} \cdot \begin{pmatrix} x_c \\ y_c \\ z_c \end{pmatrix}$$

for system c.

The Zeeman interaction is given by the term $\vec{S} \cdot \vec{g} \cdot \vec{H}$ in the spin Hamiltonian. Since this term is a scalar, while \vec{H} is a contravariant tensor of rank 1 and \vec{S} is a co-variant tensor of rank 1, \vec{g} must be a mixed tensor of rank 2. The elements of the \vec{g} tensor for the n^{th} system of I, \tilde{g}_n , are determined in the new co-ordinate system by the transformation equations

$$g_{rp}^{nA} = \sum_q \sum_s \frac{\partial p}{\partial q} \frac{\partial s}{\partial r} g_{sq}^n$$

where,

$$\begin{aligned} n &= a, b, \text{ or } c, \\ q, s &= x_n, y_n, z_n, \\ r, p &= x_A, y_A, z_A, \end{aligned}$$

and g_{sq}^n is a tensor element of \tilde{g}_n in the (x_n, y_n, z_n) coordinate system. When the principal values of \tilde{g}_n in the (x_n, y_n, z_n) system are known, this expression reduces to the form

$$g_{rp}^{nA} = \sum_q \frac{\partial p}{\partial q} \frac{\partial q}{\partial r} g_{qq}^n$$

Hence, the tensor elements of \tilde{g}_{AVE} , which describes the Zeeman interaction of an averaged spectrum I, are given by

$$g_{rp}^{AVE} = \frac{1}{3} \sum_n g_{rp}^{nA}$$

Applying the co-ordinate transformations stated above to the case at hand, where,

$$g_{qq}^n = g_{qq}^a \quad \text{for all } n$$

$$g_{qs}^n = 0 \quad \text{for } q \neq s,$$

the following tensor elements of \tilde{g}_{AVE} are obtained

$$g_{xx}^{AVE} = 1/2 (\cos^2 \alpha g_{xx}^a + g_{yy}^a + \sin^2 \alpha g_{zz}^a)$$

$$g_{yy}^{AVE} = 1/2 (\cos^2 \alpha g_{xx}^a + g_{yy}^a + \sin^2 \alpha g_{zz}^a)$$

$$g_{zz}^{AVE} = \sin^2 \alpha g_{xx}^a + \cos^2 \alpha g_{zz}^a$$

$$g_{rp}^{AVE} = 0 \quad \text{for } r \neq p$$

Since $g_{xx}^{AVE} = g_{yy}^{AVE}$, these expressions obviously reduce to the relationships given in Eq. (36). Analogous relationships also exist for the hyperfine interaction tensor, \tilde{A} , and for the electric quadrupole interaction tensor, \tilde{Q} .

REFERENCES

1. G. Aminoff, Z. Kryst., vol.56(1921), 506.
2. H.D. Megaw, Proc. Roy. Soc. (London), vol.A142(1933) 198.
3. J.D. Bernal and H.D. Megaw, Proc. Roy. Soc.(London), vol.A151(1935), 384.
4. M. Yeow Ta, Compt. rend., vol.211(1940), 467.
5. C. Duval and J. Lecompte, Bull. Soc. Chim., vol.8(1941) 713.
6. C. Duval and J. Lecompte, Bull. Soc. Franc. Mineral. et Crist., vol.66(1943), 284.
7. R.T. Mara and G.B.B.M. Sutherland, J.Opt. Soc. Amer., vol.43(1953), 1100.
8. H.E. Petch and H.D. Megaw, J. Opt. Soc. Amer., vol.44 (1954), 744.
9. D.D. Elleman and D. Williams, J. Chem. Phys., vol.25 (1956), 742.
10. R.T. Mara and G.B.B.M. Sutherland, J. Opt. Soc. Amer., vol.46(1956), 464.
11. R.M. Hexter and D.A. Dows, J. Chem. Phys., vol.25(1956), 504.
12. K.A. Wickersheim, J. Chem. Phys., vol.31 (1959), 863.
13. G. Safford, V. Brajovic and Bouÿtin, J. Phys. Chem. Solids., vol.24(1963), 771.
14. W.R. Busing and H.A. Levy, J. Chem. Phys., vol.26(1957), 563.
15. H.E. Petch, Acta Cryst., vol.14(1961), 950.
16. F. Holuj, S.M. Quick, and M. Rosen, Phys. Rev., vol.B6 (1972), 3169.
17. H.A. Jahn and E. Teller, Phys. Rev., vol.49(1936), 874.
18. D.C. Burnham, Bull. Am. Phys. Soc., vol.11(1966), 186.
19. J. Sierro, J. Phys. Chem. Solids., vol.28(1967), 417.
20. U.T. Höchli, K.A. Muller, and P. Wysling, Phys. Letters., vol.15(1965), 5.
21. W. Hayes and J. Wilkens, Proc. Roy. Soc.(London), vol.A281(1964), 340.

22. J.R. O'Conner and J.H. Chen, Appl. Phys. Letters., vol.5(1964), 100.
23. F.R. Merrit and M.D. Sturge, Bull. Am. Phys. Soc., vol.11(1966), 202.
24. R. La Croix, U. Höchli, and K.A. Muller, Helv. Phys. Acta., vol.37(1964), 627.
25. W. Low and A. Rosenthal, Phys. Letters., vol.26A (1968), 143.
26. R.E. Coffman, Phys. Letters., vol.19(1965), 475.
27. R.E. Coffman, Phys. Letters., vol.21(1966), 381.
28. R.E. Coffman, J. Chem. Phys., vol.48(1968), 609.
29. U.T. Höchli and T.L. Estle, Phys. Rev. Letters., vol.18(1967), 128.
30. U.T. Höchli, Phys. Rev., vol.162(1967), 262.
31. J.H. van Vleck, J. Chem. Phys., vol.7(1939), 61.
32. J.H. van Vleck, J. Chem. Phys., vol.7(1939), 72.
33. U. Öpik, and M.H.L. Pryce, Proc. Roy. Soc. (London), vol.A238(1957), 425.
34. A.D. Liehr and C.J. Ballhausen, Ann. Phys. (N.Y.), vol.3(1958), 304.
35. M.C.M. O'Brien, Proc. Roy. Soc. (London), vol.A281 (1964), 323.
36. I.B. Bersuker, Zh. Eksperim. i Teor. Fiz., vol.43 (1962), 1315. (English Translation: Soviet Phys...JETP., vol.16(1963), 933.)
37. F.S. Ham, Phys. Rev., vol.A138(1965), 1727.
38. M.D. Sturge, Solid State Physics., vol.20 (New York: Academic Press, 1967), 91.
39. F.S. Ham, "Jahn-Teller Effects in Electron Paramagnetic Spectra", Electron Paramagnetic Resonance., (New York: Plenum Publishing Corp., 1969).
40. A. Abragam and B. Bleaney, Electron Paramagnetic Resonance of Transition Elements., (Oxford: Clarendon Press, 1970).
41. R.G. Wilson, F. Holuj, and N.E. Hedgecock, Phys. Rev., vol.B1(1970), 3609.
42. F. Holuj and R.G. Wilson, Phys. Rev., vol.B7(1973), 4065.

43. H.D. Megaw, Proc. Roy. Soc. (London), vol.A142(1933), 198.
44. J.D. Bernal and H.D. Megaw, Proc. Roy. Soc. (London), vol.A151(1935), 384.
45. H.E. Petch, Acta Cryst., vol.14(1961), 950.
46. W.R. Busing and H.A. Levy, J. Chem. Phys., vol.26 (1957), 563.
47. A. Abragam and B. Bleaney, Electron Paramagnetic Resonance of Transition Elements., (Oxford: Clarendon Press, 1970), 395, 775-777.
48. J. Owen and J.H.M. Thornley, Rep. Prog. Phys., vol.29 (1966), 675.
49. B.R. McGarvey, J. Phys. Chem., vol.71(1967), 51.
50. C. Basu and U.S. Ghosh, J. Phys. Chem. Solids., vol.32 (1971), 2259.
51. B. Bleaney, K.D. Bowers, and D.J.E. Ingram, Proc. Roy. Soc., vol.A228(1955), 147.
52. B. Bleaney, K.D. Bowers and R.S. Trenam, Proc. Roy. Soc., vol.A228(1955), 157.
53. B. Bleaney, K.D. Bowers, and M.H.L. Pryce, Proc. Roy. Soc., vol.A228(1955), 166.
54. A. Abragam and B. Bleaney, Electron Paramagnetic Resonance of Transition Elements., (Oxford: Clarendon Press, 1970), 696.
55. Ibid., 414, 696.
56. B.R. McGarvey, J. Phys. Chem., vol.71(1967), 51.
57. J.H. van Vleck, J. Chem. Phys., vol.7(1939), 72.
58. F. Holuj, S.M. Quick, and M. Rosen, Phys. Rev., vol.B6 (1972), 3169.
59. F.S. Ham, "Jahn-Teller Effects in Electron Paramagnetic Spectra", Electron Paramagnetic Resonance., (New York: Plenum Publishing Corp., 1969).
60. U. Opik and M.H.L. Pryce, Proc. Roy. Soc. (London), vol.A238(1957), 425.
61. M.C.M. O'Brien, Proc. Roy. Soc. (London), vol.A281 (1964), 323.
62. A. Abragam and M.H.L. Pryce, Proc. Phys. Soc. (London), vol.A63(1950), 409.
63. F. Holuj, Can. J. Phys., vol.46(1968), 287.

64. F. Holuj, and R.G. Wilson, Phys. Rev., vol.B7(1973), 4065.
65. U. Öpik and M.H.L. Pryce, Proc. Roy. Soc.(London), vol.A238(1957), 425.
66. J.H. van Vleck, J. Chem. Phys., vol.7(1939), 72.
67. R.G. Wilson, F. Holuj, N.E. Hedgecock, Phys. Rev., vol.B1(1970), 3609.
68. U. Öpik and M.H.L. Pryce, op.cit., 425.
69. W. Low, J.T. Suss, Phys. Letters.(Netherlands), vol.7(1963), 310.

BIBLIOGRAPHY

- Abragam A., Bleaney B., Electron Paramagnetic Resonance of Transition Elements., Oxford: Clarendon Press, 1970.
- Abragam A., Pryce M.H.L., Proc. Phys. Soc. (London), vol.A63 (1950), 409.
- Aminoff G., Z. Kryst., vol. 56(1921), 506.
- Basu C., Ghosh U.S., J. Phys. Chem. Solids., vol.32(1971), 2259.
- Bernal J.D., Megaw H.D., Proc. Roy. Soc. (London), vol.A151 (1935), 384.
- Bersuker, I.B., Zh. Eksperim. i Teor. Fiz., vol.43(1962), 1315. (English Translation: Soviet Phys...JETP., vol.16(1963), 933).
- Bleaney B., Bowers K.D., Ingram D.J.E., Proc. Roy. Soc., vol. A228(1955), 147.
- Bleaney B., Bowers K.D., Pryce M.H.L., Proc. Roy. Soc., vol.A228(1955), 166.
- Bleaney B., Bowers K.D., Trenam R.S., Proc. Roy. Soc., vol.A228 (1955), 157.
- Burnham D.C., Bull. Am. Phys. Soc., vol.11(1966), 186.
- Busing W.R., Levy H.A., J. Chem. Phys., vol.26(1957), 563.
- Coffman, R.E., Phys. Letters., vol.19(1965), 475.
- Coffman, R.E., Phys. Letters., vol.21(1966), 381.
- Coffman, R.E., J. Chem. Phys., vol.48(1968), 609.
- Duval C., Lecompte J., Bull. Soc. Chim., vol.8(1941), 713.
- Duval C., Lecompte J., Bull. Soc. Franc. Mineral et Crist., vol.66(1943), 284.
- Elleman D.D., Williams D., J. Chem. Phys., vol.25(1956), 742.
- Ham F.S., Phys. Rev., vol.A138(1965), 1727.

Ham F.S., Electron Paramagnetic Resonance., New York:
Plenum Publishing Corp., 1969.

Hayes W., Wilkens J., Proc. Roy. Soc. (London), vol.A281
(1964), 340.

Hexter R.M., Dows D.A., J. Chem. Phys., vol.25(1956), 504.

Höchli U.T., Phys. Rev., vol.162(1967), 262.

Höchli U.T., Estle T.L., Phys. Rev. Letters., vol.18(1967),
128.

Höchli U.T., Muller K.A., Wysling P., Phys. Letters.,
vol.15(1965), 5.

Holuj F., Can. J. Phys., vol.46(1968), 287.

Holuj F., Quick S.M., Rosen M., Phys. Rev., vol.B6(1972),
3169.

Holuj F., Wilson R.G., Phys. Rev., vol.B7(1973), 4065.

Jahn H.A., Teller E., Phys. Rev., vol.49(1936), 874.

La Croix R., Höchli U., Muller K.A., Helv. Phys. Acta.,
vol.37(1964), 627.

Liehr A.D., Ballhausen C.J., Ann. Phys. (New York), vol.3
(1958), 304.

Low W., Rosenthal A., Phys. Letters., vol.26A(1968), 143.

Low W., Suss J.T., Phys. Letters. (Netherlands), vol.7(1963),
310.

Mara R.T., Sutherland G.B.B.M., J. Opt. Soc. Amer., vol.43
(1953), 1100.

Mara R.T., Sutherland G.B.B.M., J. Opt. Soc. Amer., vol.46
(1956), 464.

McGarvey B.R., J. Phys. Chem., vol.71(1967), 51.

Megaw H.D., Proc. Roy. Soc. (London), vol.A142(1933), 198.

Merritt F.R., Sturge M.D., Bull. Am. Phys. Soc., vol.11(1966),
202.

O'Brien M.C.M., Proc. Roy. Soc. (London), vol.A281(1964), 323.

O'Connor J.R., Chen J.H., Appl. Phys. Letters., vol.5(1964), 100.

Opik U., Pryce M.H.L., Proc. Roy. Soc.(London), vol.A238 (1957), 425.

Owen J., Thornley J.H.M., Rep. Prog. Phys., vol.29(1966), 675.

Petch H.E., Megaw H.D., J. Opt. Soc. Amer., vol.44(1954), 744.

Petch H.E., Acta Cryst., vol.14(1961), 950.

Safford G., Brajovic V., Boutin, J. Phys. Chem. Solids., vol.24(1963), 771.

Sierro J., J. Phys. Chem. Solids., vol.28(1967), 417.

Sturge M.D., Solid State Physics., New York: Academic Press, vol.20, 1967.

Van Vleck J.H., J. Chem. Phys., vol.7(1939), 61,72.

Wilson R.G., Holuj F., Hedgecock N.E., Phys. Rev., vol.B1 (1970), 3609.

Yeou Ta M., Compt. rend., vol.211(1940), 467.

VITA AUCTORIS

* On March 24, 1943, I was born in Windsor, Ontario and I received my early education there. In 1962, I enrolled in the Honours Physics and Mathematics course at the University of Windsor and graduated with a B.Sc. degree in Physics in 1966 and a M.Sc. degree in 1967. I married in 1971 and after completing my experimental work, I left Windsor to accept a teaching position in the Mathematics and Science Department at Fanshawe College in London, Ontario.